Pore-scale Interfacial and Transport Phenomena in Hydrocarbon Reservoirs

Chao Fang

Dissertation submitted to the faculty of the Virginia Polytechnic Institute and State University in partial fulfillment of the requirements for the degree of

Doctor of Philosophy
In
Mechanical Engineering

Rui Qiao, Chair
Danesh K Tafti
Mark R Paul
Pengtao Yue
Ryan Pollyea

May 10th, 2019
Blacksburg, VA

Keywords: hydrocarbon recovery, thin films, disjoining pressure

Pore-scale Multiphase Interfacial and Transport Phenomena in Hydrocarbon Reservoirs

Chao Fang

ABSTRACT

Exploring unconventional hydrocarbon reservoirs and enhancing the recovery of hydrocarbon from conventional reservoirs are necessary for meeting the society's ever-increasing energy demand and requires a thorough understanding of the multiphase interfacial and transport phenomena in these reservoirs. This dissertation performs pore-scale studies of interfacial thermodynamics and multiphase hydrodynamics in shale reservoirs and conventional oil-brine-rock (OBR) systems.

In shale gas reservoirs, the imbibition of water through surface hydration into gas-filled mica pores was found to follow the diffusive scaling law, but with an effective diffusivity much larger than the self-diffusivity of water molecules. The invasion of gas into water-filled pores with width down to 2nm occurs at a critical invasion pressure similar to that predicted by the classical capillary theories if effects of disjoining pressure and diffusiveness of water-gas interfaces are considered. The invasion of oil droplets into water-filled pores can face a free energy barrier if the pressure difference along pore is small. The computed free energy profiles are quantitatively captured by continuum theories if capillary and disjoining pressure effects are considered. Small droplets can invade a pore through thermal activation even if an energy barrier exists for its invasion.

In conventional oil reservoirs, low-salinity waterflooding is an enhanced oil recovery method that relies on the modification of thin brine films in OBR systems by salinity change. A systematic study of the structure, disjoining pressure, and dynamic properties of these thin brine films was performed. As brine films are squeezed down to sub-nanometer scale, the structure of water-rock and water-oil interfaces changes marginally, but that of the electrical double layers in the films changes greatly. The disjoining pressure in the film and its response to salinity change follow the

trend predicted by the DLVO theory, although the hydration and double layer forces are not simple additive as commonly assumed. A notable slip between the brine film and the oil phase can occur.

The role of thin liquid films in multiphase transport in hydrocarbon reservoirs revealed here helps lay foundation for manipulating and leveraging these films to enhance hydrocarbon production and to minimize environmental damage during such extraction.

Pore-scale Multiphase Interfacial and Transport Phenomena in Hydrocarbon Reservoirs

Chao Fang

GENERAL AUDIENCE ABSTRACT

Meeting the ever-increasing energy demand requires efficient extraction of hydrocarbons from unconventional reservoirs and enhanced recovery from conventional reservoirs, which necessitate a thorough understanding of the interfacial and transport phenomena involved in the extraction process. Abundant water is found in both conventional oil reservoirs and emerging hydrocarbon reservoirs such as shales. The interfacial behavior and transport of water and hydrocarbon in these systems can largely affect the oil and gas recovery process, but are not well understood, especially at pore scale. To fill in the knowledge gap on these important problems, this dissertation focuses on the pore-scale multiphase interfacial and transport phenomena in hydrocarbon reservoirs.

In shales, water is found to imbibe into strongly hydrophilic nanopores even though the pore is filled with highly pressurized methane. Methane gas can invade into water-filled nanopores if its pressure exceeds a threshold value, and the thin residual water films on the pore walls significantly affect the threshold pressure. Oil droplet can invade pores narrower than their diameter, and the energy cost for their invasion can only be computed accurately if the surface forces in the thin film formed between the droplet and pore surface are considered. In conventional reservoirs, thin brine films between oil droplet and rock greatly affect the wettability of oil droplets on the rock surface and thus the effectiveness of low-salinity waterflooding. In brine films with sub-nanometer thickness, the ion distribution differs from that near isolated rock surfaces but the structure of water-brine/rock interfaces is similar to their unconfined counterparts. The disjoining pressure in thin brine films and its response to the salinity change follow the trend predicted by classical theories, but new features are also found. A notable slip between the brine film and the oil phase can occur, which can facilitate the recovery of oil from reservoirs.

Acknowledgements

In a blink, my PhD study at Virginia Tech comes to an end after these incredible years. I would like to thank many people that generously contributed to the work presented in this dissertation. I could not be more grateful to have the pleasure of working with my advisor, Dr. Rui Qiao. His guidance and care have made me finish these work. His altitude towards research has been inspiring me on my work and the critical way of thinking will make me digest for the rest of my life. The support and helpful discussions on many interesting problems are also truly valued. I want to extend my gratitude to the committee members, Dr. Danesh Tafti, Dr. Mark Paul, Dr. Pengtao Yue, and Dr. Ryan Pollyea, for their valuable time and advices throughout my research and study. Additionally, the work in this dissertation would not have been possible without the generous computational hours provided by ARC at Virginia Tech.

I want to thank the collaborators. The help on water simulation using Lammps from Dr. Jingwen Mo and Dr. Zhigang Li has initiated the work in this dissertation. The fruitful discussions with Dr. Weiwei Xu and Dr. Miao Yu have effectively linked simulation results to experiment observations.

I appreciate the time and training in TPL group and thank all members for the pleasant working environment. In particular, I want to thank Dr. Yadong He for numerous help during my early stage of atomistic simulations and Dr. Fengchang Yang for introducing me into PNP simulation. I want to thank the help and collaboration from and with group members worked together: Dr. Ying Liu, Dr. Zhou Yu, Mr. Fei Zhang, Mr. Haiyi Wu, and Mr. Doyoon Moh. In addition, I would like to thank the friends and peers, including these above, for the wonderful moments in Blacksburg.

Finally, I dedicate this dissertation to my parents. They have made so much sacrifice for me and supported me in whatever I pursue. I am always beholden for their eternal love and encouragement.

Contents

List of Figures

Chapter 1. Introduction

1.1 Hydrocarbon Energy Resources

Our society is powered by energy resources. As a consequence of humanity's improvement of life quality, the demand for energy resources keeps increasing. For instance, it was predicted that the total global energy demand will increase by 50%-60% between 2008 and 2030s as a result of global population growth and living standard improvement.[1] At present, natural gas, oil, coal, hydropower, and nuclear energy are the five primary energy sources globally, accounting for 85% of the world energy consumption.[2] These energy sources are supplemented by several renewable energy sources of either natural or biosphere sources.[3-5]

Of the five primary energy sources, hydrocarbon is expected to remain as a mainstay in energy consumption in the next few decades despite their environmental consequence of greenhouse gas emission.[2, 6-7] There is no doubt that a transition from hydrocarbon fossil fuels to renewable energy including hydro, wind, solar, and nuclear power sources is preferred. However, the harvesting rates of renewable energy are far behind the rise of energy demand.[6] As such, in short term, hydrocarbon, which offers superior properties such as high specific energy content, cost-effective production and utilization, and high energy return,[2] must still be relied upon. Indeed, as shown in the consumption of different types of primary energy sources in Fig. 1-1a, no drastic variations are anticipated for the global energy composition in the next decades. Even though the redistribution of each energy source can occur, the production of energy in individual categories will rise and the consumption of gas, oil, and coal will continue to increase.[2] In line with the above information, the US Energy Information Administration (EIA) has forecasted in 2013 that hydrocarbons (petroleum, natural gas and coal) will still make up 78% of the global primary energy resource consumption in 2040.[8]

Of the three main types of hydrocarbons (oil, gas, and coal), coal is least desirable despite their huge reserve that can power the world for many decades.[9] This is in part because of the intense

CO_2 emission and release of harmful pollutants (e.g. SO_2) during their combustion.[2, 6] On the other hand, natural gas is abundant, involves less CO2 emission than coal, and their consumption is on the rise.[10] Oil has the advantage of high energy density and thus remains highly competitive in the global energy market.[2, 11]

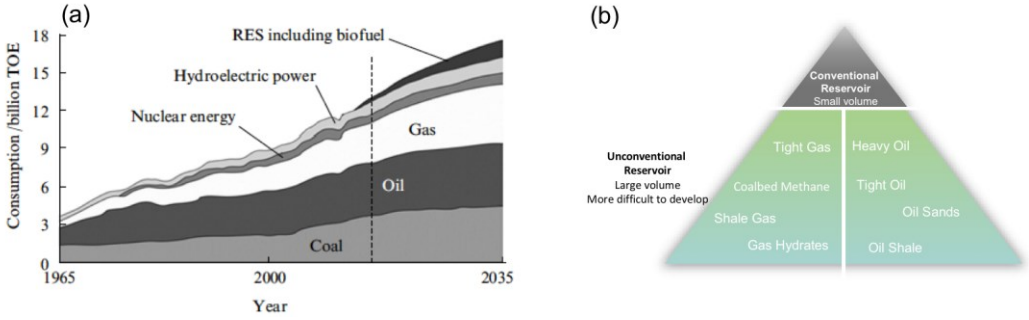

Figure 1-1. *Global energy sources.* **(a)** Existing and forecasted consumption of primary energy sources in the global energy balance. (TOE is tons of oil equivalent; RES is renewable energy source) **(b)** World hydrocarbon energy source pyramid. Panel (a) is taken from Ref. 2 with permission from Turpion; panel (b) is reproduced from Ref. 12 with permission from the Society of Petroleum Engineers.

While the demand for oil and gas is expected to remain strong in the coming decades, meeting such demand faces some challenges. Conventional hydrocarbons are enriched locally in the basins with high quality but low volume. After more than 100 years of exploration, the gas and oil reserves in the conventional reservoirs become increasingly more limited. On the other hand, oil and gas in unconventional sources,[13] namely these hydrocarbons that cannot be produced by conventional techniques,[14] may offer an alternative. As shown in the world hydrocarbon energy source pyramid (Fig. 1-1b), oil and gas from unconventional source exist in the form of heavy oil, shale oil, tight gas, shale gas, coalbed methane, gas hydrate, etc.[12, 15] They are distributed over large area of basins and account for about 80% of total hydrocarbon resources.[3] Indeed, excluding gas hydrate, the endowment, defined as the summation of cumulative gas production, reserves, and undiscovered gas, is about 68,000 trillion ft^3, and shale and tight formations comprise 70% of such endowment.[15] With these hydrocarbon sources, the life span of oil and gas may be extended by another 150 years, thus leaving time for the advent or more efficient utilization of renewable energies.[16-17]

With the existing conventional hydrocarbons and emerging unconventional hydrocarbons, the current global hydrocarbon energy market is in a stage of continuous exploration of conventional sources and a rapid exploration of unconventional sources. Conventional hydrocarbons still play an important role in meeting the energy demand, especially considering the fact that their recovery percentage is only at 25% and can be improved in the future.[18] Unconventional hydrocarbons are on a sharp rise. For example, because of the recent boom of shale gas in North America, shale gas now accounts for more than 40% of the total natural gas production.[19-20] Additionally, more than 50% of total U.S. oil production in 2015 is generated from shale and tight formations, the amount of which is anticipated to grow with the active investment of unconventional sources.[21] In the near future, it is expected the total output of unconventional source hydrocarbon will increase from 10% in 2013 to more than 20% in 2030.[5, 8]

To utilize the conventional and unconventional hydrocarbon sources effectively, it is important to explore the efficient and environmentally friendly production from unconventional sources and to enhance the recovery of hydrocarbons from conventional sources. Doing so needs a sound understanding of the interfacial and transport phenomena involved in the hydrocarbon extraction from these sources. The present dissertation is driven by this need.

1.2 Exploring Unconventional Reservoirs

1.2.1 Shale formations

Gas and oil from shales are now considered as major unconventional hydrocarbon sources. Shale is loosely defined as a class of fine-grained clastic sedimentary rocks composed primarily of tiny particles of clay minerals and quartz.[22] More strict definition considers the composition and size of shales. For example, “a lithostratigraphic unit having less than 50% by weight organic matter, with less than 10% of the sedimentary clasts having a grain size greater than 62.5

micrometres and more than 10% of the sedimentary clasts having a grain size less than 4 micrometres." is defined as shale in Section 1.020(2)(27.1) of the *Oil and Gas Conservation Regulations*. A typical shale formation is shown in Fig. 1-2a, which is composed of a rock space of clay-minerals, nonclay-minerals, and organic matters with 90% kerogen and 10% bitumen, and pore space of water in clay-bound, capillary-bound, and mobile states, and hydrocarbons.[23-24]

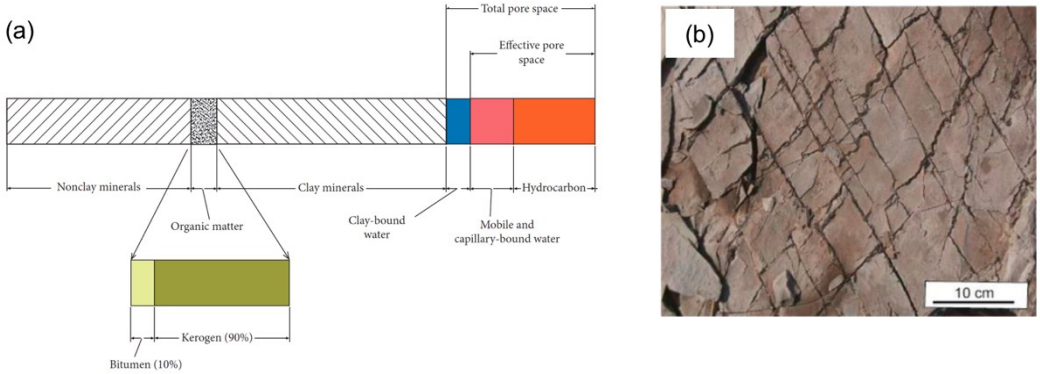

Figure 1-2. *Shale composition*. **(a)** Schematic representation of typical shale composition. **(b)** Outcrop of natural fractures in Woodford Shale, Oklahoma, USA. Panel (a) is taken from Ref. 23 with permission from Hindawi under the Creative Commons Attributions License; panel (b) is taken from Ref. 25 with permission from Elsevier.

Shale formations are characterized by deep colored rocks with many natural fractures, as shown in Fig. 1-2b. The level of the darkness of shale rocks is largely determined by their organic carbon content.[22] The organic rich shales are in dark color or "black", whereas organic-lean shales are in lighter color or "grey". Black shales are of more interest to the unconventional hydrocarbon source development as a result of their rich carbon content. However, the quantitative correlation between carbon content and shale color is impeded by the saturation of darkness with the increase of carbon content.[26] The organic carbon of black shale comes mainly from the plant detritus which had accumulated with the sediment that commonly sourced from fresh algae, marine algae, or terrestrial plants.[27]

Shales' organic matter mainly consists of kerogen. Kerogen is a mixture of many organic materials with chemical compounds varying between samples and has no specific structure. When krogen matures, oil and gas are produced.[24, 28-30] The maturation of kerogen occurs by subjecting

to high level of heat and pressure for a long period of time, and then small molecules of natural gas break from kerogen by thermal decomposition.[23] Natural gas is trapped in shales in different ways, including as gas adsorbed on and dissolved into kerogen, as free gas trapped in nonorganic interparticle porosity or microfracture porosity, as free gas stored in hydraulic fractures by stimulation, and as free gas trapped in pore-network developed within the organic matter.[12, 31-33] The last one helps explain the unexpectedly large gas rates and recoveries of natural gas from some shale formations.[12]

The storage of gas and oil in shales differs from that in conventional reservoirs in several aspects. Gas and oil are generated by the organic matter deposited in shales and remain sealed within their fine-grained rock. Shale thus can act as both source and reservoir rock. Huge amount of gas and oil can be held in shales; in conventional reservoirs, a complex process of numerous events must happen in definite order to form hydrocarbon.[22, 34] Unconventional reservoirs of shale are also known as "continuous source" because they can in principle occupy the whole volume of geological formations.[34]

Two common confusing terminologies about shales should be clarified. Tight formations also occupy substantial portion in unconventional sources. Two common characteristics about shale and tight formations are that the reservoirs form part of continuous formations by extending over large areas and the formations have low permittivity. The permeability of tight formation is less than 0.1 mD,[35] whereas that for shale matrix is on the order of nano-Darcies (or slightly higher if naturally existing fractures are abundant).[21] In the case of tight oil and gas, the oil and gas are generated usually in shale/coal and migrate into tight formations to be trapped and stored. Tight formation thus only acts as reservoir rock. However, in practice, shale oil and tight oil are usually not clearly differentiated from each other,[12, 21] but are used interchangeably. The other confusing terminology is shale oil and oil shale. Although sometimes shale oil includes oil from oil shale and shale formations,[35-36] a major difference between shale oil and oil shale exists: oil shale is a *rock*

that contains organic component of kerogen, which can be heated to high temperature to generate oil and gas.[21]

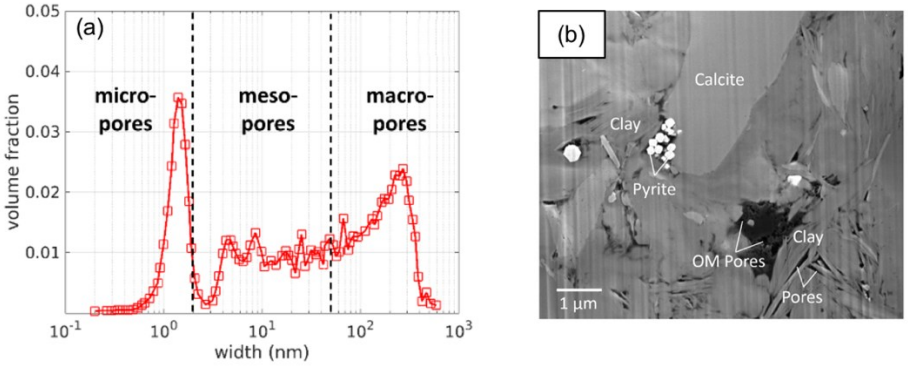

Figure 1-3. *Pores of shales.* **(a)** Pore size distribution of a representative shale sample. Micropores: width<2nm; mesopores: 2nm<width<50nm; macropores: width>50nm. **(b)** Backscattered electron images of Marcellus shale sample. Black depicts pores, dark grey is kerogen, and light gray is inorganic shale matrix. Interparticle pores between organic matter are generally equant, while pores between clay particles are slit like. Panel (a) is reproduced from Ref. 37 with permission from the American Chemical Society; panel (b) is taken rom Ref. 38 with permission from the American Chemical Society.

Extracting gas and oil from shales kilometers below the surface have long been challenging because shale has very low matrix permeability and a porosity less than 10%.[35, 39] The low permeability is caused by the small pore size in shale formations. For instance, as shown in Fig. 1-3, the distribution of the pore size in typical shale sample is broad and a significant portion of the pores are micropores with diameter less than 2nm.[37] To effectively extract the gas in shales, it is important to create artificial fractures and pores to provide pathway for the gas to be recovered. In the past decade, horizontal drilling and hydraulic fracturing have been developed to address this need. These techniques can greatly increase the contact area between wellbore and the pay zone and enable gas stored in small pores to be recovered. These techniques are discussed below.

1.2.2 Drilling and fracturing

The recovery of hydrocarbon from shale formations are both technologically and economically viable due to the new techniques developed for drilling and fracturing.[40-41] Figure 1-4a shows the drilling and fracturing process. The extraction of conventional natural gas can be enabled by only

applying vertical wells. Horizontal drilling starts from such vertical wells as the depth of wellbore is about the same depth as shale formations, up to a depth between 2000 and 3000km.[42] The horizontal drilling is performed across the length of the shale bed, with a well length of ~5.5km reported in 2016.[43] Sometimes multiple wells in different directions, on distances of 1-2km, are created to maximize the number of created cracks.[44] Multiple hydraulic fractures can later be generated along the length of the well. Numerous high permeability flow paths are created in this way that form contact with substantially larger shale volume than that in single cracks adopted in traditional wells.[22] After hydraulic fracturing, a period of well shit-in to soak the fracture fluids (i.e. soak-back technique) is usually performed to enhance hydrocarbon production.[45-46]

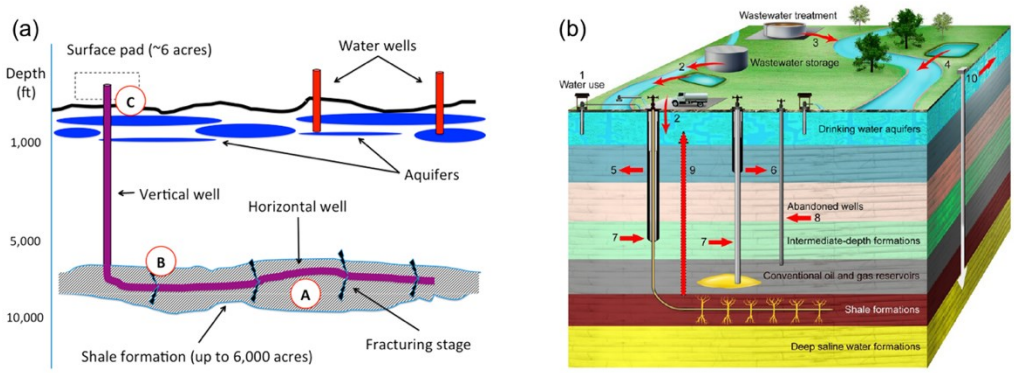

Figure 1-4. *Horizontal drilling and hydraulic fracturing.* **(a)** Schematic representation of drilling and fracturing of well. **(b)** Schematic illustration of possible modes of water impacts associated with drilling and fracturing. Panel (a) is taken from Ref. 47 with permission from the American Chemical Society; panel (b) is taken rom Ref. 48 with permission from the American Chemical Society.

Horizontal drilling. Horizontal test wells were first air-drilled in a gas shale in 1986.[49] Horizontal drilling appeared around 1930s,[50] but had two technical problems including driving the bit through curves and detecting the bottom location of the hole.[51] These problems were overcome by the advance of downhole hydraulic motor and bottomhole assembly and the improvement in downhole position measurement.[22, 51] Technological advancement of horizontal drilling mainly came about after 1990s.[22] Recently, drilling horizontal wells with gas that contains air, nitrogen, and natural gas has been acknowledged as an optimal technique to explore shale reservoir, with which footage capacity can be improved while drilling cost decreased.[52] Development of new

drilling technologies primarily focuses on decreasing the cuttings' size at the bottom hole to eliminate the influence of gas flow.[53] Most horizontal wells are now drilled by first minimizing the horizontal stress to allow for more transverse hydraulic fractures and then coverage area is expanded by drilling the horizontal part through the shale rocks.[54-55] After horizontal drilling, techniques including production casing and cementing are applied to protect the well and block gas leakage.[56]

Hydraulic fracturing, commonly referred as fracking, was commercially introduced in 1949 but originated from the use of explosive liquids to stimulate oil wells in 1860s.[57] In hydraulic fracturing process, high pressure fluids are injected into wells to stimulate the shale formations such that the hydraulic conductivity is raised and the rate of gas and oil flowing back to the wellbore is enhanced.[58] The shale rock connectivity stimulated from fracking can be improved by several orders of magnitude, i.e. shales are expanded from micro-sized openings to fractures greater than tens of micrometers in width and these fractures can propagate several meters into the formation.[59-60]

Pressures up to over 137MPa are applied during fracturing.[47] During the production of one horizontal well, on average 10-15 million liters of water and tens thousands of liters of chemicals (~1% of the total volume) are used.[61-62] The fracturing fluids are a mixture of largely fresh water, propants such as sands, and organic and inorganic chemicals additives.[22, 57] The chemical additives serve functionalities including cleaning the wellborn, altering the wettability between the fluid and shale, protecting wells from clogging, *etc*.[63-65] Once the hydraulic pressure is released, some of the fracking fluids returns to well as the so called "flow-back" water and are removed.[47, 66] Fracturing is often not a one-off event and some wells can be fracked up to 30 times.[47, 66]

Environmental concerns. Despite the many positive impacts, hydraulic fracturing has raised numerous environmental concerns about the hydrocarbon production in shales. The concerns arise from various aspects including surface and underground water contamination due to the "flowback"

and produced water in fracking, migration of chemicals and hydrocarbon from shales to water aquifers, and water/air quality risk due to emission from production, occurrence of earthquake, and blowout associated with fracturing.[67] Spatial assessments show that water contamination, gas emission, and local environment change become more severe near the fracking well.[68]

Amongst these concerns, the potential contamination of water by fracking fluids draws much attention. For instance, various potential modes of water resource degradation have been identified and schematically illustrated in Fig. 1-4b.[48] The modes can be summarized into four categories: (1) shallow aquifer contamination by fugitive hydrocarbon; (2) surface and underground water contamination from spills, leaks, and the disposal of inadequately treated fracturing fluids; (3) toxic and radioactive elements accumulation in soil and stream sediments; (4) overuse of water resources. One particular concern is the transport and fate of the fracking fluids in shale formations. Field observations suggest that only a small portion of the fracking fluids injected into shale returns to ground after hydraulic fracturing.[47] For example, the volume of "flowback" water is about 10-40% of the total injected fracking fluids and the returned fracking fluids are even lower due to increasing portion of formation water.[69] The fate of the rest of the fracking fluids remains largely unknown and raises the widespread concern that they can migrate to drinking water aquifers.[70]

1.2.3 Fracking water migration

Fate of fracking fluids. Fracking fluids can potentially migrate to shallow aquifers due to poor gas and oil-well integrity and the existence of natural or induced conductive faults or fractures in shale formations.[70-71] The migration through highly impermeable shale formations is avidly debated. For instance, while one model has suggested that the transport of fracking fluids through fractured shales to aquifers in several years,[71] other studies dispute such model by pointing out that the flow rate is much lower due to low permeability of shale formations, small upward hydraulic gradient, and the high fluid density.[72-76] Indeed, a number of situations make upward migration unlikely, e.g. stray gas migration and deep injection to dispose of waste fluids.[77] Such argument is

supported by the fact that natural gas and CO_2 are more buoyant than fracking fluids,[48, 77] which is further verified in some field observations.[78-79] However, evidence on the flow of deep saline water into aquifer has been demonstrated in some shale formations,[80-83] and possible fracking fluids migration to drinking water aquifer is suggested by various numerical models.[71, 84]

Recent research suggests that imbibition of fracking fluids into natural fractures and shales matrix is responsible for the high fracturing fluid retention in shales.[85-87] Such imbibition has dual effects. From an environment perspective, it is potentially beneficial as fracking fluids can be sequestered into shales and the potential migration toward aquifers is consequently reduced.[75, 88] The imbibition can also enhance hydrocarbon production from the well by displacing them into the fractures.[87, 89] On the other hand, fluid imbibition can damage a reservoir by lowering its permeability, reducing fracture connectivity, and shortening fracture length.[90-92] To effectively manage the beneficial and detrimental aspects of fluids imbibition into shale formations, research on fluids imbibition into shales has received significant attention recently.

Imbibition in shales. On macroscopic scales, capillary filling or imbibition of a pore has been understood since the beginning of 20th century. The famous Lucas-Washburn equation has been successfully applied to predict the capillary filling process shown in Fig. 1-5a .[93-94] This equation follows a $\sqrt{t}$ law of filling length of the fluid in capillary with a constant radius

$$H(t) = (\gamma R cos\theta/2\mu)^{1/2}\sqrt{t}, \qquad (1.1)$$

where γ is the surface tension of the liquid, R is the radius of the capillary, θ is the contact angle between the meniscus and the wall, and μ is the dynamic viscosity of the liquid. Equ. 1.1 is obtained by equating the viscous drag of the filled liquid $4\mu d[H(t)^2/R^2]/dt$ from laminar flow and the capillary force $2\gamma cos\theta/R$, and doing an integration over time. Because inertial is neglected, Equ. 1.1 is not valid at the initial filling stage. Note that Equ. 1.1 can be extended to other pore shape (e.g. slit shape) and similar scaling law is obtained.

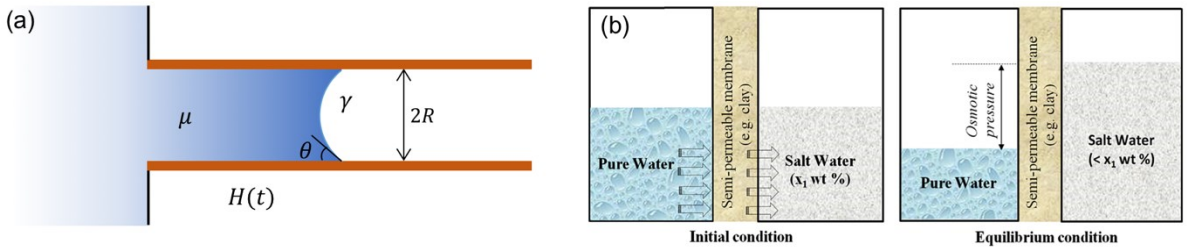

Figure 1-5. *Water imbibition through capillary flow and osmosis.* **(a)** Schematic representation of water imbibition through capillary flow. **(b)** Schematic representation of water imbibition through osmosis in shale. Panel (b) is taken from Ref. 95 with permission from Elsevier.

The Lucas-Washburn equation has been applied and extended by many researchers to describe the spontaneous imbibition in porous media. For instance, the effects of viscosity ratio, tortuosity, variable shaped pores, and the fractal nature of pores in porous media have all been considered to improve Equ. 1.1.[96-98] More recent models take into account some properties of porous medias like wettability and pore structures from capillary pressure and permeability curves of porous media.[99-100] Furthermore, on the fundamental side, numerous phenomena with qualitative and quantitative deviations from this law have been identified in nanofluidic transport.[101-106] For instance, slippage at liquid-wall interfaces,[103, 107-108] disjoining pressure in liquid films,[107, 109] electroviscous effects,[101, 110] enhanced viscosity of interfacial or highly confined fluids,[111] and contact angle hysteresis[112] have been shown to greatly affect liquid imbibition into nanopores.

Compared with the understanding of imbibition in other porous media or conventional rocks, the knowledge about imbibition in shale is still evolving.[95] The low recovery rate of fracking fluids to ground is initially postulated to result from the capillary imbibition into shale matrix through two modeling studies.[113-114] Further attention on the imbibition of fracking fluids in shale is from experiments, where spontaneous imbibition on gas production has been performed on some shale samples.[115] Recently, laboratory investigations suggest that the imbibition length in shale samples deviates from the $\sqrt{t}$ law.[85, 116] These observations are not yet understood though different reasons have been proposed in individual studies.

The imbibition rates of fluids into shales are largely determined by the pores and the imbibing

fluids. The pores in shale is not homogenous but exhibit nonideal connectivity and heterogeneity on pore size.[116-118] Natural fractures in shales can act as pores and more micropores in shale are created during fluid imbibition.[89, 119] Furthermore, shale can be clay rich, whose surface properties contribute to extra imbibition mechanisms rarely relevant in conventional porous medias.[120-121] The imbibing fluids' composition including salt type and concentration,[122-123] pH values,[124] barium content,[125-126] and the surface tension and viscosity can potentially play significant roles.[127]

Because of the above complexities, many conflicting and anomalous imbibition results are found in shales and they vary from sample to sample.[95] For example, laboratory observations of the slopes of imbibition curves shows a constant 0.25 in many samples from US, while those for samples from China have multiple regions with slopes varying between 0.1 and 0.5.[116, 128] Field observations diverge on whether the high salinity of flowback water comes from formation brine or is due to ion leaching from shale rock.[70, 124] These observations necessitate a comprehensive understanding of fluids imbibition in shales, which has been classified into four categories: capillary imbibition, osmosis, clay hydration, and other mechanisms.

Capillary imbibition. As shown in the Lucas-Washburn equation, the wettability or the contact angle of shale rocks is a main factor that regulates imbibition dynamics. Contradicting results are usually found between measured contact angle and imbibition rate in shale rocks.[86, 129-130] These results can be explained by three reasons that regulate the actual contact angle in shale matrix at micro- and nano scale.[95] The actual contact angle can be much smaller due to the surface force of thin liquid films between liquid and solid surfaces.[131] The rough surface can induce "tilt" in contact angle because water molecules tend to first fill hydrophilic area with lower contact angle.[132] Finally, the line tension effects may be important at nanoscale and their effect can be more significant than the surface tension.[133]

Beyond wettability/contact angles, two other factors can contribute to the observed different imbibition rates of capillary flow in shales. Because of their organic content, shales can be in mixed

or oil-wet. While traditional capillary imbibition will not occur for fluids in shale, a liquid drop can still enter the shale matrix when the droplet radius is below some critical value.[134] Although experimental evidence is lacking at present, this condition is thought to be satisfied in shales.[95] Additionally, as pores in shale exhibit surface roughness and are under confinement, surface friction can become important.[95] A surface friction coefficient can be used to account for this effect, which can be related to the effective viscosity of imbibing fluids.[118, 135-136]

Osmosis is the spontaneous net movement of solvent molecules (i.e. water) passing through semipermeable membranes (i.e. shale matrix) from the low solute concentration region into the high concentration region. As shown in Fig. 1-5b, the difference in solute concentration on the two sides of the semipermeable membrane creates a pressure gradient (osmotic pressure gradient) that moves water into the high salt concentration side. Quantitative relation between osmotic pressure and solute concentration can be found from the van't Hoff law.[137] Pores in shales can as semi-permeable membranes and the role of osmosis in imbibition has been investigated in shales.[138-139] However, due to the wide variety of pore size in shale, i.e. from micro-pores to macro-pores, the semipermeable property of shale is not ideal.[95] For example, it was estimated that the membrane efficiency of shale matrix ranges from 10% to 90% and osmotic pressure is thus always lower than the theoretical limit.[113, 139]

Clay hydration. Owing to the rich content of clay minerals, water can imbibe into shales by adsorbing on the basal crystal surface and interlayering spacing of clays. The hydration of clay surface usually consists of two stages.[119] The clay surface is normally negatively charged and with exchangeable cations.[95, 140] The first stage, known as *surface hydration*, occurs when the moisture content in the mineral surface is very low. Surface hydration is driven by the favorable hydration of the clay cations and by the liquid-solid interactions including hydrogen bonding and charge-dipole interactions.[140-141]

After the initial surface hydration is complete, cations are enriched near clay surface and

double layers are established (see Section 1.3.2), through which a concentration difference of dissolved ions between diffuse layers near clay surface and free bulk water is generated.[119, 142] The osmotic pressure from the concentration difference drives water further into the interlayer or outer-layer clay surface, which is known as *osmotic hydration*.[119] Both surface hydration and osmotic hydration are responsible for the hydration of clay surface, but surface hydration is dominant in the initial stage of water imbibition.[142] The swelling of clay is associated with hydration and it is suspected that micro-fractures in shale are generated by clay swelling.[89, 143] The imbibition of water into shale through clay hydration has been suggested. For example, some shale sample adsorbs more water than the initial measured pore volume, which was attributed to clay hydration.[89, 128]

Other mechanisms. Some additional mechanisms can be involved in the imbibition in shales. The micro-fractures should contribute to imbibition pathways in shale. Aside from the swelling of clays, the micro-fractures in shale can be created due to pore pressure developed by the imbibition fluids (including water and oil).[95, 144] It has been proposed that the pore pressure has an inverse relation with the aspect ratio of the pore.[145] Another possible mechanism is water evaporation, which may be facilitated in shale formations through the gas expansion during production, the significantly enhanced evaporation in shale's narrow pores, and the shift of thermodynamic equilibrium for evaporation in shale's confined space.[95]

Pore-scale study. In addition to laboratory and field observations, simulation investigations have also been performed on the liquid imbibition in shales. Currently, there is no single model that covers all imbibition mechanisms. A combination of more than more mechanism is preferred. For example, the effects of osmosis and creation of micro-fractures have been both included in some models.[146] Additionally, to represent a real shale, the pore network model that captures the complex pore connectivity and multiphase flow characteristic has been applied to model the imbibition in shales.[147]

In spite of these modeling studies, the imbibition mechanisms are not yet fully understood in

shales. Particularly, the imbibition process and dynamics of clay hydration are still unclear. To completely understand these mechanisms and effectively manage the dual aspects of liquid imbibition in shales, pore-scale study is desired for the following reasons. First, most of the mechanisms are induced by the surface of clay content and occurs at micro or nanoscale, which can be resolved in pore-scale study by using atomistic models. Second, the complexity of the investigated systems including pore size and heterogeneity and interplay of individual mechanism impedes the thorough understanding of individual mechanisms. At the single pore scale, these complexities can be largely excluded. Third, to ultimately integrate the different mechanisms at larger scales, the accurate description of each imbibition mechanism at single-pore scale is necessary.

1.2.4 Hydrocarbon transport

The transport of water discussed above is concerned primarily with the potential environmental damages caused by fracking fluids. The transport of hydrocarbons in shales is equally important as it governs the rate of hydrocarbon production and ultimate recovery fraction. The effective and optimal extraction of gas and oil from shales requires a robust understanding of the hydrocarbon transport in shales. In contrast to conventional porous media, the hydrocarbon transport in shale matrix is affected by several unique mechanisms originating from shales' small pore size and great heterogeneity. Because of the pressing need for efficient hydrocarbon recovery, the understanding of their transport in shale is relatively advanced and models spanning multiple scales have been successfully applied.

Adsorption and desorption. Natural gas exists in shale reservoirs as free gas, adsorbed gas, and dissolved gas.[148] Among the three states, the gas adsorbed on surfaces of organic and inorganic materials of shales contribute greatly to the total gas reserve,[149] e.g. it is found that 20-80% of the total gas is adsorbed gas in shales.[150] As the shale pressure declines, more gas will dissociate from the adsorbed state to become free gas and consequently the recovery rate of gas from shale is

affected by the gas adsorption and desorption.

The gas adsorption reflects the molecular accumulation of gas near shale surfaces to minimize their energy.[151] Gas adsorption is influenced by environmental condition (e.g. pressure and temperature) and shale's properties. A great number of isotherm models have been proposed to describe adsorption, including Langmuir-type models, Freundlich-type models, and Langmuir–Freundlich-type models.[152-157] In particular, Langmuir-type models are regarded as the simplest, and often most effective one. They have been reasonably calibrated and applied for modeling the adsorption of methane and other gas in shales.[158-159] The Langmuir isotherm is expressed as

$$V_{ads} = V_L p/\ (p + p_L), \qquad (1.2)$$

where V_{ads} is the volume of gas adsorbed under pressure p, V_L is the eventual adsorption amount, and p_L is the gas pressure when adsorption reaches half of the eventual adsorption amount.

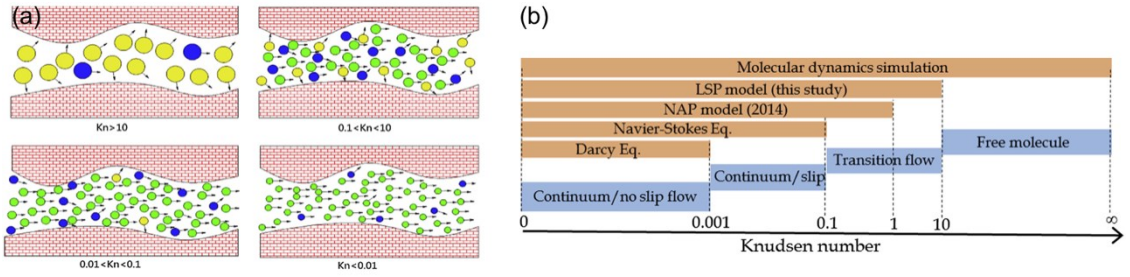

Figure 1-6. *Hydrocarbon flow regimes.* **(a)** Molecular illustration with gas transport through a pore throat with different Knudsen number. The yellow, blue, and green circles represent molecules engaged in molecule-wall collisions, molecule-molecule collision, advective molecular flux driven by pressure gradient. The arrows point to the momentum directions. **(b)** Different flow regimes as a function of Knudsen number. Panel (a) is taken from Ref. 160 with permission from Elsevier; panel (b) is taken from Ref. 161 with permission from Elsevier.

Flow mechanisms. The classical continuum description of flow by the Navier-Stokes equation and Darcy's law, which work well in conventional reservoirs, often become invalid in shales. Such deviation is often caused by the fact that the pore size in shales is comparable to the mean free path of the fluid molecules. The physics of gaseous hydrocarbon flow is typically controlled by the Knudsen number (K_n), which is defined as the ratio of the molecular mean free path of a gas molecule to the average width or diameter of a pore. As shown in Fig. 1-6, when K_n increases the

continuum flow becomes less suitable and various flow regimes not described by the continuum flow theories are found: continuous/no slip flow ($K_n < 0.001$); continuous/slip flow ($0.001 < K_n < 0.1$); transition flow ($0.1 < K_n < 10$); free molecule or Knudsen flow ($K_n > 10$).[162]

Klinkenberg effect. The slip length in typical bulk flow is usually small. In micro- and nano pores, slippage may become pronounced. The Klinkenberg factor was first proposed to account for the possible factors that lead to permeability enhancement of a shale sample to gas.[163] The slippage of gas on the pore wall is described through dependence of the apparent permeability on the pressure as

$$K_a = (1 + b/p)K_\infty, \quad (1.3)$$

where b is the Klinkenberg factor, p is the average pressure across the pore, and K_∞ is the absolute gas permeability. The Klinkenberg effect is expected to be more significant under high pressures and a non-Darcy effect is resulted in the slip flow regime. The Klinkenberg effect has been widely incorporated into simulations of low permeability rocks.[164] Many experiments on shale permeability have been performed to verify the existence of the Klinkenberg effect and obtain its necessary parameters.[165-166]

Knudsen diffusion. In the free molecule flow regime, the mean free path of the gas molecule is much larger than the pore size and gas-wall collision becomes more significant such that the viscous effect is negligible. Within the framework of Knudsen diffusion, the gas flux is given as a diffusion flux with a Knudsen diffusion constant.[167] The Knudsen diffusion constant is given by

$$D_K = \frac{2r}{3}\sqrt{8RT/\pi M}, \quad (1.4)$$

where r is the mean pore size, R is the gas constant, T is the temperature, and M is the molecular weight of the gas. The apparent or total gas flux can be calculated by combining Knudsen diffusion with the normal convective flux. In some cases, the Knudsen diffusion can fail when the pore size is very small, i.e. 1nm pore in mature kerogen. This failure can be caused by (1) the interactions between the gas molecules and pore walls can dominate the gas transport and

thus the kinetic theory-based Knudsen theory is no longer accurate and (2) the superlubricity effect, which arises when the molecules are only slightly smaller than the pore.[23]

Transition regime. No generally-accepted apparent permeability has been developed for gas flow in this regime due to its complexity. A correlation equation using a multiplier between the apparent permeability and K_n is proposed and widely used, from which many other correlations have also been advanced.[162] The multiplier is a function of the Knudsen number K_n and is commonly written as

$$f(K_n) = (1 + \alpha_1 K_n)(1 + 4K_n/(1 - \alpha_2 K_n)), \quad (1.5)$$

where α_1 and α_2 are two parameters related to the cross-section shape of the pore.

Surface diffusion. In addition to viscous flow and Knudsen diffusion, the transport of gas can be dominated by surface diffusion in nanopores with strong adsorption (i.e. pore radius < 2nm).[168] Surface diffusion is controlled by factors including pressure, temperature, surface heterogeneity, gas type, and gas-wall interaction.[168-172] The hopping model that takes the surface diffusion as an activated process of hoping between adsorption sites in the adsorption and desorption process and the Langmuir isotherm with single adsorption layer have been combined to describe the surface diffusion in shales.[173]

Numerical models. The flow mechanisms summarized above have been studied progressively at micro- and mesoscale using methodologies including molecular dynamics (MD) and Lattice Boltzmann method (LBM). MD treats gas particles explicitly and is applicable to model the flow at all Knudsen numbers (especially high K_n). For example, MD simulations have been used to study the adsorption/desorption and gas diffusion process in shales.[174-175] LBM method has been proven to be a powerful tool and applied in shale reservoirs, e.g. shales' transport properties can be obtained from LBM models when Knudsen diffusion is integrated into the model.[176] Furthermore, in the transition regime, the direct simulation Monte Carlo (DSMC) method that solves the Burnett equation based on high-order moments of Boltzmann equation is appropriate

and has been used to predict the gas flows.[177]

Treating shale as a network constituting of idealized elements such as pore bodies and throats, pore network models are capable of accounting for the pore size distribution and connectivity.[178-179] Prior to the flow simulation, a realization of the internal structure of rock samples is built using high resolution imaging and other methods (e.g. statistical construction, grain-based construction, and direct mapping model).[23, 180-181] The apparent permeability of the pore throats is usually corrected by considering gas slippage and Knudsen diffusion, though direct superposition of the two effects has been questioned.[182-184] At macroscale, given the inapplicability of Darcy's low due to the extremely low permeability in shale matrix, many innovative methods are available for gas flow modeling: dual mechanism models that include Darcy flow, Fickian diffusion, and dynamic gas slippage have been proposed; methods that refine the apparent permeability by applying a flow condition function of Knudsen number have been developed.[23, 185-186]

Multiphase issue. While existing studies have advanced the understanding of hydrocarbon transport in shales, many issues remain. One key issue is that the transport of hydrocarbon in shales often occurs in presence of water. The water may either be injected during the fracturing process or originally present in the shale. Nuclear magnetic resonance measurement of shale samples suggests the amount of water that is not structured by electrostatic force varies between shale samples and does not correlate with the overall porosity.[187] The presence of water can lead to transport physics different from that in conventional reservoirs. For example, water confined in shale nanopores can alter the flow pattern described by Darcy's law and lead to new gas transport pathways.[188-189] Therefore, it becomes necessary to account for the existence of the liquid water when studying hydrocarbon transport in shales.

Research resolving these multiphase transport phenomena at pore-scale or single-pore level is preferred. Reminiscent of the high Knudsen number for single-phase transport in shales, the capillary number can be large in shales with nanometer wide-pores because the interfacial effects

become dominate. In these cases, the classical continuum hydrodynamics may not be accurate and methods involving fewer assumptions than continuum hydrodynamics are needed. In addition, single-pore level studies can clarify the basic multiphase transport mechanisms, which can be incorporated into models at larger scales, i.e. the flow unit between two pore bodies in the pore network model. Consequently, these studies are a critical step towards a bottom-up, and rigorous understanding of the shale gas/oil extraction process. Regarding hydrocarbon recovery from shales, two key questions about the multiphase transport at single-pore level remain open.

Invasion of gas into water-filled pores. This process is opposite to the imbibition and is often encountered. For example, highly pressurized methane sometime must pass through water-saturated tight rocks featuring extensive nanopores before it can be recovered.[190-191] Of the few existing studies, most are experimental characterization of the gas invasion process into water-saturated rock samples.[192-193] While these studies provided valuable data on the gas invasion process in practical systems, the complexity of the systems studied makes it challenging to gain generalized insight into the gas invasion process. To address this challenge, studies of the gas invasion process at the pore scale are needed.

Invasion of droplet/bubble into water-filled pores. In shales, the solid boundaries are often preferentially wetted by water and the oil/gas phase is dispersed as droplets/bubbles.[194-195] The invasion of the gas/oil as bubble/droplets into nanopores and their subsequent transport plays an important role in shale gas/oil recovery. Previous studies have advanced the basic understanding of droplet invasion into pores, whose size is smaller than the droplets.[134, 196-201] However, new issues arise when the pores reach nanoscale dimensions, i.e. pores in shale environments. First, when a droplet enters a nanopore, a molecularly thin film likely forms between the droplet and the surface of the nanopore and a host of interfacial forces can emerge. To what extent these forces affect the free energy landscape of the droplet invasion is not clear *a priori.* Second, when an external pressure difference exists between the up- and downstream of the nanopore, much of the

prior work focused on identifying the critical pressure difference under which a droplet can deterministically enter the nanopore. However, when the size of the droplets and pores reaches nanoscale, where thermal fluctuations are significant, a droplet can potentially enter and translocate the nanopore by overcoming the energy barrier through thermal activation. Delineating the free energy landscape for droplet transport through nanopores in presence of a pressure difference, which has received limited attention in prior works, thus becomes important.

1.3 Enhanced Recovery from Conventional Reservoirs

1.3.1 Low salinity water flooding

For conventional hydrocarbon sources, the average recovery factor from oil fields around the world is somewhere between 20% and 30%, while that of gas fields is between 80% and 90%.[202] Enhanced oil recovery (EOR) has been a hot topic in conventional hydrocarbon extraction for years. EOR typically involves injecting chemicals (fluids, nanoparticles, polymers, *etc*) into oil reservoirs to achieve oil recovery better than that based on traditional pressure maintenance methods. Amongst the various techniques, low salinity waterflooding (LSW) has attracted great attention because it is more economically applicable and environmentally viable than many other methods, e.g. chemical flooding, thermal flooding, and CO_2 flooding. In practice, low salinity brine is injected under secondary and tertiary conditions after the displacement of oil in place using high salinity seawater or produced water.[203]

LSW studies began several decades ago. In one of the earliest report, it was suggested that fresh water is favored over brine for heavy oil displacement.[204] From 1990s, the potential of LSW starts to be recognized from experimental work, where oil recovery rate is found to depend on water composition.[205-207] In recent years, the benefit of LSW becomes widely recognized. For instance, it is generally believed that, in sandstones, LSW can increase the oil recovery rate by 5-20% of the original oil in place.[208] Based on a large number of laboratory tests and field observations, the conditions favoring effective LSW are summarized as the presence of clays,

presence of polar oil, presence of initial water, presence of divalent in the initial brine, and salinity shock.[209-214] However, it is also recognized that these conditions neither guarantee effective LSW, nor are all required for successful deployment of LSW in a given field.

Diverse mechanisms of LSW have been proposed, e.g. fines migration, pH effect, multicomponent ionic exchange (MIE), double layer expansion (DLE), wettability alteration, osmosis, and salting effect.[215] Importantly, these mechanisms are not exclusive of each other; most of them are both supported and disapproved by evidences or counter-evidences in different cases; none of them alone will necessarily lead to success in LSW.[209, 216-217] Due to the complex interactions and compositions within oil-brine-rock (OBR) systems, there has been no consensus about which one of them is the dominant mechanism. Recently, wettability alteration is emerging as the most widely accepted mechanism for LSW.[208-209, 214, 218-220]

Wettability change from oil-wet to mixed-wet in carbonates and from water-wet to mixed-wet in sandstones has been reported in LSW studies.[221] Based on data mainly from sandstones, the mechanisms of wettability change may include pH effect,[222] MIE,[213] DLE,[223] and some additional chemical mechanisms.[220] In carbonates, these mechanisms are not directly applicable but can be triggered by calcite dissolutions.[224] At present, it is unclear which of these mechanisms dominates wettability alteration. Some researchers believe that DLE is the leading mechanism in sandstones and carbonates.[223, 225-226] The idea is that the double layer interactions between oil and rock is universal, whereas other mechanisms appear under narrower and more restricted conditions.[227] It is thus important to understand how DLE contributes to wettability alteration in OBR systems.

1.3.2 Double layer expansion

The wettability alteration in OBR systems refers to the increase of the macroscopic contact angle of oil droplets on rock surfaces. The reservoir rock primarily consists of sandstone or carbonate. The sandstone (e.g. quartz) surfaces are negatively charged at most pH values.[228] The carbonate surfaces can be charged by various processes, i.e. the dissolution of calcium ions from

calcite.[229] The oil-brine interface can be charged by ionization of the polar groups of polar oil or more complex mechanisms for nonpolar oil.[230-231]

A key feature of OBR systems is that a thin brine film usually separates the oil droplets and rock surfaces, as shown in Fig. 1-7a.[232-233] The thickness of these films depends on the nature of rock surfaces, the brine composition, and the properties of the oil droplets, and can range from a few angstroms to tens of nanometers.[234-235] For example, using small-angle neutron scattering, it was shown that water films with a thickness of ~0.8-1.3nm exist on the surfaces of silica particles dispersed in heptane using anionic surfactants.[235] Because the rock-brine and brine-oil interfaces are charged, electrical double layers (EDLs) appear inside the brine films.

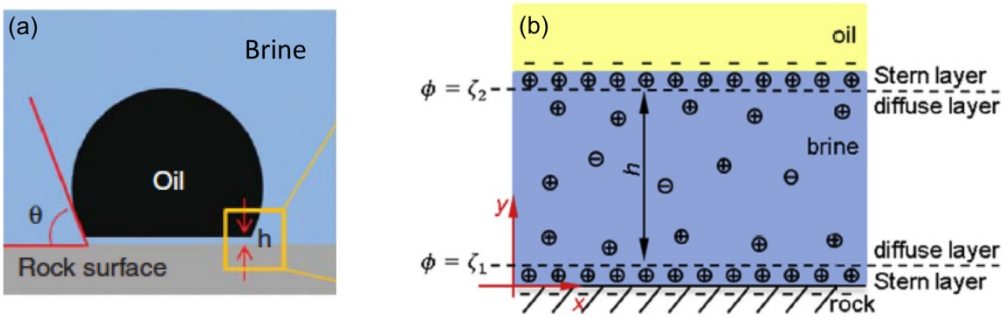

Figure 1-7. *Oil-brine-rock system in enhanced oil recovery.* **(a)** Schematic representation of oil droplet on rock surface, which are separated by a thin brine film. **(b)** The schemes for classical EDLs between oil and rock. h is the film thickness. Panel (a) is taken from Ref. 236 with permission from the Society of Petroleum Engineers; panel (b) is taken from Ref. 227 with permission from Elsevier.

Figure 1-7b shows the classical description of planar EDLs between rock and oil. The first layer of EDL is formed both at the charged rock and charged oil surfaces. The second layer includes counter-ions and co-ions from brine, which are attracted and repelled from the two charged surfaces separately. The second layer can be divided into an inner part of Stern layer and an outer part of Gouy-Chapman or diffuse layer.[237] The Stern layer is layer of counter-ions that are directly adsorbed to the charged surface and is often thought to be immobile,[238] but recent studies suggest that counterions in the Stern layer can have finite mobility. The plane that separates the Stern layer and diffuse layer is called outer Helmholtz plane, at which the electrical potential is defined as the zeta potential and denoted as $\phi = \zeta_1$ and $\phi = \zeta_2$ near the two surfaces. Numerous theories have

been developed for the diffuse layers in EDLs, and the simplest and most widely used theory is the Poisson-Boltzmann (PB) equation.

In the PB equation, the solvent is treated as a continuous media with certain dielectric constant and ions are treated as point charges. The charge density ρ_e and electric potential ϕ are related by Poisson equation as $\nabla \cdot (\varepsilon_0 \varepsilon_r \nabla \phi) = -\rho_e$, where ε_0 and ε_r are the vacuum permittivity and relative permittivity separately. The local ionic space charge density is $\rho_e = \sum_i eN_A z_i c_i$, where e is the electron charge, N_A is the Avogadro number, and z_i and c_i are the valence and concentration of the *i*-th ion, separately. According to the Boltzmann distribution, the local ion density is given by $c_i = c_{i0} \exp(-z_i e\phi / k_B T)$, where c_{i0} is the bulk ion concentration, k_B is the Boltzmann constant and T is the absolute temperature. Assuming a uniform dielectric constant in space, the PB equation in the diffuse layer becomes

$$\nabla^2 \phi = -\frac{eN_A}{\varepsilon_0 \varepsilon_r} \sum_i z_i c_{i0} \, exp(-z_i e\phi / k_B T). \qquad (1.6)$$

Nondimensionalization of the PB equation gives a characteristic length termed the Debye length: $\lambda_D = \kappa^{-1} = (\varepsilon_0 \varepsilon_r k_B T / 2N_A e^2 I)^{1/2}$, where $I = \sum_i c_i z_i^2 / 2$ is the ionic strength. The Debye length is an intrinsic length scale of any electrolyte and it characterizes at what distances a charge is screened in an electrolyte.

The EDLs and their response to salinity reduction play a fundamental role in the wettability alteration. Within the brine films, surface interactions lead to effective interactions between the oil and rock phase that are usually called the disjoining pressure, which tend to separate the water and oil phases (if the interactions tend to bring the two phases together, the disjoining pressure is negative and often called conjoining pressure). The disjoining pressure consists primarily of van der Waals forces and EDL forces, both of which are usually described using classical Derjaguin-Landau-Verwey-Overbeek (DLVO) theory. Non-DLVO forces including structural forces and other forces also contribute to the disjoining pressure.[239] On the basis of the augmented Young-Laplace equation or the Young-Dupré equation, the disjoining pressure in the brine films

sandwiched between the oil droplet and the rock surface determines the contact angle.[226-227, 233]

The contribution of the EDL forces to the disjoining pressure can be obtained by solving the PB equation across the brine film with proper boundary conditions. For two surfaces interacting through a liquid film, constant charge and constant potential are commonly assumed for the two surfaces as they approach each other. These approximations are not as rigorous as the charge regulation theory, but they have been widely used due to their simplicity.[239] For example, with the constant charge assumption, the EDL force across the film is identical to that given by the contact value theorem, which takes a very simple form that depends only on the ion concentration at the surface.[239] Various forms of EDL disjoining pressure have been worked out for different boundary conditions.[226, 240] Particularly, a linear superposition approximation between constant charge and constant potential assumptions is favored for fitting surface force, and it is given by

$$\Pi_{EDL}(h) = 64 n_b k_B T \times tanh(\zeta_1/4) tanh(\zeta_2/4)\, exp(-h/\lambda_D), \quad (1.7)$$

where $n_b = N_A \sum_i c_i$ is total bulk ion density and ζ_1 and ζ_2 are the zeta potentials shown in Fig. 1-7b.[239-240] This relation, however, only works for film with thickness larger than the Debye length, that is $\kappa h > 1$. As the salinity decreases, λ_D increases (i.e. the double layer expands) and $|\zeta_1|$ and $|\zeta_2|$ usually increase too. Consequently, lowing brine salinity tends to enhance the EDL disjoining pressure in thin brine films, which in turn makes the rock more water-wetting and the contact angle of oil droplets on the rock surface larger. It is important to note that, even though Equ. 1.7 and the DLVO theory built upon it (or its other variants) can predict the trend of Π_{EDL} rather robustly, they may not be quantitatively accurate (especially at high salinity) in terms of the predicted magnitude and decay length of Π_{EDL}.[226-227, 241-242] This, along with the fact that the variation of the surface potential and charge with salinity is not well understood,[226, 243] makes the quantitative prediction of DLE an outstanding challenge.

The role of DLE in wettability alteration has been extensively verified in experiments through zeta-potential measurement. The measured zeta-potential generally becomes more negative as the

salinity is lowered, for many brine compositions (containing either monovalent or divalent cations and even only deionized water) and at many sandstone surfaces (including Berea and clay). The more negative zeta-potential is strongly correlated with a more water-wetted state and improved oil recovery.[244-248] Zeta-potential measurements in carbonate systems also confirmed the occurrence of DLE during LSW and further suggested that DLE is more significant at higher temperatures.[249-250] Apart from zeta-potential, direct force measurement also supports that DLE is responsible for wettability change.[251-252]

While DLE is widely considered as a key mechanism for LSW, different opinions do exist. For example, some experiments showed that wettability does not change consistently with brine concentration and experimentally measured film thickness of deionized water is not the optimal one among different brine concentrations.[232, 247-248, 253] These results point to the inherently complex interactions in OBR systems and the inadequate understanding of individual mechanism like DLE.

1.3.3 Understanding thin brine films in OBR systems

The lacking of a thorough mechanistic understanding on LSE or more specifically on DLE originates from the inaccurate description of the interaction between oil and rock. Such interaction is usually determined by the interfacial structure at OBR systems. In addition to thermodynamics of EOR including their structure and disjoining pressure, the dynamics of brine films are expected to play a crucial role in determining the kinetics of LSW.[236, 254] Insights on the structure, thermodynamics, and dynamics of brine films in OBR systems can potentially help improve existing EOR techniques and/or formulate new EOR concepts. While such insights may be derived from prior works on thin liquid films in other systems, some unique situations in OBR systems can make this approach difficult.

With the sub-nanometer film thickness,[235] the brine films exhibit two interesting features. First, these brine films are confined by a solid rock with a rigid surface and an oil phase with a soft,

diffusive surface. Second, the thickness of these brine films is comparable to key intrinsic length scales of the brine solution, brine-rock interfaces, and brine-oil interfaces (e.g. the Debye length of brine, the hydration diameter of the ions in brine, the characteristic length of the density oscillation of water molecules near rock surfaces, and the width of diffuse brine-oil interfaces). The combination of these features makes these brine films highly unique, and it is thus difficult to extrapolate the insights obtained in the studies of other thin liquid films to them.

In principle, MD simulations, in which the thin brine film, oil, and rock are resolved with atomistic scale, can be used to gain insights into the molecularly thin brine films in OBR systems. The MD simulation provides plentiful interfacial information on the OBR systems at a fundamental level and allows for exclusive investigation on one mechanism, i.e. DLE. Many questions on the structure, thermodynamics, and dynamics of brine films found practical OBR systems can be explored in MD systems. For example, the molecular structure of rock-brine and brine-oil interfaces in the film is unknown, especially under the condition that the two interfaces approach at a molecular thickness. Little information is available on the ion distribution in EDLs and its response to the change of bulk ion concentration and film thickness. Furthermore, the behavior of the disjoining pressure inside such thin film and the contribution of EDL forces as well as the response with film thickness and bulk ion concentration are not immediately clear.

1.4 Scope of This Dissertation

From the previous sections, it is clear that, during both the recovery of gas/oil from shale reservoirs and the low-salinity waterflooding of conventional oil reservoirs, several interfacial and multiphase transport phenomena are encountered: the imbibition of water into nanopores filled with pressurized gas, the transport of gaseous and liquid hydrocarbon into water-filled nanopores, and the expansion of the thin brine films in OBR systems. To promote technological advancement on hydrocarbon extraction, a fundamental understanding of these phenomena is important. In this dissertation, the above phenomena are studied at the single-pore level, acting as a key step toward

up-scaling and comprehensive description of hydrocarbon extraction process at pore network, core, and field scales.

The first study explores the imbibition of water into single mica nanopore when capillary flow is suppressed. Water is found to imbibe into the nanopore through surface hydration in the form of monolayer liquid propagation on the mica surface. The propagation of the imbibition fronts follows a diffusive scaling law with an effective diffusion coefficient much larger than the self-diffusion coefficient of water in the monolayer. These observations are understood with the help of a thin film growth theory and analysis of the energetics of water in the monolayer, bulk, and near mica surfaces immersed in water. The transition of imbibition from the surface hydration to the capillary flow regime is also clarified.

The second study examines the invasion of methane gas into water-filled mica pores with widths of 2-6nm. Gas invades into a mica pore only when the pressure exceeds a breakthrough pressure and a thin residual water film is left on the mica wall after gas enters the pore. The gas breakthrough pressures can be predicted by the capillary pressure if the finite thickness of residual liquid water film and the disjoining pressure in the thin residual water film are considered. The movement of the front of the liquid meniscus during invasion can be described using the classical hydrodynamics if the negative slip length on the mica surface is taken into account.

The third study examines how a droplet enters water-filled nanopores. The free energy profile for droplet invasion and how the profile is affected by the applied pressure difference and the size of the droplet and nanopore are clarified. For nanopores whose surface is fully wetted by water but not the droplet phase, a droplet larger than the pore diameter must overcome a higher free energy cost than that predicted by classical theories due to the large disjoining pressure. When the droplet is smaller than the pore size, and thus the droplet is usually expected to enter the pore freely, a large energy barrier for droplet entrance can nevertheless exist.

The fourth study focuses on the molecularly thin brine films in OBR systems. The structure of

the interfacial water, oil, and the electrical double layers within the films with a thickness of 0.74 and 0.94nm are delineated. The evolution of the electrical double layer structure as the liquid film is thinned is understood by computing the dielectric constant in the films and with the help of the Poisson-Boltzmann equation. The disjoining pressure between the charged rock surface and the oil is quantified. The relative contribution of hydration and EDL forces to the disjoining pressure as well as their presumed additivity are analyzed in detail. The shear viscosity of the thin brine film and the slippage between the brine film and the oil phase are quantified.

The rest of the dissertation is organized as follows. Chapter 2 presents the imbibition of water into nanopores through surface hydration. Chapter 3 presents the invasion of gas into water-filled mica nanopores. Chapter 4 presents the thermodynamics of droplet invasion into nanopores filled with water. Chapter 5 presents the interfacial structure, disjoining pressure, and dynamic properties of thin brine films in OBR systems. Finally, conclusions are draw in Chapter 6.

Chapter 2. Water Imbibtion through Surface Hydration

Disclosure

Major part of this work has been published by the Royal Society Chemistry: C. Fang, R. Qiao, Surface hydration drives rapid water imbibition into strongly hydrophilic nanopores. *Phys. Chem. Chem. Phys.* 2017, 19 (31), 20506-20512.

2.1 Introduction

Imbibition and infiltration of liquids into nanopores play a critical role in diverse applications including lab-on-chip, oil and gas recovery, smart textiles, and energy storage.[255-258] In recent years, driven by the advancement in nanochannel fabrication and computational methods,[259] there has been a surge of interest in understanding these phenomena beyond the classical interpretation pioneered by Lucas and Washburn a century ago. Indeed, research on these phenomena has evolved into one of the most exciting frontiers in the nanofluidics field, with new phenomena discovered and new fundamental insights offered. For example, even though the classical Washburn law, in which the movement of the imbibition front exhibits a square root law scaling, has been confirmed in smooth nanopores,[260] qualitative and quantitative deviations from this law have also been identified.[101-106] In particular, slippage at liquid-wall interfaces,[103, 107-108] disjoining pressure in liquid films,[107, 109] electroviscous effects,[101, 110] enhanced viscosity of interfacial or highly confined fluids,[111] and contact angle hysteresis[112] have been shown to greatly affect liquid imbibition into nanopores.

Most of the existing studies focused on imbibition associated with capillary flows. However, imbibition can also occur via other mechanisms. In particular, surface hydration, the imbibition of water into nanopores driven by the affinity of water molecules to strongly hydrophilic pore walls, can lead to water imbibition without involving capillary flow.[261] Despite the potential relevance of surface hydration in technically important problems such as water management in shale gas recovery operations,[95, 262] a fundamental understanding of such imbibition is limited at present.

In this work, we investigate the imbibition of water into slit mica nanopores filled with highly pressurized methane using molecular dynamics (MD) simulations. Since the capillary pressure is smaller than the initial gas pressure inside the pore, imbibition through capillary flow is suppressed. Nevertheless, water is imbibed into the pore through surface hydration in the form of a monolayer liquid film before the imbibition front reaches the pore's end. We show that the growth of the imbibition front driven by surface hydration follows a simple diffusive scaling law. Interestingly, the effective diffusion coefficient for the growth of the imbibition front is more than an order of magnitude larger than the self-diffusion coefficient of the water molecules in the thin water film adsorbed on pore walls. With the help of a molecular theory, we clarify the mechanism underlying the rapid water imbibition observed during surface hydration.

2.2 Simulation System and Methods

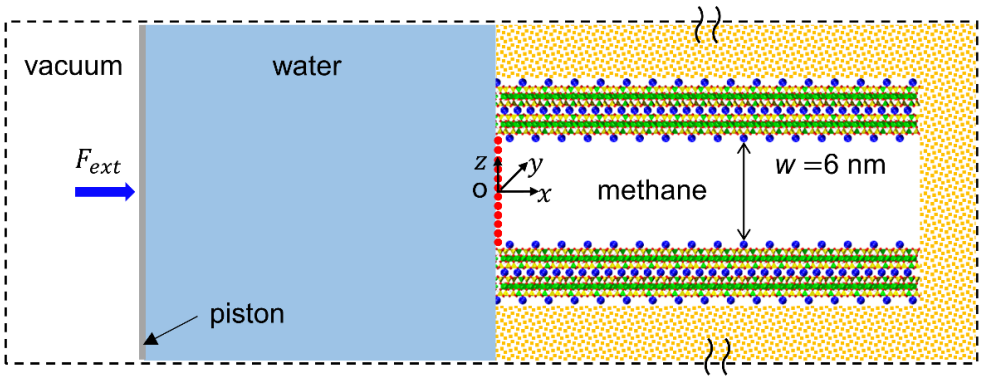

Figure 2-1. *A schematic of the system for studying water imbibition into slit mica pores*. The pore is initially separated from the water reservoir by blocker atoms (red dots) and filled with methane. The pressure in the reservoir is controlled using a piston. Implicit walls (denoted by the golden slabs) are used to model the mica away from the imbibed water. The dashed lines denote the periodical simulation box. At $t = 0$, the blocker atoms are removed to initiate water imbibition. x=0 corresponds to the pore entrance. The figure is not drawn to scale. A 3D view of the system is shown in *Appendix A*.

System and simulation protocol. Figure 2-1 shows a schematic of the MD system for studying the imbibition of water into a slit-shaped nanopore. The system consists of a water reservoir and a slit pore cleaved from mica, which is a good model for strongly hydrophilic materials. The pore is 6nm wide, 3.15nm deep in the y-direction, and 20.2nm long in the x-direction. The right end of the

pore is sealed. The system is periodical in all three directions. To reduce the effects of periodicity on water imbibition, the simulation box is 36.5nm long in the pore length direction. Initially, the pore is separated from the water reservoir by "blocker" atoms at its entrance (the red dots in Fig. 2-1) and is filled with methane at 250bar. The pressure of the water reservoir is controlled using a piston to 5bar. The MD system is first equilibrated for 1ns. Next, the blocker atoms are removed to initiate water imbibition (this time instant is defined as t=0), and the system is run for 8ns to study the water imbibition. We note that the imbibition of fluids into the pore is not driven by the pressure applied on the piston. Indeed, we found that different applied pressure (e.g. 10bar) on the piston does not notably affect the water imbibition as long as capillary flow into pore is suppressed.

Molecular model. To reduce computational cost, only the horizontal pore walls that can come into contact with the imbibed water molecules are modeled atomistically. The other portion of the pore walls that do not directly affect the water imbibition are modeled as implicit walls (see below). Each of the atomistic walls is made of two muscovite mica layers (~2nm thick) so that the water-wall interactions are captured accurately. Muscovite ($KAl_2Si_3AlO_{10}(OH)_2$) is a phyllosilicate clay.[18] Each muscovite layer has a tetrahedral-octahedral-tetrahedral (TOT) structure, in which each Al-centered octahedral sheet is sandwiched between two Si-centered tetrahedral sheets. The neighboring TOT structures are held together by a potassium interlayer. Following the widely used method for building surfaces and nanopores from muscovite minerals, we cleave the muscovite such that its surface features K^+ ions and is rich in bridging oxygen atoms.[18, 263]

Water and methane are modeled using the SPC/E model and the TraPPE force fields.[264] The partial charges and LJ parameters for the mica atoms are taken from the CLAYFF force fields.[18, 265] The TraPPE force fields enables accurate prediction of methane's thermodynamic properties. In addition, prior works showed that the CLAYFF force fields allow the surface hydration of clay surfaces under equilibrium conditions to be accurately simulated.[263, 266] The interactions among mica atoms are excluded. Atoms in the clay sheets in contact with methane or water are tethered

with a stiff spring to their lattice sites. Other atoms in the mica walls are fixed. For the portion of the mica wall modeled implicitly, their interactions with the methane molecules and the oxygen atoms of water molecules are computed using the LJ 12-6 potential

$$E(s) = 4\epsilon\left[\left(\frac{\sigma}{s}\right)^{12} - \left(\frac{\sigma}{s}\right)^{6}\right], \qquad (2.1)$$

where s is the separation between a methane molecule (or the oxygen atom of a water molecule) and the surface of the *nearest* implicit wall. To mimic strongly hydrophilic walls, σ=0.287nm and ϵ=6.23kJ/mol are adopted for the water-wall and the methane-wall interactions.

All simulations are carried out using the LAMMPS code[267] in the NVT ensemble (T=300K). The equations of motion are solved using a time step of 1fs. The vibrating mica atoms are kept at a constant temperature using a Nose-Hoover thermostat. Bond lengths and angles of the water molecules are kept fixed using the SHAKE algorithm. The temperature of the water and methane molecules are maintained using the dissipative particle dynamics (DPD) thermostat which has the advantage of preserving hydrodynamics.[108] Non-electrostatic forces are computed using the cutoff method (cutoff length: 1.2nm). Long-range electrostatic forces are computed using the particle-particle particle-mesh (PPPM) method[268] with a relative accuracy of 10^{-5}.

2.3 Results and Discussion

Imbibition dynamics. Figure 2-2a shows that, after the blocker atoms at the pore entrance are removed, the methane gas expands into the water reservoir to form a bubble at the pore entrance, and its size remains relatively unchanged during the simulation. The flow of water across the full pore width is not observed. Instead, water enters the pore as two thin liquid films and the length of these thin films grows with time. In principle, the film growth can occur by two processes. First, the water molecules in the film can propagate along the pore's two walls and thus the liquid film extends deeper into the pore with time. Second, water molecules in the meniscus and/or liquid film can enter the gas phase, transport into the pore interior and subsequently adsorb on the pore wall.[269] We carefully examined the simulation trajectory and find that the second process contributes

negligibly to the growth of the liquid film in the system studied here. We envision that this second process may become important in wide pores and at higher temperature because both evaporation and transport of water molecules are facilitated in these situations.

Since the liquid film growing laterally on the pore wall is about one molecule thick (see below) and thus the concept of hydrodynamic flow is not readily applicable, the water imbibition observed here is best regarded as surface hydration. Importantly, the imbibition observed here is truly a surface phenomenon and its dynamics does not depend on the pore width. The idea is corroborated by two observations. First, the thickness of the water film on the pore walls is <1nm, which is much smaller the pore width. Hence, the water film on one pore wall does not "see" the other pore wall. It follows that the effect of one pore wall on the growth of water film on the other pore wall is negligible – as far as the film growth is concerned, the pore width is not important here. Second, the thin liquid film propagating into the pore resembles the thin precursor films ahead of liquids imbibed into a pore by capillary flow or a spreading droplet,[260, 270-272] whose occurrence does not depend on the width/length of pore or the size of the droplet either. As we shall see later, the growth of the imbibed water film in the present simulations follows the same scaling law for those precursor films. As long as the imbibition front does not reach the pore's dead end, the pore length has no impact on the imbibition dynamics either. Therefore, although water imbibition is simulated in a relatively narrow and short pore, the insight gained here is also relevant to imbibition into wider and longer pores.

To quantify the dynamics of imbibition, we compute the evolution of the number of water molecules imbibed into the pore $N(t)$ and the propagation of the imbibition front $h(t)$ along the pore walls. To determine $h(t)$, we first compute the area density of water molecules on the pore walls as a function of distance from the pore entrance, $\rho_s(x,t)$, by taking advantage of the fact that the imbibed water molecules form a thin film on the pore walls. Next, we scan $\rho_s(x,t)$ from pore interior toward the pore entrance, and the imbibition front $h(t)$ is marked as the position at

which $\rho_s(x,t)$ exceeds a threshold value of $\rho_s^{th} = 0.4\text{nm}^{-2}$. Figure 2-2b shows that $h^2(t)$ increases linearly with time, i.e. the movement of the imbibition front follows a diffusive scaling law $h(t) \sim t^{1/2}$. Using a diffusive growth law $h(t) = \sqrt{2D_e t}$ and the data in Fig. 2-2b, the effective diffusion coefficient D_e of the growth of the imbibed water film's length is found to be $6.02 \times 10^{-9}\text{m}^2/\text{s}$. Figure 2-2b shows that the growth of the amount of imbibed water molecules also follows a diffusive scaling law, i.e $N^2(t) \sim t$ or $N(t) \sim t^{1/2}$. Together, these results show that the imbibition of water into a nanopore by surface hydration is a dynamic process observing a diffusive scaling law. It is useful to note that such a scaling law is also observed for the spreading of precursor films ahead of liquids imbibed into a pore via capillary flow or a spreading droplet.[260, 272]

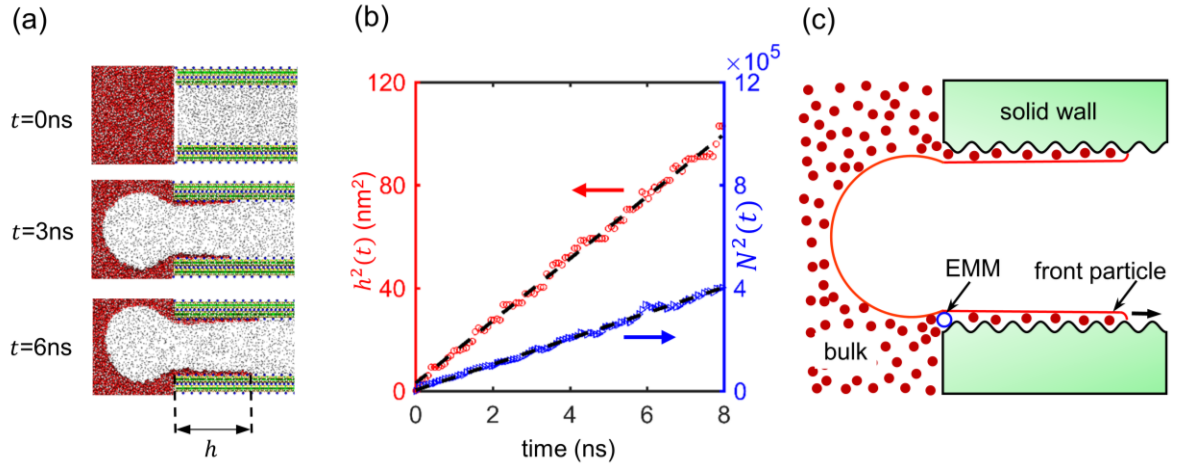

Figure 2-2. *Dynamics of imbibition driven by surface hydration*. (**a**) Snapshots of the system near the pore entrance during imbibition. Water is imbibed into the pore as thin films on the pore walls. (**b**) Evolution of the imbibition front $h^2(t)$ and the number of water molecules imbibed into the pore $N^2(t)$ as a function of time. The imbibition exhibits a diffusive scaling law since $h^2(t)$ and $N^2(t)$ increase linearly with time. (**c**) A schematic of the molecular model for the propagation of thin liquid films on wetting solid substrates developed by Burlatsky, Oshanin, Cazabat and Moreau. This panel is adapted from Ref. 273.

To further delineate the imbibition process, we quantify the temporal and spatial distribution of hydration water layer propagating on the pore walls. Figure 2-3a shows the evolution of the average water density profiles normal to the lower mica wall in two selected patches along the pore (patch A: x=1.5-2.5nm; Patch C: x=3.5-4.5nm). We observe that the imbibed water forms a

single layer on the pore walls. After the imbibition front moves past a patch on the pore walls, the thickness of the water layer in that patch does not increase but the amount of water adsorbed there can still increases. For example, at t=1ns, the imbibition front already reaches the surface patch C located at x=3.5-4.5nm, but more water molecules become adsorbed on the surface patch A located at x=1.5-2.5nm till t~7ns. Similar trend is evident in Fig. 2-3b, which shows the temporal evolution of the area density of water molecules in several patches on the pore wall.

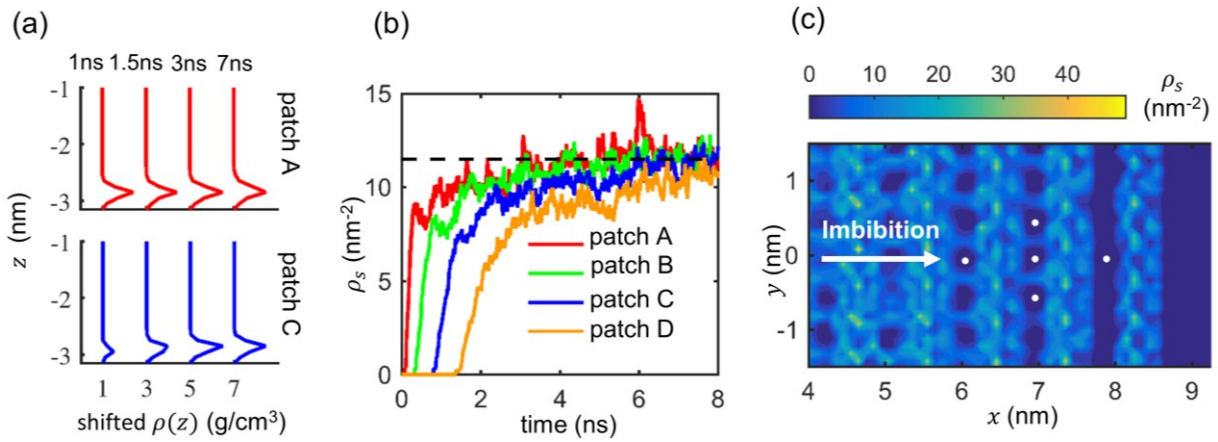

Figure 2-3. *Temporal evolution and spatial distribution of hydration water on pore walls during imbibition.* (**a**) Evolution of the water density profile normal to the lower mica wall in two surface patches of the wall (patch A: x=1.5-2.5nm; patch C: x=3.5-4.5nm; x=0 corresponds to the pore entrance). The water density profiles at t = 1, 1.5, 3, and 7ns are *shifted up* by 1, 3, 5, and 7g/cm^3 for clarity. z = -3nm corresponds to the position of the surface K^+ ions on the lower mica wall. (**b**) Growth of the area density of hydration water in different patches along the mica wall (patch A: x=1.5-2.5nm; patch B: x=2.5-3.5nm; patch C: x= 3.5-4.5nm; patch D: x=4.5-5.5nm). The dashed line denotes the asymptotic area density of water on the wall. (**c**) The distribution of water density on a portion of the pore walls at t=6.5ns. Some of the K^+ ions on the mica surface are identified using white dots. The position of water molecules is determined based on their oxygen atom.

These results imply that, although surface hydration-driven imbibition involves the propagation of a monolayer water film along the pore, the density of the water film is not a constant. In fact, the water monolayer behind the imbibition front densifies as the imbibition front moves forward. To see this from a different perspective, we compute the area density of the water molecules adsorbed on the pore wall, $\rho_s(x,y,t)$, at a representative time of t=6.5ns, when the imbibition front has reached x = 9.0nm. Figure 2-3c shows $\rho_s(x,y,t)$ near the imbibition front. While the surface sites

in the region 8nm<x<8.6nm are occupied by many water molecules, the interstitial spaces between the surface K^+ ions behind the imbibition front are only sparsely populated by water molecules. As one moves from the imbibition front toward the pore entrance, the interstitial spaces between the surface K^+ ions become more densely populated by water molecules. Together, the results in Fig. 2-3b and 2-3c show that, as the imbibition front moves forward, the most favorable surface sites near the imbibition front are hydrated by water molecules first and the less favorable surface sites behind the imbibition front gradually become hydrated by water molecules. Consequently, while the thickness of the water film is nearly uniform over the pore walls, the density of the water film decreases as one moves from the pore entrance toward the imbibition front.

Molecular model of surface hydration. The essential features of the imbibition dynamics revealed in Fig. 2-2 and 2-3 can be captured by the thin film growth theory developed by Burlatsky, Oshanin, Cazabat, and Moreau two decades ago.[273] This theory considers the growth of a single molecule-thick liquid film originating from a stationary liquid meniscus (see Fig. 2-2c). It was postulated that the growth of a molecularly thin film is governed by the diffusive transport of vacancies from its front to the edge of the macroscopic meniscus (EMM). The analytical model building on this idea predicts that the liquid density (molecular vacancy) in the thin film increases (decreases) as the one moves from the tip of the propagating film toward the EMM, which is observed in our simulations. Moreover, in agreement with the imbibition characteristics shown in Fig. 2-2b and c, solution of the analytical model indicates that the growth of the liquid film follows a diffusive scaling law, i.e. the growth of the total mass of the liquid film and the movement of the liquid film's front both follow a square root law. For example, the front of the liquid film $h(t)$ moves along the solid substrate by

$$h(t) = \sqrt{2A_m D t}, \qquad (2.2)$$

where D is the diffusion coefficient of liquid molecules in the thin film. On homogeneous solid substrates, A_m is a constant controlled by two energies: the energy gained by moving a liquid molecule from the interior of the macroscopic meniscus into a vacancy site at EMM ($E_\downarrow$) and the

work needed for moving a vacancy at the tip of a laterally propagating liquid film ($W_{\leftarrow}$) to the EMM (see Fig. 2-2c). It follows that the propagation of the liquid film's tip exhibits an effective diffusion coefficient of $A_m D$, and this effective diffusion coefficient is affected by the liquid-substrate interactions at the EMM and at the front of liquid film. A key prediction of the theory, which has not been examined thus far to our best knowledge, is that A_m can be either smaller or larger than one depending on the value of $E_{\downarrow}$ and $W_{\leftarrow}$.[273] Given that the theory captures the qualitative aspect of surface hydration well, we next investigate quantitatively how large A_m is in the present system, and in particular, whether A_m may be larger than one. To this end, we first examine the diffusion of water molecules in monolayer water films adsorbed on mica surfaces.

Dynamics of water molecules in thin films. We perform *separate* equilibrium simulations in which a layer of water molecules is placed on the mica walls (see *Appendix A*). The area density of water molecules is set to the asymptotic water density on the mica surface at positions far behind the imbibition front observed in Fig. 2-3b. Figure 2-4a shows the mean square displacements (MSDs) of the water molecules in *x*- and *y*- directions, which give diffusion coefficients of D_x=0.42×10^{-9} m^2/s and D_y=0.6×10^{-9}m^2/s in the *x*- and *y*- directions, respectively. Both D_x and D_y are much smaller than that of bulk water (D_{bulk}=2.54×10^{-9}m^2/s), in good agreement with prior reports.[274-276]

To understand the slow diffusion of water molecules adsorbed on the mica surface and its anisotropicity, we compute the potential of mean force (PMF) of water molecules adsorbed on the mica wall (see *Appendix A*). Figure 2-4b shows that the free energy landscape for water molecules diffusing over the mica wall is highly corrugated. Because of the strong hydrogen-bonding between water molecules and the bridging oxygen atoms on the mica surface and between water molecules and the surface K^+ ions (see Fig. 2-4b), there are distinct free energy valleys near the bridging oxygen atoms and surface K^+ ions. Meanwhile, the protrusion of surface K^+ ions from the mica wall creates free energy hills above the K^+ ions and saddle points between vertically

aligned K^+ ions (see Fig. 2-4b). When performing random walks over such a corrugated energy landscape, water molecules are often trapped into local energy minimums (see trajectories of representative water molecules in Fig. 2-4b), hence exhibiting slow diffusion. The anisotropicity of water diffusion in the *x*- and *y*- directions originates from the anisotropicity of the PMF: because the free energy landscape is more corrugated in the *x*-direction (see Fig. 2-4b), the diffusion in *x*-direction is slower.

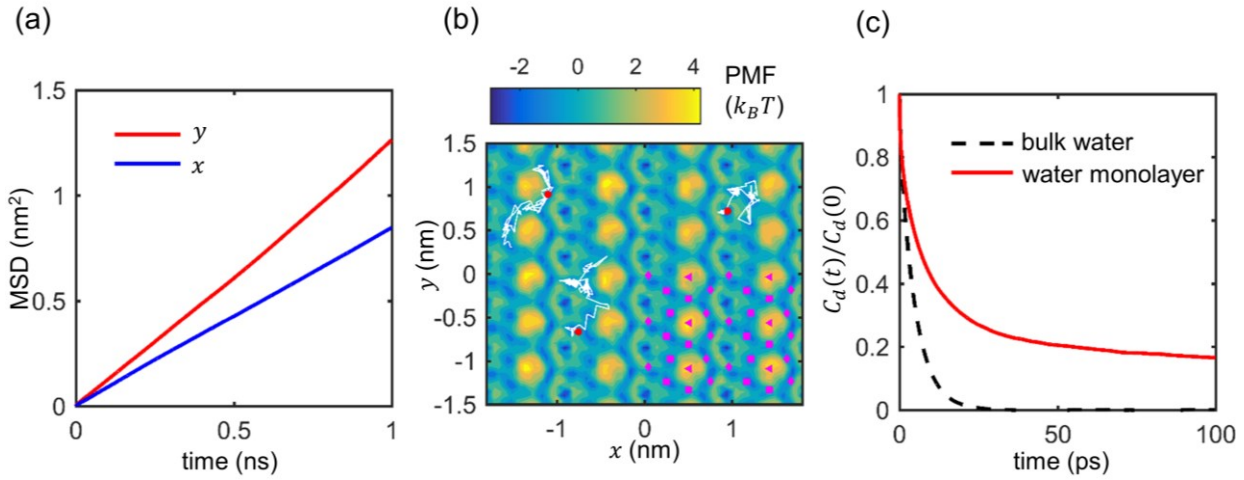

Figure 2-4. *Dynamics of water molecules in the water monolayer adsorbed on planar mica surfaces*. (**a**) The mean square displacement (MSD) of water molecules in x- and y-directions. (**b**) The trajectory of three representative water molecules over 200ps. The red dots denote the initial position of the water molecules. The trajectory is overlaid on the color-coded PMF plot of the water molecules on the mica surface. The magenta markers in the right bottom corner denote some of mica's surface atoms (K^+ ions: triangle; bridging oxygen: square; bridging oxygen with tetrahedral substitution: diamond). **(c)** The dipole autocorrelation function (dashed line is for water molecules in bulk) of water molecules.

In addition, because of the strong, directional interactions between water molecules and the bridging oxygen atoms and surface K^+ ions on the mica walls, water molecules often adopt preferred orientation with respect to these atoms, which hinders their free rotation. This is evident from the dipole autocorrelation function $C_d(t)$ of water molecules shown in Fig. 2-4c. For water molecules in the bulk, $C_d(t)$ decays to zero in ~20ps. However, for water molecules adsorbed on the mica surface, their $C_d(t)$ reaches only ~0.3 by 20ps, and decays very lowly after that. Since the translation of water molecules over the heterogeneous surface of a mica wall inevitably requires

them to rotate from time to time, the retardation of the rotation of water molecules hinders their translational diffusion.

Accelerated diffusion of the imbibition front. We now return to the dynamics of imbibition driven by surface hydration. Using the effective diffusion coefficient for the growth of imbibition front and the D_x of the water molecules computed above, it follows from Equ. 2 that A_m~14, i.e. the growth of the imbibition front is greatly accelerated compared to the diffusion of individual water molecules in single-molecule thick hydration layer. This thus supports the prediction of Burlatsky *et al.*'s theory that A_m can be larger than 1. Based on their theory, this large A_m indicates that $E_{\downarrow} \gg k_B T$ and $W_{\leftarrow} \ll k_B T$ ($k_B T$ is the thermal energy) in our system. $E_{\downarrow}$ is the energy gain when a water molecule is moved from bulk to fill a vacancy at the EMM. Hence $E_{\downarrow} \gg k_B T$ corresponds to strong liquid-substrate attractions. $W_{\leftarrow}$ is the cost of moving a vacancy from the tip of the imbibed film to the EMM. In the theory by Burlatsky *et al.*, this cost is equivalent to the difference of the energies lost and gained due to the forward (i.e. moving away from the EMM) and backward hop of the front molecule of the imbibed film.[273] Computing $E_{\downarrow}$ and $W_{\leftarrow}$ is difficult because, unlike in the theory where molecules are assumed to occupy defined lattices, water molecules are randomly distributed on the mica wall in our simulations and thus vacancies are not well-defined. Nevertheless, we can gain insight into $E_{\downarrow}$ and $W_{\leftarrow}$ by examining the energetics of water molecules in mica-water systems and thus better understand the accelerated diffusion of the imbibition front.

To gain insight into $E_{\downarrow}$, we note that the liquid structure at EMM is intermediate between that of the water at the interface of a thick water layer and a mica surface and that of a monolayer water film adsorbed on a mica wall. Therefore we compute the potential energy of a water molecule when it is located at three positions: in bulk water (E_1), in the first interfacial water layer near mica wall hydrated by a thick slab of water (E_2), and in a monolayer water film adsorbed on a mica wall (E_3, the water density here is equal to the asymptotic water density in the imbibed water film shown

in Fig. 2-3b). Snapshots of the water molecules at these positions and their microenvironments are shown in Fig. SA-2 in *Appendix A*. A value of -18.65, -21.38, -19.58k_BT is obtained for E_1, E_2, and E_3, respectively. In particular, E_2 and E_3 are 2.73 and 0.93 k_BT smaller than E_1, respectively. This indicates that when a water molecule moves from bulk to the EMM, the increase of its potential energy due to the reduction of its number of neighboring water molecules is compensated by its strong attraction by the mica wall. This strong attraction of water by the mica wall is consistent with the strong electrostatic interactions between the water molecule and the charged sites on the mica wall. To qualitatively understand $W_{\leftarrow}$, we next compute the potential energy of an isolated water molecules adsorbed on the mica wall (E_4), and find it to be lower than E_3 by 3.00k_BT. Therefore, it is energetically favorable for a water molecule at the imbibition front to hop forward. Specifically, when a water molecule at the imbibition front hops forward, its potential energy tends to increase because it loses the coordination by neighboring water molecules. However, at the same time, this water molecule improves its coordination with the charged sites on the mica surface (see Fig. SA-3 in *Appendix A*), and thus its potential energy due to interactions with the mica surface becomes more negative. The latter effect is more significant and hence forward hopping is energetically favorable. While the net free energy cost for a water molecule at the imbibition front to hop forward can still be positive because isolated water molecules are confined tightly to selected surface sites and thus suffer an entropy penalty, the forward hoping should be a facile process and hence $W_{\leftarrow}$ is small. Overall, the above results show that the accelerated diffusion of the imbibition front compared to the diffusion of individual water molecules in thin water films adsorbed on mica walls (i.e. $A_m > 1$) is caused by the strong attraction of water molecule by the mica walls. In the present study, the pore walls are homogeneous in both physical structure and chemical nature, and thus A_m is a constant. For pore walls with heterogeneous surface properties, A_m may not be a constant.

Capillary effects. In finite length-pores, the imbibition fronts eventually reach the pore's end. To study the imbibition in such situations, we repeat the above simulations in a system featuring a

short, 5.5nm-long mica pore. The end of the pore, modeled using an implicit wall, is made hydrophilic by adopting a 12-6 Lennard-Jones (LJ) potential with a deep energy well for the water-wall interactions (see Methods). Visualization of the trajectory indicates that the imbibition fronts hit the pore's end at $t \approx$ 2ns. Thereafter, the imbibition fronts on the lower and upper walls move upward and downward along the vertical wall at the pore's end, respectively, till they meet at the center of the vertical wall. During this period, water molecules accumulate in the corner at the pore's end (see Fig. 2-5a). Such an accumulation is driven primarily by capillary effects. Specifically, similar to that in capillary condensation, water tends to accumulate in corners with large curvature because the chemical potential of the liquids in these corners is lowered by capillary pressure. The reduced chemical potential of water molecules in the corner further drives the transport of water molecules from the water reservoir into the pore.

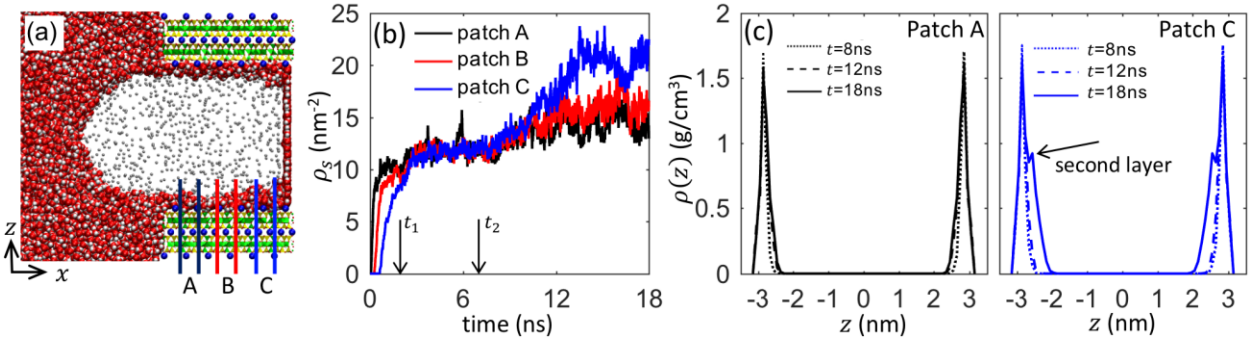

Figure 2-5. *Dynamics of imbibition after the imbibition fronts reach pore end*. (**a**) A snapshot of the MD system at t =18ns (the pore's dead end is strongly hydrophilic and modeled using an implicit wall). (**b**) Growth of the total area density of the hydration water in different patches of the mica wall (patch A: x = 1.5-2.5nm; patch B: x =2.5-3.5nm; patch C: x = 3.5-4.5nm; x = 0 corresponds to the pore entrance). t_1 and t_2 denote the instants when the imbibition fronts hit the pore's end and when the upper and lower surface film meet, respectively. (**c**) Evolution of the water density profile across pore in two patches on the mica surface.

Figure 2-5b shows that, the water film in the pore interior (i.e. closer to the pore's end) grows faster than that near the pore entrance. To examine the growth of the water film in more details, we compute the water density profile across the pore at different position along the pore wall. Figure 2-5c shows that, very close to the entrance (patch A: 1.5nm< x <2.5nm), the water film only densifies marginally after the imbibition front reaches the pore's end and remains one-molecule

thick till t=18ns. Near the pore's end and close to the corner (patch C: 3.5nm< x <4.5nm), the growth of the water film is more significant, and a second layer is developed by t=18ns. Clearly, imbibition continues after the entire pore wall is hydrated by monolayer water films. The growth of the water films follows a layer-by-layer mode, in which a second layer is developed on top of the first hydration layer. The water film grows from the pore interior toward the pore entrance, with the second hydration layer first developing near the pore's end rather than its entrance.

2.4 Conclusions

In summary, we studied the imbibition of water into mica nanopores filled with pressurized methane gas using molecular dynamic simulations. While capillary flow through the pore's full cross-section is suppressed, water invades the pore as monolayer water films propagating on the pore walls. In the first stage, water invades the pore as monolayer water films propagating on the pore walls. The growth of the imbibition front during this surface hydration-dominated process follows a diffusive scaling law. The effective diffusion coefficient of the growth of the imbibition front is more than one order of magnitude larger than that of individual water molecules in the water film, which is attributed to the fact that the interactions between water molecules and mica walls are stronger than that between water molecules in the water film and in bulk. After the imbibition fronts on the two walls of the pore meet at the end of pore, the imbibition transitions to the second stage. Here, water molecules first preferentially accumulate at the corners and the water film on pore walls thickens by gradually adding extra water layer, first at position near the pore's end and then at position near the pore entrance. The capillary effects become important in this second stage because, by lowering the pressure (hence the chemical potential) of the water in the corner at the pore's end, it drives the transport of water into the pore.

In the present study, we considered only the imbibition of water into mica pores through surface hydration. The scaling law revealed here should be applicable to the imbibition of fluids as thin liquid films when other imbibition modes (e.g. capillary flow) is suppressed. However, for such

imbibition to occur, the fluid molecules must show strong affinity to the solid surface (e.g. if the fluids show complete wetting on the surface). This condition is similar to that for the formation of a precursor film ahead of a spreading droplet or the liquids imbibed into a pore by capillary flow, and it is embodied in the requirement that the term $E_{\downarrow}$ in Burlatsky *et al*'s model must be large. If the pore walls are made of materials much less hydrophilic than mica, this condition may not be met and thus water transport through surface hydration may not occur.

Supporting Information

All supporting information cited in this chapter is located in *Appendix A*.

Chapter 3. Invasion of Gas into Water-Filled Mica Nanopores

Disclosure

This work has been published by the Institute of Physics: C. Fang, F. Zhang, R. Qiao, Invasion of gas into mica nanopores: a molecular dynamics study. *J. Phys. Condens. Matter* 2018, 30 (22), 224001.

3.1 Introduction

The transport of multiphase fluids in nanopores plays a critical role in diverse areas including lab-on-chip, oil and gas recovery, smart textiles, and energy storage.[255-256, 258, 277] Driven by the technical needs in these areas and the advancements in nanochannel fabrication and computational methods,[259] there has been a surge of research activities in understanding these phenomena. In particular, much attention has focused on the imbibition and infiltration of fluids (both spontaneous and forced) into nanopores. These researches have revealed rich imbibition dynamic ranging from recovering the classical Washburn law in some systems to qualitative and quantitative deviations from the classical law in other systems. [102, 104-106, 278-280] For parameters such as the critical pressure for the infiltration of water into hydrophobic pores, it has been shown that the classical Young-Laplace equation cannot accurately predict the threshold pressure for carbon nanotubes.[281-283]

While the imbibition and infiltration of fluids into gas-filled pores have received much attention, the opposite process, i.e. the invasion of gas into liquid-filled pores, has received much less attention. Such a process is encountered in practical applications. For example, in shale gas recovery, the highly pressurized gas such as methane must sometime pass through water-saturated tight rocks featuring extensive nanopores before it can be recovered.[190-191] Of the few existing studies, most are experimental characterization of the gas invasion process into water-saturated rock samples.[192-193] While these studies provided valuable data on the gas invasion process in practical systems, the complexity of the systems studied (e.g. heterogeneity of surface properties and size of the pores in the rock samples) makes it challenging to gain generalized insight into the

gas invasion process. To address this challenge, studies of the gas invasion process at the pore scale can be very useful.

Two important aspects of the invasion of gas into a liquid-filled pore are the gas breakthrough pressure P_B (i.e. the pressure above which gas can invade into the pore) and the dynamics of gas invasion at pressure higher than P_B. The breakthrough pressure is often taken as the capillary pressure given by the Young-Laplace equation, i.e. $P_B = 2\gamma\cos\theta\,/R$ for a cylindrical pore and $P_B = 2\gamma\cos\theta\,/W$ for a slit pore, where γ is the interfacial tension of the gas-liquid interface, θ is the contact angle. R (W) is the radius (width) of cylindrical (slit) pore. The dynamics of the gas invasion into the pore is typically described using the Navier-Stokes equation with bulk liquid and gas properties. While these approaches should be accurate for wide pores, their accuracy in narrow nanopores is not immediately clear. For example, recent studies showed that the surface tension of liquids confined in nanopores can deviate from that of bulk liquids,[284] and the viscosity of fluids confined in nanopores is non-uniform across the pore and can be much higher than that of bulk liquids.[111] Given these interesting phenomena, it is useful to examine the invasion of gas into nanopores without making the assumptions in the classical approaches widely used in the literature.

In this work, we use molecular dynamics (MD) simulations to investigate the invasion of gas into mica nanopores with widths of 2, 4, and 6nm. We determine the gas breakthrough pressure and the dynamics of gas invasion and compare our observations with classical theories. The rest of this manuscript is organized as follows. In Section 3.2, the molecular model and simulation details are presented. In Section 3.3, the thermodynamics and dynamics of the gas invasion including the gas breakthrough pressure and invasion dynamics are discussed. Finally, conclusions are drawn in Section 3.4.

3.2 Simulation Details

Figure 3-1 shows a schematic of the MD system for studying the breakthrough of methane gas into a slit-shaped nanopore initially filled with water. The system consists a slit pore cleaved from

a mica slab and two reservoirs at the pore's two ends. Initially, the left reservoir features both a gas phase (methane, 8nm thick in the *x*-direction) and a liquid phase (water, 2nm thick in the *x*-direction). The large volume of methane molecules in the left reservoir ensures that the gas molecule can fill the entire slit pore after gas breakthrough occurs. The right reservoir only contains water (3nm thick in the *x*-direction) initially. The desired pressure in the reservoirs is regulated by applying the necessary forces to the two rigid pistons bounding the reservoirs. The dimensions of the pore in the *x*- and *y*-directions are 14.7nm and 3.15nm, respectively. The pore width, defined as the distance between the surface potassium ions on the upper and lower mica walls (see Fig. 3-1), is $W = 2$, 4, and 6nm in different simulations. The MD system is periodic in all three directions. To effectively model systems that are periodic only in the *y*- and *z*-directions, two large vacuum spaces are placed outside the rigid pistons.

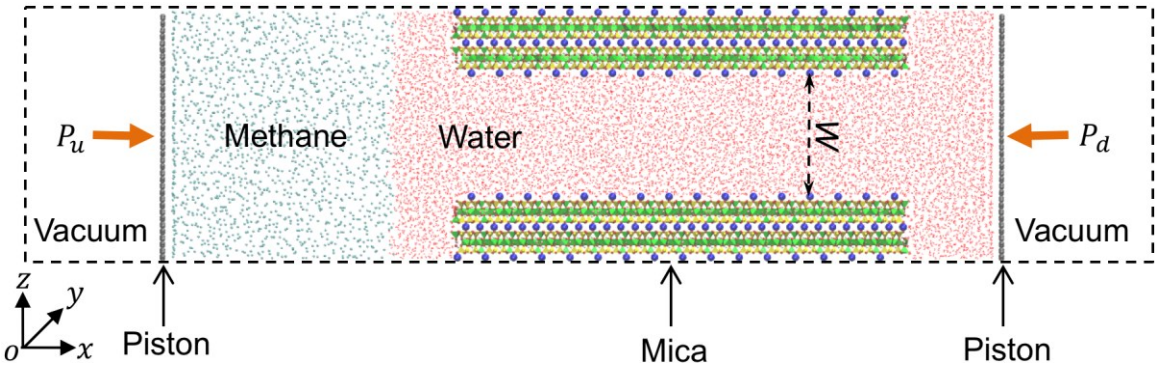

Figure 3-1. *A snapshot of the molecular dynamics system for studying gas invasion into mica pores.* The left reservoir is initially filled with 8nm thick (along *x*-direction) methane gas and 2nm thick (along *x*-direction) water. Water also fills the pore and a 3nm thick region (*x*-direction) in the right reservoir. Two rigid pistons are used to regulate the pressure in the two reservoirs. The pore is cleaved from bulk mica with a wall thickness of ~2nm. The pore width W (W=2, 4, and 6nm) is the distance between the surface potassium ions (shown as blue spheres) of the two mica walls. The pore length is 14.7nm. The system is periodic in all three directions and the length in the *y*-direction is 3.1nm. Two large vacuum spaces are placed in the *x*-direction so that the system measures 40nm (W=2, 4nm) or 45nm (W=6nm) in the *x*-direction.

Each of the walls is made of two muscovite mica layers (~2nm thick) so that the liquid-wall interactions are captured accurately. Muscovite ($KAl_2Si_3AlO_{10}(OH)_2$) is a phyllosilicate clay and can be easily cleaved from the (001) plane.[189] Each muscovite layer has a tetrahedral-octahedral-

tetrahedral (TOT) structure, in which each Al-centered octahedral sheet is sandwiched between two Si-centered tetrahedral sheets. Substitution of every four Si atoms in the tetrahedral layer by Al atoms results in a negative net charge, which is compensated by the K^+ ions. The neighboring TOT structures are then held together by a potassium interlayer. Following the widely used method for building surfaces and nanopores from muscovite minerals, we cleave the muscovite from the (001) plane, resulting in a surface featuring K^+ ions.[189, 263] For simplicity, the surface K^+ ions are arranged in ordered fashion following the previous approach.[285-286]

Water and methane are modeled using the SPC/E model and the TraPPE force fields,[264] respectively. The partial charges and LJ parameters of the mica atoms are taken from the CLAYFF force fields.[189, 265] The TraPPE force fields enable accurate prediction of methane's thermodynamic properties. Prior works showed that the CLAYFF force fields allow the interfacial water on clay surfaces to be accurately modeled.[263, 266] The interactions among mica atoms are excluded. All atoms in the clay sheets are tethered with a stiff spring. The piston atoms are modeled as Lennard-Jones atoms with parameters taken from those of the sp^2 carbon atoms in the OPLS-AA force fields. All force fields parameters are summarized in the Supplemental Material.

Simulations are carried out using the Gromacs package[287] in the NVT ensemble with a temperature T=400K. The temperature adopted here is relevant to that encountered in shale gas fields.[288] The temperature of the system is maintained using the velocity-rescaling thermostat.[289] The equations of motion are solved using a time step of 2fs during equilibrium runs and 1fs during non-equilibrium runs. Bond lengths and angles of the water molecules are fixed using the SETTLE algorithm. A cutoff 1.2nm is used for computing the Lennard-Jones potential and the particle mesh Ewald method is used for computing the electrostatic interactions.[290]

The MD system is first equilibrated for 4ns with $P_u = P_d = P$ on both pistons (see Fig. 3-1). For the 2nm-wide pores, P is set to 100MPa; for the 4nm- and 6nm-wide pores, P is set to 60MPa. To initiate the invasion of methane gas into the nanopores, the pressure on the right piston

(P_d) is reduced while P_u is not changed. Note that, although using a lower pressure on the left piston (P_u) is desirable, a high value is adopted because a lower pressure will require an extremely large volume of gas to be used in the simulations. Given that water has very low compressibility, adopting a relatively high P_u does not notably affect the gas invasion.

3.3 Results and Discussions

3.3.1 Gas breakthrough characteristics

Figure 3-2a shows the snapshots of methane gas breaking into pores with widths of 2, 4, and 6 nm when the pressure difference between the up and down-stream reservoir (ΔP_{ud}) is sufficiently high. As the gas invades into the pores, a gas-water meniscus forms and moves toward the downstream reservoir. Importantly, as the meniscus moves downstream, a thin film of water is left on the mica surface. Such a liquid film forms due to the affinity of water to the strongly hydrophilic mica surface.[286, 291] The formation of this residual film is akin to the formation of precursor films ahead of the moving meniscus when water is imbibed into pores (or when water droplets spread on substrates) with strongly hydrophilic walls.[271, 278, 292] In pores narrower than a few nanometers, such thin residual films occupy a substantial portion of the pore space. Moreover, as we shall see in *Section 3.3.2*, these thin residual films affect the critical gas breakthrough pressure in these narrow pores. Given the importance of these residual films, we characterize them in detail below.

We first compute the density distribution of the water residual film in direction normal to the mica wall. We focus on the portion of the water film 1.0nm away from the pore entrance and one pore width behind the moving meniscus, in which it has a nearly uniform thickness. In each pore, the density distribution is found to vary little once ΔP_{ud} exceeds a critical breakthrough pressure P_B when the gas just begins to be able to break into the pore. Figure 3-2b shows the water density distribution across the thin residual films (note that the surface K^+ ions are located at z=0) inside the 2, 4, and 6 nm pores. The density profiles show that water molecules can reach up to 1.0nm above the mica surface. For z < 0.2nm, the density profiles are practically identical in all pores; at

z > 0.2nm, the water density becomes larger as the pore becomes wider, i.e. the residual water film thickens in wider pores. To quantify such a thickening, we follow the concept of the Gibbs dividing surface, and determine the residual film thickness by equating the surface excess from both the liquid and vapor sides along the wall normal direction z[293]

$$\int_{-\infty}^{h}[\rho_l - \rho(z)]dz = \int_{h}^{W/2}[\rho(z) - \rho_v]dz, \qquad (3.1)$$

where ρ_l and ρ_v are the densities of the saturated bulk liquid water and water vapor at 400K, respectively. ρ_l is taken to be 31.3nm^{-3} based on independent simulations and ρ_v is taken as zero because it is much smaller than ρ_l. Using the density profiles shown in Fig. 3-2b, the thicknesses of the residual water films are determined as h=0.35, 0.49, and 0.54nm for 2, 4, and 6nm pores, respectively.

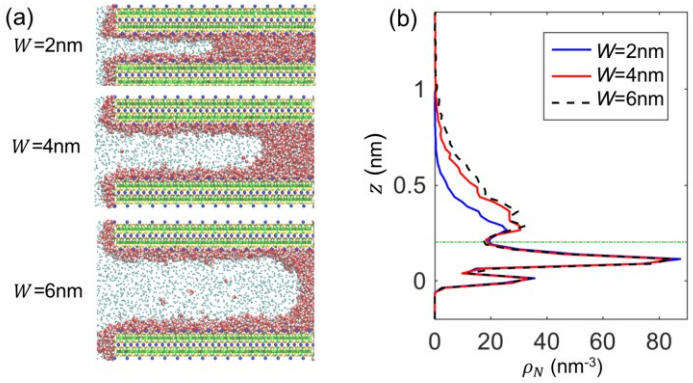

Figure 3-2. *Invasion of gas into water-filled mica pores*. **(a)** The snapshots of gas invasion into the 2, 4, and 6nm-wide pores. Methane molecules are shown as light blue spheres and water molecules are shown as red (oxygen) and white (hydrogen) spheres. The mica wall is the same as [that] in Fig. 3-1. **(b)** The number density profiles of water across the residual water films on the walls of the 2, 4, 6nm-wide pores (in the 2nm-wide pore, P_u=100MPa and P_d=10MPa; in the 4nm-wide pore, P_d=60MPa and P_d=20MPa; in the 6nm-wide pore, P_u=60MPa and P_d=40MPa.) The dashed line marks the water density valley at z=0.2nm, below which the water number density profiles are identical for the three pores.

To clarify the thickening of the residual film in wider pores, we delineate the evolution of the residual water film when the pore size increases by examining the organization of water molecules in the film. By inspecting the snapshots of the water molecules in the residual water film (e.g. see Fig. 3-3a), one can identify two layers of water molecules in the residual film based on how the water molecules in the residual film interact with other molecules. The inner layer (z<0.2nm)

consists of the water molecules hydrating the surface K^+ ions (cf. the density peak at $z \sim 0.1$nm) and the water molecules in the interstitial space between the surface K^+ ions (cf. the density peak at $z \sim 0.02$nm). The outer layer consists of the water molecules that interact with the inner water layer.[263, 286] These two layers of water molecules can also be visualized by computing their distribution as a function of their radial and vertical distance from the surface K^+ ions (see Fig. 3-3b; the surface K^+ ions are located at $(r, z) = (0, 0)$ and denoted by magenta dots).

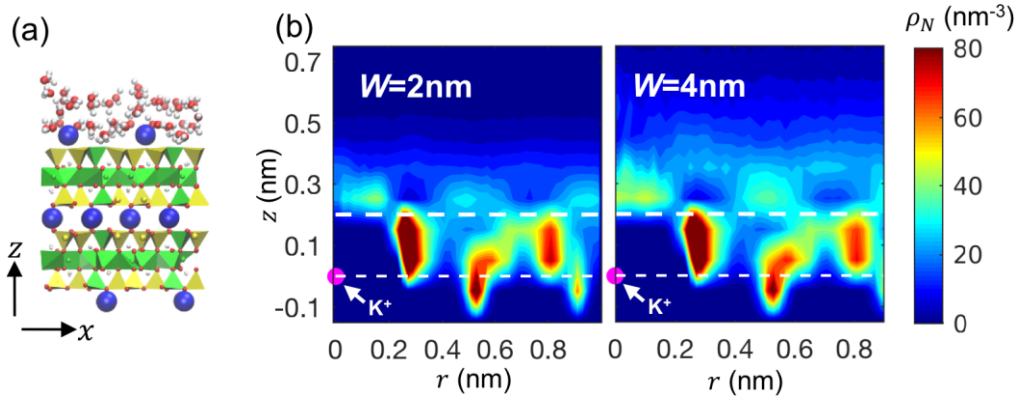

Figure 3-3. *Molecular structure of the residual water film on mica walls.* (**a**) A zoom-in view of the residual water layer near the mica wall of a 4nm-wide pore. The color coding is the same as Fig. 3-1 and Fig. 3-2a. (**b**) The number density distribution of water around mica's surface potassium ions in a cylindrical coordinate (r and z represent the radial and vertical distance of water molecules to the potassium ions, respectively). The number density distribution is calculated for the residual water film in W=2nm pore and W=4nm pore. The center potassium ions are shown in magenta dots. The position of the surface potassium ions (z=0) and the boundary for the inner/outer layer (z=0.2nm) is marked as dashed white lines.

Figure 3-2b and Fig. 3-3b show that, as the pore width increases from 2 to 4nm, the inner water layer hardly changes but the outer water layer becomes more distinct, i.e. the residual film grows by adding more water molecules to its outer layer without densifying or loosening its inner layer. This growth mode helps explain why the residual film becomes thicker as the pore width increases from 2 to 4nm. When gas breaks into a nanopore, the residual liquid films behind the meniscus are in quasi-equilibrium with the downstream water reservoir. Because the gas phase in contact with the residual film is at higher pressure than in the downstream reservoir, it tends to elevate the chemical potential of the water molecules inside the residual film above that in the downstream

reservoir, and thus thins the residual film. However, the strong interactions between the water molecules in the residual film with the mica surface make these water molecules energetically more favorable to stay in the residual film. The competition of these two processes results in a stable residual film with finite thickness. In narrow pores (e.g. W=2nm), the gas breakthrough pressure is high and thus the pressure of the gas phase in contact with the residual water film is high. Therefore, only water molecules interacting very strongly with the mica surface (i.e. mostly the inner water layer in Fig. 3-3b) can be stabilized. In wider pores (e.g. W=4 and 6nm), the pressure of the gas phase in contact with the water film is lower and thus even water molecules in the outer layer, which interact primarily with the inner water layer, can be stabilized. Therefore, the thickness of the residual water film increases as the pore becomes wider. We note that the thickening of the residual water film in larger pores is not influenced by the different P_u used in these simulations. Separate simulations show that, when the P_u increases to 100MPa in the 4nm-wide pores (P_d is increased accordingly), the film thickness is almost unchanged (see Fig. SB-1 in the *Appendix B*). Together, the thicker residual water films in larger pores should originate largely from the lower breakthrough pressures.

Thus far, we examined the basic process of gas invading mica pores and the formation of residual water film on pore walls. Below we examine two aspects of the gas invasion quantitatively: the gas breakthrough pressure and the dynamics of gas invasion into the mica pores.

3.3.2 Gas breakthrough pressure

For each mica pore, a series of simulations with different ΔP_{ud} are performed to check whether gas breakthrough occurs. A gas breakthrough occurs if continuous gas flow into the pore is observed. Once gas invades into a pore for more than the pore width W, the simulation is terminated. For cases in which gas breakthrough was not observed, the MD simulations are run for at least 20ns. The simulation results are summarized in Fig. 3-4, in which ΔP_{ud} corresponding to observation of gas breakthrough is marked using blue stars and those corresponding to no gas

invasion into the pore is marked using red squares.

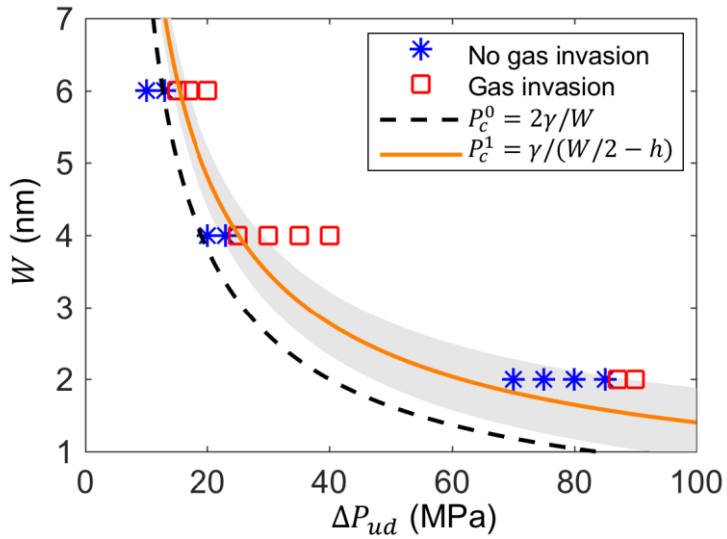

Figure 3-4. *Gas breakthrough pressure in different pores*. The pressure difference at which gas can (cannot) invade into the pore is shown as blue stars (red squares). The prediction of the gas breakthrough pressure by the classical capillary theory $P_c^0 = 2\gamma/W$ is shown as a dashed line. The prediction by considering the narrowing of pores by the residual water film $P_c^1 = \gamma/(W/2 - h)$ is shown as a solid line. The shaded area denotes the range of possible gas breakthrough pressure due to the ambiguity of assigning a thickness to the thin water films on the pore walls, which is in turn caused by the diffuseness of gas-liquid interfaces.

To check if gas breakthrough can be predicted using the capillary pressure (i.e. $P_B = P_c^0 = 2\gamma \cos\theta\ /w$), we note that separate simulation indicated that water droplets spread completely on the mica wall, i.e. θ=0. Since the methane-water interfacial tension depends on temperature and pressure, independent equilibrium simulations are performed to determine γ. In these simulations, a 4nm-thick slab of water is sandwiched between two 2nm slabs of methane (see Fig. 3-5). The number of methane molecules in the system is adjusted to give a methane pressure of 60, 80, and 100MPa, which is in the range of gas pressure in the gas breakthrough simulations. Each system is periodic in all three directions and the simulations are run in the NVT ensembles at three different temperatures. The methane-water interfacial tension is evaluated using $\gamma = 1/2\int_0^{Lx}[P_{xx} - 0.5(P_{yy} + P_{zz})]dx$,[294] where L_x is the length of the simulation box in the direction normal to the water-methane interface (x-direction), P_{xx}, P_{yy}, and P_{zz} are the three diagonal components of the pressure tensor along the *x, y,* and *z*-directions, respectively. To verify our calculations, we

also compute the water-vacuum interfacial tension in a similar system at 300K, and obtain a value of 61.4±0.9mN/m. This value agrees well with that in the literature for the same water model (60.7mN/m), and it is lower than the experimental value (72.8mN/m) mainly due to the choice of the water model.[294]

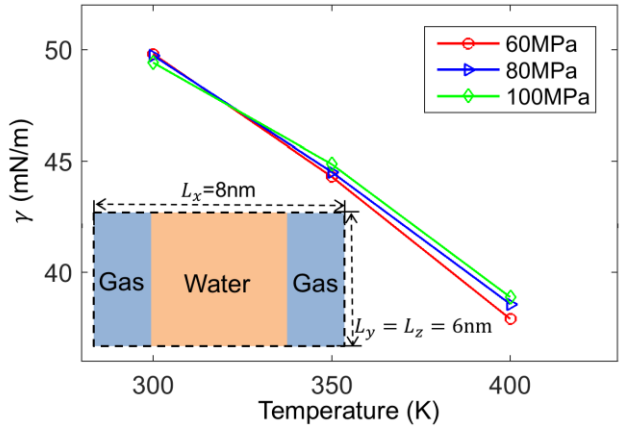

Figure 3-5. *Water-methane interfacial surface tension.* The inset is a schematic of the system used to compute the interfacial tension of planar water-methane interfaces.

Figure 3-5 shows that the water-methane interfacial surface tension decreases with temperature and varies little with pressure. These trends as well as the range of interfacial surface tension are consistent with earlier simulations.[295] Using the interfacial tension in Fig. 3-5, the prediction of the gas breakthrough pressure by the classical capillary theory is computed as $P_c^0 = 2\gamma/W$ and shown in Fig. 3-4. We observe that the gas breakthrough pressure is systematically underestimated using this method. In this method, however, the residual water film, which effectively narrows the pore, is neglected. To consider this effect, we compute a corrected capillary pressure $P_c^1 = \gamma/(W/2 - h)$ (h is the thickness of the residual film), and the predicted gas breakthrough pressure is shown with solid line in Figure 3-5. The corrected capillary pressure can predict the gas breakthrough pressure in the 4nm- and 6nm-wide pores reasonably well, but still underestimates the gas breakthrough pressure in the 2nm-wide pores by ~20MPa. The significant underestimation of the gas breakthrough pressure by the corrected capillary pressure is next examined from several perspectives.

It is possible that the pore entrance can contribute an extra energy barrier for gas invasion into the nanopores. Since this possible entrance effect is not taken into account in the classical capillary theory, it can cause the underestimation of gas breakthrough pressure by the capillary theory. However, this effect is ruled out through additional simulations. In these simulations, we start from a configuration in which the gas has already invaded into the 2nm-wide nanopores by half the pore length under high pressure (e.g. the pressure marked by the two red squares in Fig. 3-5). We then lower the pressure difference ΔP_{ud} between the two pistons to the highest pressure difference at which gas breakthrough was not observed in the simulations described in Section 3.3.2 (e.g. the pressure marked by the rightmost blue star in Fig. 3-5). It is found that, within 30-40ns, the gas front always recedes back into the upstream reservoir. This thus rules out the existence of an extra barrier when the gas break into a pore initially filled by liquids.

It is possible that the interfacial tension of the water-gas interfaces inside the nanopore differs from that at planar water-gas interfaces because of their small radius. However, prior work showed that interfacial tension decreases as the radius of the interfaces approaches molecular dimension,[296] which should lead to the overestimation of the breakthrough pressure when the interfacial tension measured for planar water-gas interfaces is used.

In addition to the capillary pressure, the disjoining pressure of the water film inside the pore may pose an additional barrier for gas invasion. Indeed, recent simulations revealed that disjoining pressure is responsible for the anomalous infiltration pressure observed in some carbon nanotubes. [297] Since the mica surface is not charged, two types of disjoining pressure, i.e. the van der Waals disjoining pressure and the structural disjoining pressure, can be considered. The van der Waals disjoining pressure is given by

$$\Pi_{vdw} = -\frac{A_m}{6\pi W^3}, \qquad (3.2)$$

where A_m is the Hamaker constant. Taking A_m as 2.0×10^{-20}J from theoretical prediction[298] or 2.2×10^{-20}J from experimental measurement[298], the magnitude of the van der Waals disjoining

pressure in a 2nm-wide pore is ~0.13MPa, too small to explain the observed discrepancy observed above. The structural disjoining pressure for a hard sphere liquid confined between two planar walls is given by [297-298]

$$\Pi_{stru} = -\rho_{\infty} k_B T \cos\left(\frac{2\pi W}{\sigma}\right) e^{-\frac{W}{\sigma}}, \quad (3.3)$$

where ρ_{∞} is the bulk density of the liquids, k_B is the Boltzmann constant, and σ is the diameter of fluid molecules. Taking the diameter of water molecule as 0.3nm, the magnitude of the structural disjoining pressure in 2nm-wide pores is thus ~0.11MPa, again too small to explain the observed discrepancy observed above.

The structural disjoining pressure in Equ. 3.3 however, does not take into account the fact that the mica surface is hydrated by interfacial water molecules that bond strongly to them. When two mica surfaces approach each other closely, the hydration structure near individual mica surfaces can be perturbed, and the resulting hydration force can generate an additional structural disjoining pressure.[298]

To evaluate whether surface hydration can lead to the underestimation of the gas breakthrough pressure, we examine the hydration of the mica surfaces in both 2nm-wide and 4nm-wide pores. Figure 3-6a compares the water density profile as a function of distance from the mica wall in both pores. We observe that the water density profile shows oscillation only close to the mica surface and becomes uniform beyond ~0.5nm from the mica surface. Importantly, the density profile of intefacial water is pratically identical in both pores. Because water is a dipolar molecule and its intefacial structure is also characterized by its orientation, we further assess the orientation of the interfacial water in the 2nm- and 4nm-wide pores. As shown in Fig. 3-6b, we consider water molecules in two regions (region 1: $W/2 - 0.3\text{nm} < z < W/2$, W is the pore width; region 2: $-0.2\text{nm} < z < 0.5\text{nm}$) and compute the distribution of the water molecules' dipole with respect to the normal direction of the mica surface. Figure 3-6c shows that the water molecules in Region 1 are nearly randomly oriented. Water molecules in Region 2 tend to orient their dipole toward the mica surface.

Importantly, in each region, the orientation of water molecules is nearly identical in the 2nm- and 4nm-wide pores. The fact that the density profile and the dipole orientation distribution of interfacial water in both pores are nearly identical suggests that the purtubration of the water structure near mica surface as the pore width decreases from 4 to 2nm is very small. Thereore, the hydration force and related disjoining pressure is unlikely to be significant. This is also consistent with previous experimental studies which showed that the hydration force between mica surface separated by water decays to nearly zero at a separation about 2nm.[299] Therefore, the hydration forces cannot cause the overestimation of the gas breakhrough pressure observed in Fig. 3-5.

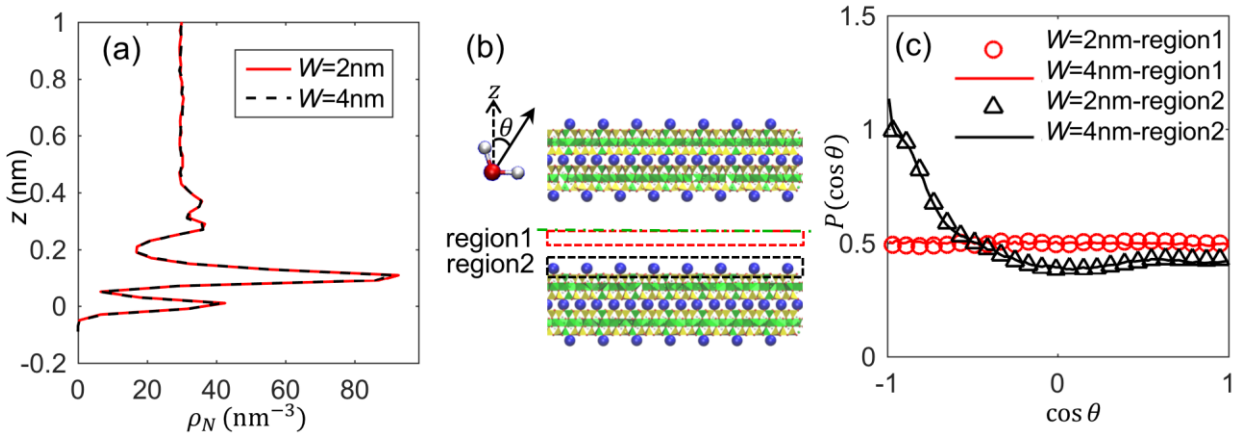

Figure 3-6. *Density distribution and orientation of water molecules near mica-water interfaces in 2nm and 4nm-wide pores filled with water.* **(a)** The water number density profiles along z-direction in the two pores. **(b)** A schematic showing the definition of region 1 (the red dashed box located at $W/2-0.3\text{nm}<z<W/2$, W is the pore width) and region 2 (the black dashed box located at –0.2nm<z<0.5nm) in the mica pores. The dipole orientation of water molecules with respect to the normal direction of the nearest mica wall is calculated in these two regions. **(c)** The dipole orientation distribution of water in regions 1 and 2 (see panel b) for the 2 and 4nm-wide pores. A random distribution corresponds to $P(cos\theta) = 0.5$.

None of the above physics can explain the underestimation of the gas breakthrough pressure using the classical capillary pressure, even after the pore width is corrected by considering the finite thickness (diffuseness) of the residual liquid film. Here we suggest that the discrepancy can originate from the ambiguity in precisely defining the width of a pore when it approaches molecular dimensions. Specifically, due to thermal fluctuation, the liquid surface is diffuse and exhibits a finite thickness. Under the action of capillary forces, the thickness of a liquid-gas

interface is $\sim\sqrt{k_BT/\gamma}$.[300] With such a diffuseness of the liquid-gas interface, a thickness of $h - 0.5\sqrt{k_BT/\gamma}$ to $h + 0.5\sqrt{k_BT/\gamma}$ may be designated to a liquid film with a thickness of h computed using Equ. 3.1. For a pore with a width of W and a residual liquid film with a thickness of h, the lower and upper limits of the effective pore width can be estimated reasonably by

$$W_{eff} = W - 2(h \pm \frac{1}{2}\sqrt{k_BT/\gamma}). \quad (3.4)$$

Using the new effective pore width to compute the capillary pressure, the range of reasonable breakthrough pressure for a given pore can be computed. The shaded area in Fig. 3-4 shows the range of possible gas breakthrough pressure when the range of film thickness to assign is estimated using Equ. 3.4. For all pores considered here, the gas breakthrough pressure observed in the MD simulations is within the shaded area shown in Fig. 3-4. Therefore, the diffuseness of the gas-water interface can potentially explain why the gas breakthrough pressure is underestimated significantly in the 2nm-wide pores.

3.3.3 Dynamics of gas invasion into liquid-filled pores

After gas breaks into a pore, the subsequent two-phase flow proceeds as a liquid meniscus moving deeper into the pore. Here we quantify the movement of the liquid meniscus by computing the position of its front (i.e. point *O* in Fig. 3-7a) and examine to what extent it can be described by the classical hydrodynamics. The forced invasion of gas into a liquid-filled pore can be predicted using the approach for deriving the Lucas-Washburn equation as in the case of the spontaneous imbibition of fluids into pores. Specifically, we make three assumptions: (1) inertia effects are negligible, (2) the gas breakthrough pressure can be computed using $P_B = P_C^1 = \gamma/(W - 2h)$, (3) the dynamics of gas invasion into a pore is dominated by the transport of liquids in the liquid-filled portion of the pore, and the latter can be treated as a simple Poiseuille flow with a slip length of b on the pore walls. In the third assumption, the complex two-phase flow near the gas invasion front is neglected, which is reasonable only if the total thickness of the residual liquid films on the pore wall is much smaller than the pore width. With these assumptions, one can show

that, in a pore that is initially filled entirely by liquids, the movement of the front of the liquid meniscus observes

$$(L-x)^2 = L^2 - 2At, \qquad (3.5)$$

where L is the length of the pore, x is the position of the liquid meniscus front inside the pore, gas begins to invade into the pore at t=0 and A is a constant given by

$$A = \frac{W^2(W+6b)}{12\eta(W-2h)}(\Delta P_{ud} - P_B), \qquad (3.6)$$

where ΔP_{ud} is the pressure drop between the two liquid reservoirs.

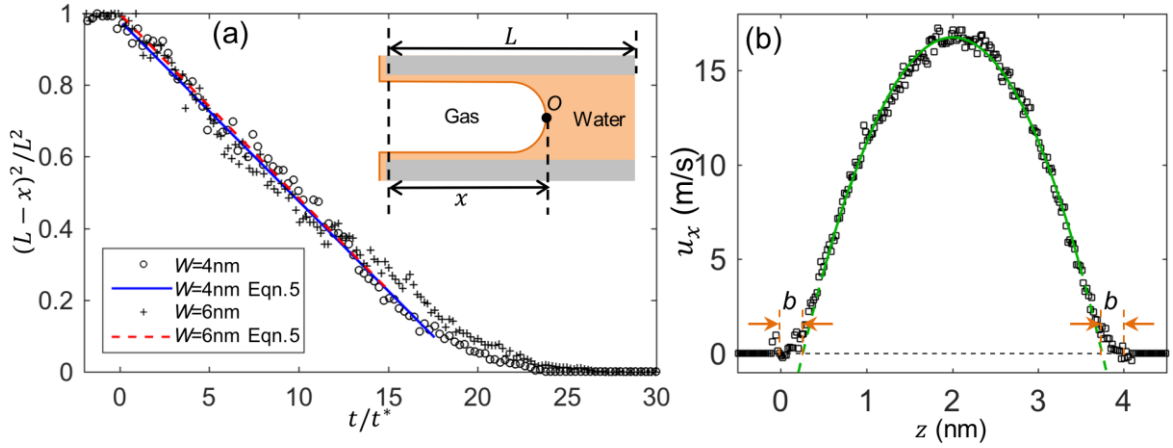

Figure 3-7. *Dynamics of gas invasion into mica pores*. **(a)** The location the liquid meniscus in the pore (x) as a function of time (t=0 is defined as the instant that gas starts to invade into the pore) for W=4 and 6nm pores. The meniscus position x is shown as $(L-x)^2$ and normalized by L^2, where L is the pore length. The time is normalized by $t^* = L/\sqrt{\Delta P_{ud}/\rho}$, where ΔP_{ud} is the pressure difference between the two liquid reservoirs up- and down-stream the pore and ρ is the bulk water density at 400K. The data points are linear fitted base on Equ. 3.5. The inset shows a schematic of gas invading into a nanopore. **(b)** The x-velocity of water flow across a 4nm-wide pore driven by a constant acceleration. The velocity profile in the central portion of the pore is fitted to a quadratic curve and extrapolated to the wall to obtain the slip length b.

The predictions of Equ. 3.5 and 3.6 can be checked using MD simulation data. Because the total residual water film thickness on pore walls is ~35% of the width of the 2nm-wide pore, the third assumption underlying these equations is invalid in these pores. Therefore, we only examine the validity of Equ. 3.5 and 3. 6 in the 4nm- and 6nm-wide pores. The position of the liquid meniscus front is determined as follows. We compute the water density along the pore center at each time $\rho_{cl}(x)$, and scan from the pore entrance to the pore exit. The position at which the water

density $\rho_{cl}(x)$ reaches bulk water density (31.3nm^{-3}) is considered as the front of the liquid meniscus. Figure 3-7a shows the dynamics of the meniscus front for a pressure difference $\Delta P = 20\text{MPa}$ in the 4nm- and 6nm-wide pores. We observe that, except at the final stage of gas invasion process, the square of the length of the liquid-filled pore, $(L-x)^2$, decreases linearly with time, in agreement with the prediction by Equ. 3.5 and 3.6. Linear fitting of the data in Fig. 3-7a shows that the constant A in Equ. 3.5 is 77.6×10^{-9} and $53.2\times10^{-9}\text{m}^2/\text{s}$ in the 4nm- and 6nm-wide pores, respectively. The deviation from the linear scaling of $(L-x)^2$ with respect to time *t* during the final stage of gas invasion is caused by the fact that, at this stage, the liquid-filled portion of the pore is short and thus the hydrodynamic resistance for flow from the pore exit to the reservoir can no longer be neglected (a similar effect is observed during the initial stage of liquid being imbibed into gas-filled pores).[108, 301]

To check if the pre-factor A can be computed accurately by Equ. 3.6, we determine the two parameters in this equation (viscosity η and slip length b) through separate simulations. Specifically, we build a 4nm-wide pore that is periodic in its length direction (i.e. no reservoirs at its two ends) and has identical mica walls with those in the gas invasion simulations. The pore is filled with water to the density found in the liquid-filled portion of 4nm-wide pores. To measure η and b, a constant acceleration is applied on each water molecule to generate a steady flow. The velocity profile of the resulting flow across the pore is shown in Fig. 3-7b and a parabolic velocity profile, as expected from classical hydrodynamics, is observed in the central portion of the pore. Fitting the velocity profile in the central portion of the pore, the viscosity η is calculated as 0.22mPa·s, which is close to the reported value of bulk water at the same temperature.[302] Extrapolating the parabolic velocity profile to the pore wall (see Fig. 3-7b), a negative slip length of b=0.256nm is obtained. Such a negative slip length is consistent with the fact that water molecules are attracted strongly to the pore walls.[303] Using the η and b computed here, as well as the residual film thickness determined in *Section 3.3.1*, the pre-factor A given by Equ. 3.6 is computed to be 73.4×10^{-9} and $56.5\times10^{-9}\text{m}^2/\text{s}$ for 4nm- and 6nm-wide pores, respectively.

Their good agreement with these extracted directly from Fig. 3-7b suggests that the classical hydrodynamic theories can be used to predict the invasion of gas into nanopores accurately down to a pore width of 4nm.

3.4 Conclusions

In summary, we study the invasion of methane gas into mica nanopores initially filled with water using MD simulations. Driven by sufficiently high pressure, the methane gas can invade into the mica pore and move downstream. However, a residual film is left behind the moving liquid meniscus. The thickness of this film is less than one nanometer in the pores studied here (2nm-, 4nm- and 6nm-wide) and decreases as the pore width decreases. The critical pressure for gas invasion, i.e. the gas breakthrough pressure, for the 4nm- and 6nm-wide pores can be predicted using the capillary pressure, providing that the curvature of the liquid meniscus is corrected using the finite thickness of the residual film on the mica walls. For the 2nm-wide pores, the capillary pressure corrected by the film thickness still underestimates the gas breakthrough pressure. This underestimation is unlikely to be caused by van der Waals and structural disjoining pressure as well as the hydration interactions, but can be rationalized by taking into account the diffuseness of the gas-liquid interface. The dynamics of gas invasion, as quantified using the movement of the front of the liquid meniscus, can be predicted by the classical hydrodynamics if the negative slip length on the mica surface, which originates from the strong affinity of water to the hydrophilic mica surface, is taken into account. These results suggest that the gas invasion into liquid-filled nanopores can be described by continuum theories as pores are as narrow as 2nm providing that crucial *interfacial effects* such as the existence and finite thickness of the residual liquid film, diffuseness of the gas-liquid interfaces, and the negative slip length at solid-liquid interfaces are taken into account.

Gas invasion in practical engineering systems, e.g. porous media saturated with water, is much more complicated than the ideal situation considered here. For example, there often exist

heterogeneity in surface properties (e.g. hydrophobic vs. hydrophilic), pore size, and pore shape along the path of gas invasion. However, delineating the essential features of the gas invasion in the model systems adopted here and clarifying the validity of continuum theories in describing the thermodynamics (e.g. the gas breakthrough pressure) and dynamics (e.g. the movement of liquid meniscus) of the gas invasion process is a key step toward obtaining a fundamental understanding of the gas invasion in more practical situations.

Supporting Information

All supporting information cited in this chapter is located in *Appendix B*.

Chapter 4. Thermodynamics of Droplet Invasion into Nanopores

Disclosure

This work has been published by the American Chemical Society: C. Fang, Q. Kang, R. Qiao, The Role of Disjoining Pressure and Thermal Activation in the Invasion of Droplets into Nanopores. *J. Phys. Chem. C* 2019, 123 (11), 6905-6912.

4.1 Introduction

Multiphase transport at nanoscale is widely encountered in engineering practice, e.g. in the drying of natural and engineering nanoporous materials,[304-305] gas and oil recovery,[194-195] and oil-water separation.[306-307] In such transport, the solid boundaries are often preferentially wetted by one fluid phase and another fluid phase is dispersed as bubbles or droplets. A frequently encountered scenario is the presence of an immiscible phase as a droplet/bubble near the entrance of a nanopore. Understanding how the droplet or bubble enters the nanopore is crucial because whether it can translocate the nanopore or become trapped at the entrance can greatly affect the operation and performance of practical systems. Knowledge of such transport is also necessary input for simulations such as the pore-network modeling of multiphase flows in porous media.

Prior studies of the transport of droplets through narrow pores showed that the wetting property of the droplet phase on the pore surface, the size and shape of the droplet and pore, and the external pressure difference play important roles in determining the droplet transport behavior.[134, 196-201] For example, in absence of a pressure difference between the up- and downstream of the pore, the free energy landscape for droplet transport has been investigated theoretically. If the droplet size is below a threshold value, which is comparable to the size of the pore, a nonwetting droplet can enter the pore spontaneously. This prediction has been verified in the adsorption of transition liquid metal droplets into carbon nanotubes, where various droplet transport regimes were identified.[196-197] More droplet transport regimes were also identified when the spreading of droplet on the exposed solid surface outside the pore was taken into account.[198] If the droplet size is considerably

larger than the width of a pore, an external pressure difference is required to drive the droplet into the pore. The threshold invasion pressure can be estimated using the Laplace pressure difference between the front and rear sides of the droplet as it enters the pore.[201] When strong flow is involved during the invasion of a droplet into a pore, the ensuing change of the curvature at the droplet's leading edge has also been shown to affect the droplet transport greatly.[199]

While prior works advanced the basic understanding of droplet transport into pores, new issues arise when the pores reach nanoscale dimensions. First, the application of the insights from prior studies involves uncertainties. When a non-wetting droplet enters a nanopore, a molecularly thin film can form between the droplet and the surface of the nanopore and a host of interfacial forces can emerge. To what extent these forces affect the free energy landscape of droplet transport into the nanopore is not clear *a priori.* For example, while droplets smaller than the nanopore size were expected to enter the nanopore freely in most previous studies, it is not clear if this is universally true for nanopores with various surface properties. Second, when an external pressure difference exists between the up- and downstream of the nanopore, much of the prior work focused on identifying the threshold pressure difference under which a droplet can deterministically enter the nanopore. However, when the size of the droplets and pores reaches nanoscale, where thermal fluctuations are significant, a droplet can potentially enter and translocate the nanopore by overcoming the energy barrier through thermal activation. Therefore, classifying the free energy landscape for droplet transport through nanopores in presence of a pressure difference, which has received limited attention in prior works, becomes important.

Here, we are interested in how a droplet invades a nanopore whose surface is fully wetted by water. Our interest in this system is motivated by its relevance to gas/oil extraction from shales, where much of the gas/oil exists in pores with nanoscale dimensions and the surfaces of many pores are strongly hydrophilic.[95, 191, 308] Much of the existing work on gas/oil transport in shales focuses on single phase transport. However, multiphase transport does occur during gas/oil

recovery because water is found ubiquitously in shale formation and they can greatly affect the transport of gas/oil.[179] While studying multiphase transport in nanopores experimentally is difficult, this problem is amenable to molecular dynamics (MD) simulations. In MD simulations, the nanopore and all fluids are resolved at the molecular level and the transport can be modeled with much less restrictive assumptions compared to continuum models. Indeed, MD simulations have emerged as a powerful tool for understanding nanoscale multiphase transport in recent years.[188, 195]

In this study, we examine the free energy profile of a droplet as it enters the nanopore and how this profile is affected by the applied pressure difference and the size of the droplet and nanopore. We show that, for nanopores whose surface is completely wetted by water but not by the droplet, a droplet larger than the pore diameter must overcome a higher free energy cost than that predicted by classical theories due to large disjoining pressure. When the droplet is smaller than the pore size, and thus the droplet is usually expected to enter the pore freely, a large energy barrier for droplet entrance can nevertheless exist. The insight gained here helps understanding the nonlinear multiphase transport phenomena in nanoporous media and inform the development of better pore network models.

4.2 Models and Methods

We use continuum and molecular dynamics (MD) models to determine the free energy profile for the invasion of droplets into nanopores. In the continuum model, we consider two-dimensional (2D) droplets invading a slit pore and three-dimensional (3D) spherical droplets invading a cylinder pore. The 2D cases are studied to facilitate the assessment of the accuracy of continuum models by MD models because studying large droplets in 3D using MD simulations is much more expensive than in 2D. As we shall see, results in 2D and 3D spaces are qualitatively similar.

Continuum model. We first examine the invasion of a droplet into a long pore in 2D space. A droplet with an initial diameter D_0 is immersed in water and positioned at the entrance of a pore

with a width W. Figure 4-1a shows the sketch of such droplet entering the pore. A pressure difference ΔP is imposed between the upstream reservoir and downstream pore. We focus on the situation where the pore wall is completely wetted by water and the droplet diameter is larger than the pore width. Hence, as the droplet enters the pore, a thin residual water film remains on the pore wall, which reduces the pore to an effective width W_{eff}. We note that such thin water films, akin to the precursor film in front of a droplet spreading on a hydrophilic surface,[309] are observed both in prior studies of bubbles/droplets entering pores with strongly hydrophilic walls (e.g. mica)[310-312] and our MD simulations (see below).

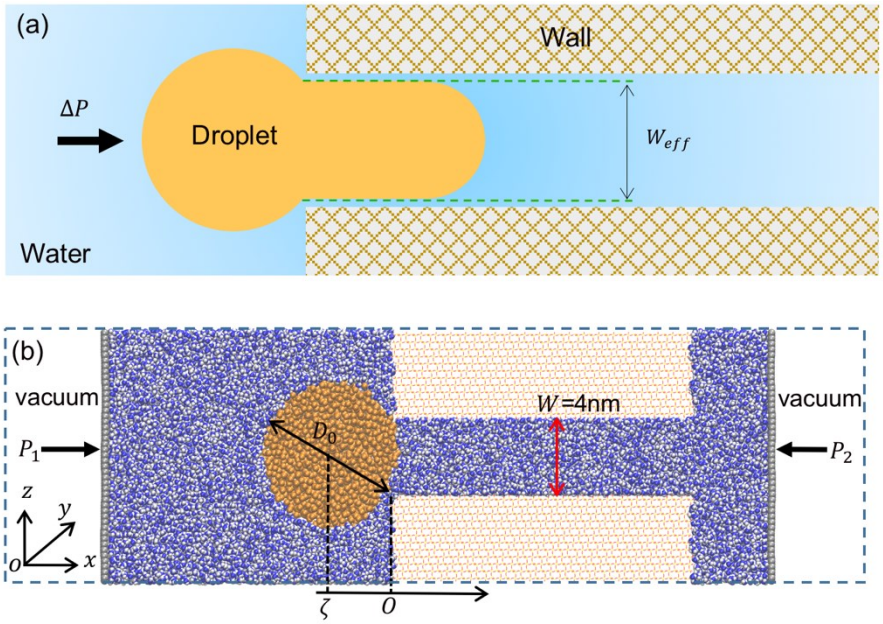

Figure 4-1. *Continuum and molecular models of droplet invasion into a slit pore*. **(a)** A schematic of the model for the invasion of a droplet into a pore. The dashed lines denote the boundary of the thin liquid film between the droplet and water after invasion. (**b**) A snapshot of a representative MD model. An un-deformed droplet (diameter: D_0) is initially positioned at the entrance of a slit pore (nominal width: 4nm). The pressure up- and down-stream the pore is set to P_1 and P_2 by the two pistons. The system is periodic in all three directions but two large vacuum spaces are placed outside of the two pistons. Water molecules are shown as blue (oxygen) and white (hydrogen) spheres. The droplet (piston) atoms are shown as orange (grey) spheres. The pore walls made of quartz are shown as lines. The dashed box denotes the simulation box.

Following the standard approach,[195-198, 200, 313] we determine the free energy profile as the droplet moves into the pore by considering only the surface energy and pressure work. For an

infinitesimal displacement of the droplet into the pore, the associated free energy variation dG is thus

$$dG = \gamma dA - \Delta P dV_{in}, \quad (4.1)$$

where γ is the water-droplet interfacial tension, dA and dV_{in} are the changes of the area of water-droplet interface and the volume of the droplet inside the pore with the displacement of the droplet into the pore, respectively. To obtain the free energy profile, three widely used approximations are made: the droplet is pinned at the pore mouth before fully entering the pore; with the exception of the interface between the droplet and the residual water film, other water-droplet interfaces are circular; the droplet is incompressible.[196-198, 200] The details for evaluating the free energy profile are provided in Fig. SC-1 and the associated text in the *Appendix C*. After studying the droplet invasion in 2D, the calculations are repeated in 3D space.

MD models and methods. Figure 4-1b shows a snapshot of a representative MD system. The system consists of two water reservoirs, a slit channel bounded by two solid walls, a droplet immiscible with water and two rigid pistons. The pressure in the up- and downstream reservoirs is maintained by applying appropriate forces on the two pistons bounding them. The system is periodic in all three directions but two large vacuum spaces are placed outside of the pistons to effectively remove the periodicity in the pore length direction. The droplets are cylindrical in shape because they span the periodic MD box in the *y*-direction. Droplets with diameters of 1.86, 2.26, 2.60, and 6.00nm have been studied. The full dimensions of the pore and the vacuum space are varied for different droplets and are summarized in Table SC1 in the *Appendix C*. With the droplet and simulation box sizes listed in Table S1, finite-size effects on the free energy profile for droplet invasion should be minor in our simulations (see Fig. SC-2 in the *Appendix C* and related discussion). The pressure applied on the right piston is fixed at 1bar, while that on the left piston is varied in different simulations to generate different pressure differences up- and down-stream the slit pore.

Water is described using the SPC/E model.[314] The droplet are made of Lennard-Jones (LJ) particles with LJ parameters same as those for methane molecules[264] except that the ϵ for droplet-droplet interactions is set to 4.0kJ/mol in our simulation so that the droplet behaves like liquids. The LJ parameters for the interactions between the droplet atoms and all other types of atoms in the system are obtained using the Lorentz-Berthelot combination rule. The channel wall is made of α-quartz cleaved from the (101) direction, with a silanol group surface density of 5.92 per nm^2. The force fields parameters including Lennard-Jones potential and partial charges of quartz are taken from the CLAYFF force fields.[265, 315] The cleavage of the quartz surface follows recent work by other researcher.[315] Following their convention, the zero plane of the quartz surface is defined as the location of the second outmost layer of the silicate atoms. The nominal channel width W is the distance between the zero planes of the two walls (see Fig. 4-1b). The quartz surface used here is strongly hydrophilic as demonstrated by separate simulation in which a water droplet initially placed above it ultimately spread completely to form a thin film (see Fig. SC-3 in the *Appendix C*). To reduce computational cost, all the silicate and oxygen atoms of the wall are fixed and their interaction with each other is excluded. The hydrogen atoms of surface silanol groups are allowed to vibrate by considering the bonds and angle of the silanol groups.

MD simulations are performed using the 5.1.4 version of Gromacs package.[316] The bonds and angle of water are constrained by SETTLE algorithm. An NVT ensemble with the velocity-rescale thermostat and a time constant of 1ps at 300K is adopted.[289] A global cutoff 1.2nm is used for computing the LJ potential and the particle mesh Ewald (PME) method is used to calculate the electrostatic interactions.[317]

The free energy profile for droplet invasion into the slit pore is computed using the Umbrella sampling technique.[318] The idea is to sample the free energy in different windows centered along the reaction coordinate of droplet invasion, which is taken as the center-of-mass position of the droplet. To generate initial configurations corresponding to droplets residing in different windows,

we first apply a force to each atom of the droplet so that it moves at a speed of ~1 nm/ns from the left reservoir into the pore's interior. Configurations recorded during this non-equilibrium run are then used as the initial configurations of the Umbrella sampling runs. A window size of 0.15 and 0.20nm is used for the small and large droplets, respectively. Next, equilibrium Umbrella sampling runs are performed so that the position of the droplet in the *x*-direction in each window is sampled for 20-30ns. In these simulations, a force is applied on each atom of the droplet to constraint the droplet's center-of-mass around the center of each sampling window. This force is given by $F_{com} = K(x_{com} - \zeta)^2$, where x_{com} and ζ are the droplet's center-of-mass and the center of the sampling window in the *x*-direction, respectively. K is a spring constant taken as 1000kJ/mol·nm^2. From the histograms of the center-of-mass of the droplet in each sampling window (see Fig. SC-4 in the *Appendix C*), the potential of mean force (PMF) of the droplet is computed using the Weighted Histogram Analysis Method and the error bar is estimated using the bootstrap analysis with 100 bootstraps.[319]

For comparing the free energy profile of droplet invasion obtained from continuum and MD models, the interfacial tension between the water and droplet phase is needed. This interfacial tension is calculated from a separate simulation. In this simulation, a slab of LJ particles with LJ parameters identical to the droplet is sandwiched between two slabs of water and the periodic MD box has a cross-section area of 4×4nm^2 and a thickness of 8nm in direction normal to the LJ particle-water interface (the *x*-direction). An equilibrium NVT simulation is performed at 300K for 8ns. The interfacial tension is evaluated using $\gamma = 1/2 \int_0^{L_x} [P_{xx} - 0.5(P_{yy} + P_{zz})]\, dx$,[320] where L_x is box length in the *x*-direction, and P_{xx}, P_{yy}, and P_{zz} are the three diagonal components of the pressure tensor along the *x*-, *y*-, and *z*- directions. The interfacial tension is determined as 94.84 ± 4.94mN/m.

4.3 Results and Discussions

4.3.1 Continuum models

Figure 4-2a shows the evolution of the free energy ΔG, as a function of the droplet volume ΔV_{in} invading into the pore for the case of $D_0 = 3W_{eff}$ at several pressure difference ΔP. For generality, ΔG, ΔV_{in}, and ΔP are normalized using $G_0 = \pi\gamma D_0$, $V_0 = \pi D_0^2/4$ and $P_c = 2\gamma/W_{eff}$, respectively. For large ΔP (e.g. $\Delta P = 0.3P_c$), the free energy decreases monotonically as ΔV_{in} increases, and the droplet can invade the pore spontaneously. For low ΔP, the free energy profile exhibits two local extremums, which lead to an initial free energy valley (depth: ϕ_1) and a subsequent energy barrier (height: ϕ_2, see Fig. 4-2b). Therefore, a droplet tends to be trapped near the pore mouth. Because whether the droplet can enter the pore is governed by the energy barrier height ϕ_2, we extend the above calculations to different droplet sizes and pressure differences to compute a map of this barrier height. Figure 4-2c shows that, for given droplet size and pore width, a spontaneous invasion pressure ΔP_{si} exists: for $\Delta P \geq \Delta P_{si}$, a droplet experiences no barrier as it invades the pore; for $\Delta P < \Delta P_{si}$, a droplet must overcome a barrier to invade the pore, and this barrier increases as ΔP becomes smaller. As the size of the droplet relative to the pore increases (i.e. as D_0/W_{eff} increases), ΔP_{si} approaches the capillary pressure P_c and the barrier height for droplet invasion increases for a fixed ΔP. In addition to D_0/W_{eff}, the barrier height tends to be higher for larger droplets and larger surface tension (note that ϕ_2 is scaled by $G_0 = \pi D_0\gamma$ in Fig. 4-2c).

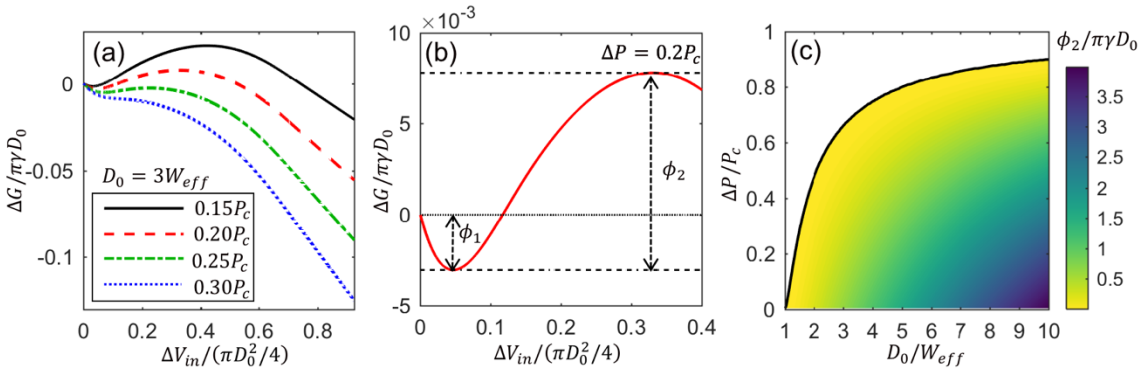

Figure 4-2. *Continuum model of droplet invasion into a slit pore*. **(a)** The free energy profiles of an invading droplet as a function of its volume inside the pore under three pressure differences along the pore. The diameter of the un-deformed droplet, D_0, is $3W_{eff}$. **(b)** A zoom-in view of the free energy profile for $\Delta P = 0.2P_c$ in (b). **(c)** Dependence of the entry barrier height ϕ_2 on the droplet size and applied pressure. The solid line corresponds to $\phi_2 = 0$.

The above analysis can be extended to three dimensions (see *Appendix C*), in which a spherical droplet invades a cylindrical pore, a situation often encountered in nanofluidic systems. To appreciate the absolute magnitude of the free energy landscape, the analysis is done under conditions typical of oil recovery operations, i.e. the temperature is 373K and the interfacial tension γ between droplet and water is 35mN/m.[321] The key features of the free energy landscape for the droplet invasion here are similar to those revealed in Fig. 4-2. For example, Fig. 4-3a shows the map of the barrier height ϕ_2 when a 6nm diameter droplet enters pores with different sizes (note that ϕ_2 is shown in the unit of thermal energy k_BT, where k_B is the Boltzmann constant and T is the temperature).

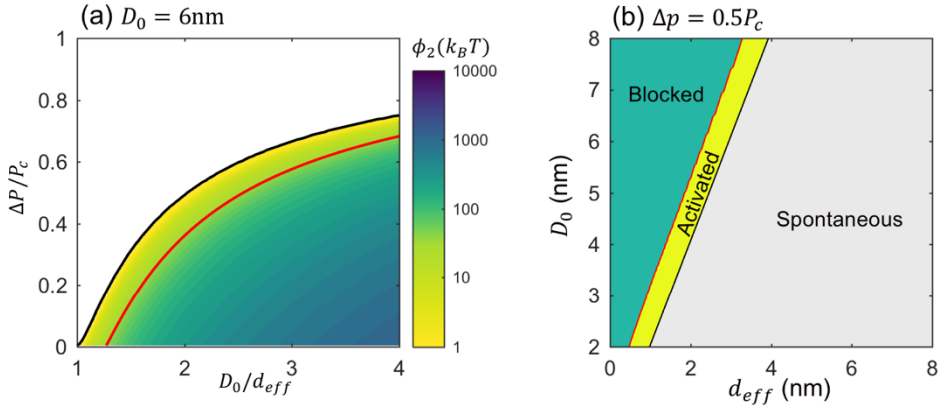

Figure 4-3. *Invasion of a cylindrical pore by spherical droplets*. (**a**) Dependence of the entry barrier height ϕ_2 on the droplet size and pressure difference along the pore. The blue and red lines correspond to ϕ_2=0 and $\phi_2 = 40k_BT$, respectively. (**b**) A map for the droplet invasion mode as function of the droplet and pore size. The pressure difference along the pore is fixed at $\Delta P = 0.5P_c$.

As in the 2D case, a spontaneous invasion pressure ΔP_{si} exists for each effective pore diameter D_{eff} and a barrier must be overcome at lower pressure differences. Although ϕ_2 can reach thousands of k_BT, because of the droplet's small size, ϕ_2 will not be prohibitively high if the pressure difference is not too much smaller than ΔP_{si}. For example, the red line in Fig. 4-3a corresponds to a barrier height of $40k_BT$. Because thermal activation time $\tau_a \sim t_0 \exp(G_B/k_BT)$ ($t_0 \sim h/k_BT$, h is the Planck's constant, and G_B is the barrier height), driven by thermal fluctuations, the droplet can overcome this barrier to enter the pore after a waiting time of ~8.3

hours at the pore entrance. Hence, although the nanometer-sized droplet cannot enter the pore when $\Delta P < \Delta P_{si}$ in the deterministic view, it can nevertheless invade the pore in a stochastic view when ΔP is not too low compared to ΔP_{si}, i.e. thermal activation lowers the threshold pressure for nanometer-sized droplets to invade nanopores. Equivalently, for a given pressure difference, thermal activation allows nanometer-sized droplet to invade pores smaller than that anticipated in the deterministic view. To show this, we computed the entry barrier height for a series of droplets and nanopores when the pressure difference is 50% of the capillary pressure. Without losing generality, we then assumed that a droplet can invade a pore by thermal activation if the entry barrier height is less than $40k_BT$ but is blocked otherwise. Figure 4-3b shows the map of the droplet invasion mode as a function of droplet and nanopore size. We observe that, because of thermal activation, the droplets considered here can invade pores ~0.5 nm (the width of the activated regime) narrower than that anticipated deterministically.

4.3.2 Molecular models

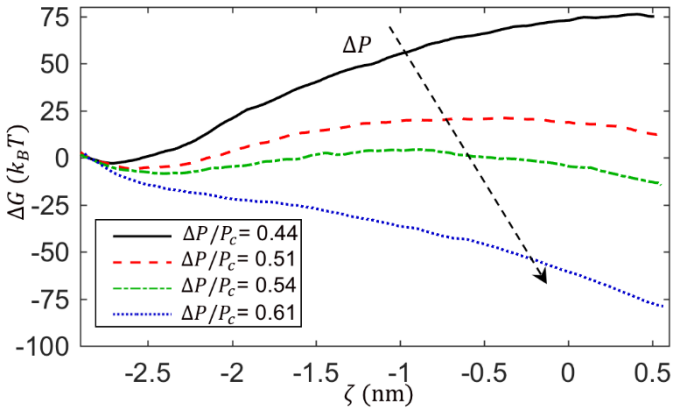

Figure 4-4. *Molecular model of nanodroplet invasion into a slit pore*. The free energy profiles of a 6nm-diameter droplet as a function of its center-of-mass position (ζ) at four different pressure differences from molecular model. The upper bound of the error bar of the free energy at any point along the pore is $1.44k_BT$.

Because the MD modeling of large spherical droplets is computationally expensive and droplet invasion in 2D and 3D space has similar features, we study the invasion of a slit pore by a nanodroplet that is periodic in the transverse direction (see Fig. 4-1b), which is similar to the

invasion of a 2D droplet into a slit pore studied in the previous section. Figure 4-4 shows the free energy profile of the droplet invasion under four pressure ratios. The free energy is taken as zero at the position where the droplet just touches the wall edges. The pressure differences are again scaled using the capillary pressure of the pore $P_c = 2\gamma/W_{eff}$ (the value of W_{eff} is given below). The free energy profiles are qualitatively similar to these predicted by the continuum model. For instance, at ΔP=$0.44P_c$, a significant entry barrier corresponding to a blockage of the droplet by the pore is observed. As the pressure difference rises to $0.61P_c$, the free energy decreases monotonically as the droplet invades the pore, suggesting that the droplet invasion is spontaneous. For intermediate pressure differences, an initial trap and a subsequent barrier as observed, just as in Fig. 4-2b.

To compare the MD predictions with these by continuum models, we first obtain the effective width of the slit pore. Figure 4-5a shows a snapshot of the droplet invading partially into the pore. Because of the strong hydrophilicity of the quartz wall, a thin water film is observed between the droplet and each pore wall. This effective width of the pore is evaluated from the number density profile of the water and droplet phase across the channel, which is calculated in the region between the two dashed lines in Fig. 4-5a. As shown in Fig. 4-5b, water accumulates near the solid wall and the density of the droplet phase is nearly constant in the middle part of the pore. Following the concept of Gibbs' dividing surface, the effective pore width W_{eff} is found to be 2.93nm by dividing the total mass of the droplet phase across the channel (computed from the density profile in Fig. 4-5b) by the droplet phase's bulk density.

Figure 4-5c and 4-5d show the continuum and MD free energy profiles of the droplet invading the nanopore at a pressure difference of $0.51P_c$ and $0.61P_c$, respectively. The MD predictions are systematically higher than the continuum predictions, which suggests that the continuum model tends to underestimate threshold pressure for droplet invasion. We propose that the deviation of the continuum predictions from the MD predictions originates from the fact that the thin water films sandwiched between the droplet and the pore walls contribute to an additional energy term

neglected in the continuum model.

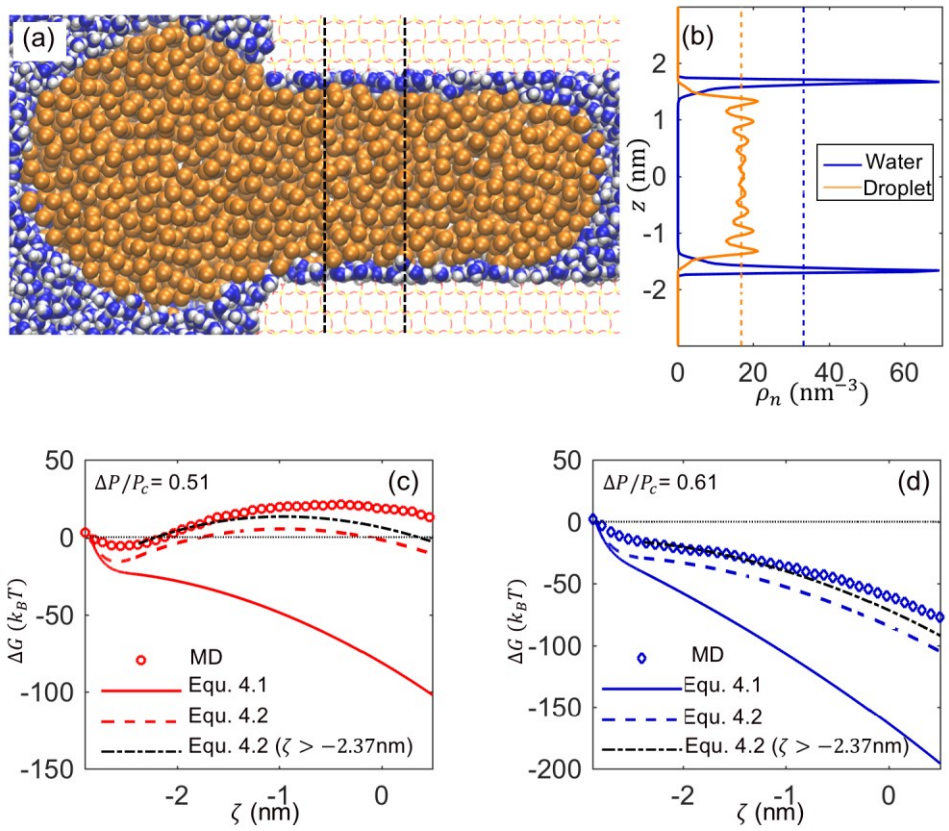

Figure 4-5. *Comparing the MD predictions with continuum models*. **(a)** A snapshot of the droplet invading partially into the slit pore in Fig. 4-1b. The color coding is same as that in Fig. 4-1b. **(b)** The number density profiles of water and droplet across the slit pore in the region bounded by two dashed lines in panel (a). The bulk water and droplet densities are shown as dashed lines. **(c, d)** The free energy profiles computed from continuum models and MD simulations at a pressure difference of $0.51P_c$ (c) and $0.61P_c$ (d). The upper bound of the error bar of the free energy from MD simulations at any point along the pore is $1.44k_BT$.

In the continuum model described above, the effect of water film is considered only through the surface energy of the water-droplet interfaces (see Equ. 4.1). Such an approach is acceptable if the water film is thick. Here, the water film is molecularly thin and inter-surface interactions contribute greatly to the system's energy, which is lumped as the disjoining pressure effects in the literature.[239, 297, 322-323] Therefore, as a droplet invades a pore, an extra term related to the disjoining pressure must be introduced into Equ. 4.1 to account for the energy required (gained) to form the thin water film:

$$dG = \gamma dA - \Delta P dV_{in} + E_d(\delta) dA', \quad (4.2)$$

where $E_d(\delta)$ is the energy per unit area of a water film with a thickness of δ and an area of A'. Assuming that the disjoining pressure is dominated by van der Waals forces, $E_d(\delta) = A_H/12\pi\delta^2$, where A_H is the Hamaker constant. The thickness of water film behind the semicircle-shaped front of the droplet is taken as 0.23nm, which is determined using water density profile shown in Fig. 4-5b and the concept of Gibbs dividing surface. Using a typical value of the Hamaker constant for water on strong hydrophilic substrates $A_H \sim 2.0 \times 10^{-20}$J,[239] the free energy profiles for droplet invasion are computed (see Fig. 4-5c and 4-5d). We observe that, when the disjoining pressure effects are considered, agreement between continuum and MD predictions is greatly improved. The remaining deviation is mostly caused by the fact that the energy variation during the initial phase of droplet invasion ($\zeta < -2.37$nm, when the front portion of droplet inside pore has not yet formed a semi-circle) is not captured well. Indeed, if Equ. 4.2 is used only in the region $\zeta > -2.37$nm and ΔG at $\zeta = -2.37$nm is set to the MD value, the agreement between continuum and MD predictions is very good (see Fig. 4-5c and 4-5d). The fact that the energy variation in the initial phase of droplet invasion is not captured well by the simple model used here is not surprising, e.g. the structure and energetics of the molecules in the water film near the sharp edge of pore entrance should differ from those in extended water films of same thickness but such effects are not considered. We note that apart from the disjoining pressure of the thin film, other physics including curvature effects and line tension can also be significant as the droplet dimension reaches nanometer scale.[324] They may contribute to the discrepancy between Equ. 4.1 and MD results and can potentially explain why the corrected continuum model using Equ. 4.2 still cannot fully capture MD results.

The greatly improved agreement between the continuum and MD predictions shown above highlights the potential importance of disjoining pressure in the invasion of droplets into nanopores. For the disjoining pressure effects to be prominent, its contribution, which depends on the droplet and pore size, should be at least comparable to the combined pressure and surface tension effects

considered in Equ. 4.1. As shown in the *Appendix C*, one can show that this amounts to requiring

$$\alpha = \left|1 - W_{eff}/2R_0 - \Delta P/P_c\right|^{-1} \; E_d(\delta_0)/\gamma \gtrsim O(1), \qquad (4.3)$$

where δ_0 is the thickness of the water film behind the front of the droplet inside the pore. When $\Delta P = \Delta P_{si}$, the pre-factor $\left|1 - W_{eff}/2R_0 - \Delta P/P_c\right|^{-1}$ approaches infinity. This is consistent with the idea that the effect of disjoining pressure on droplet invasion tends to be most significant at a ΔP where a droplet can spontaneously invade a pore in absence of such effects. For the system modeled here E_d/γ ~0.06, the pre-factors are 10 and 600 for $\Delta P/P_c$ =0.51 and 0.61, separately. Therefore, α =0.6 (36) when $\Delta P/P_c$ =0.51 (0.61), which is consistent with the importance of disjoining pressure effects revealed in Fig. 4-5c and 4-5d.

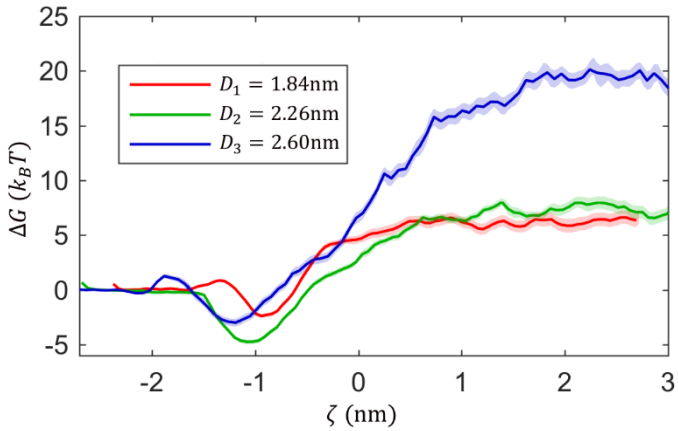

Figure 4-6. *Invasion of nanodroplets into pores wider than them.* Free energy profiles for the invasion of nanodroplets with diameters of 1.84, 2.26, and 2.60nm into a slit pore with a nominal width of 4.0nm. The pressure difference between the up- and downstream of the pore is zero. The shallow shaded areas represent the errors of free energy profile at each point.

We next examine the invasion of droplets into pores wider than them. Figure 4-6 shows the free energy profiles for the invasion of droplets with diameters of 1.84, 2.26, and 2.60nm into a pore with a nominal width of 4nm. No pressure difference is applied along the pore. Apart from a minor valley near the pore entrance, which is likely caused by the reduced hydrophilicity of the pore entrance's sharp edge, the free energy of the droplet inside the pore is 6-20k_BT above that in the bulk water. The latter suggests that, although it is often expected that a droplet can invade a pore wider than its diameter without any energy cost, for droplets invading pores only a few

nanometers wider than them, an energy cost is involved. The existence of this cost and its increase with the droplet size are consistent with the disjoining pressure effects presented above. Because a circular droplet invading a pore wider than it barely changes shape and hence the water-droplet interfacial area, no energy cost is expected. However, if the pore is only marginally wider than the droplet, the invasion of the droplet creates thin water films above and beneath it, which incurs disjoining pressure and related energy cost as presented in Equ. 4.2. Because the cost of creating these films increases as the films become thinner, the cost for a droplet invading the pore increases as the droplet size increases.

An interesting aspect of the invasion of droplets into wider pores is that the pressure drop between the up- and down-stream of the pore no longer occurs mostly across the droplet since the invading droplet no longer completely blocks the pore. Therefore, the invasion of a droplet into a pore relies on the hydrodynamic force exerted on it by the fluid flow and diffusion. Because the fluid velocity in nanofluidic system is generally small (~O(10^{-7}-10^{-3}m/s)), the hydrodynamic force is unlikely to be strong enough to overcome the thermodynamic force and drive the droplet into the pore. Here, we perform non-equilibrium simulations by imposing a pressure difference of 5MPa between the two reservoirs connected by the 4nm-wide pore (see Fig. 4-1b). A 1.84nm-diameter droplet is initially placed in front of the pore entrance, and both the flux of water through the pore and the position of the droplet are monitored. The droplet remains trapped near the pore entrance during the 20ns run (see Fig. SC-6 in the *Appendix C*). The mean water velocity through the pore is determined as 0.196 m/s by linear regression of the ensemble average of the cumulative number of water molecules leaving the upstream reservoir (Fig. SC-6's inset in the *Appendix C*). Using this mean velocity and the continuum prediction of the drag experienced by a 2D droplet confined in a slit channel,[325] the upper bound of hydrodynamic force exerted on the droplet is estimated to be ~33pN (see *Appendix C*). The fact that this force is smaller than the maximal thermodynamic force repelling the droplet from the pore (~55pN, determined from the free energy profile in Fig. 4-6) is consistent with the observation that the droplet does not invade into the pore.

In practical nanofluidic systems, the fluid velocity is generally less than ~10^{-3}m/s, and thus the hydrodynamic drag will be even weaker than that simulated here and thus the invasion driven by flow is more unlikely.

Although the droplets studied here are unlikely to invade the pore by fluid flow, invasion by thermal activation is possible. Using the free energy profiles shown in Fig. 4-6 and assuming that the droplet invasion into a pore is a Brownian translocation process through a domain characterized by a free energy profile ΔG, we can estimate the average time for a droplet near the pore entrance to enter the pore using[326]

$$\langle \tau \rangle = \frac{1}{D} \int_{\xi_s}^{\xi_e} exp(\Delta G(\xi)/k_B T) d\xi \int_{\xi_s}^{\xi} exp(-\Delta G(x)/k_B T)\, dx, \qquad (4.4)$$

where D is the droplet's diffusion coefficient. ξ_s is the left domain boundary, where ΔG first reaches zero if the droplet approaches from the pore interior to pore outside. ξ_e is the right domain boundary, where ΔG first reaches ϕ_2 if the droplet approaches from the pore interior from outside of the pore. The diffusion coefficients of the three droplets inside the slit pore are evaluated using separate simulations as 0.51×10^{-9}, 0.45×10^{-9}, and 0.37×10^{-9} m^2/s from the smallest to the largest droplet (see Fig. SC-8 in the *Appendix C*). The average entry times are estimated to be 9.81×10^{-7} s, 1.17×10^{-4} s, and 4.91s for the droplets with a diameter of 1.84, 2.23, and 2.60nm, respectively.

The invasion of spherical droplets into cylindrical pores can be understood using the free energy profiles computed for cylindrical droplets invading slit pores. Specifically, assuming that the disjoining pressure in a liquid film depends solely on its local thickness, the free energy profile for the invasion of a spherical droplet into a cylindrical pore $\Delta G_{3d}(\zeta)$ is related to that for the invasion of a cylindrical droplet with the same diameter and a length of L_y into a slit pore with width equal to circular pore diameter, $\Delta G(\zeta)$, by $\Delta G_{3d}(\zeta) = \pi \Delta G(\zeta) D_0 / 2L_y$, where D_0 is the droplet diameter (see *Appendix C*). Using this relation, the free energy profiles in Fig. 4-6, and Equ. 4.4, the average entry time for spherical droplets with diameters of 1.84, 2.26, and 2.60nm to

enter a 4nm-diameter cylindrical pore can be estimated as 1.80×10^{-7}s, 3.84×10^{-5}s, and 1.15×10^{1}s, respectively. These results and those for the 2D droplet show that for droplets entering pores slightly wider than them through Brownian diffusion, the entry time can increase sharply as the droplet size approaches the pore size and may reach minutes or even longer.

4.4 Conclusion

In summary, we study the invasion of droplets into nanopores using molecular and continuum simulations. Depending on the applied pressure and the relative size of pore and droplet, three regimes can be found: spontaneous invasion, invasion by thermal activation, and blocking at pore entrance. The most interesting scenario occurs when the droplets have nanometer sizes and the pore width is comparable to the droplet diameter. When the droplet size is larger than the pore size, thermal activation can modestly expand the parameter space in which droplet can invade the pore compared to deterministic expectations. However, the disjoining pressure associated with the thin water film on the pore wall generally hinders the droplet invasion by driving up the energy barrier. In particular, when the droplet diameter is smaller than the pore size, disjoining pressure can lead to notable energy barriers for droplet invasion. These barriers are unlikely to be overcome by the hydrodynamic drag on the droplet but may be crossed through the Brownian motion of the droplet. In that case, the droplet entry time can increase dramatically as the droplet diameter approaches the pore size.

Our study highlights that, as droplets and the liquid films formed between the invading droplets and pore walls approach nanoscale dimensions, physics insignificant under other conditions, e.g. thermal activation and droplet blocking by wide pores due to the disjoining pressure, can become important. Understanding these nonlinear phenomena helps understand the non-Darcy multiphase flow behavior in nanoporous media and also helps improve the modeling of multiphase transport in unconventional porous media. For example, understanding the different invasion regimes and the spontaneous invasion pressure difference helps improve the pore-network models to achieve

more accurate prediction of droplet transport in shale reservoirs.

Supporting Information

All supporting information cited in this chapter is located in *Appendix C*.

Chapter 5. Structure, Thermodynamics, and Dynamics of Thin Film in Oil-Brine-Rock Systems

5.1 Introduction

Thin liquid films confined between surfaces are ubiquitous in nature and engineering systems, e.g. in colloids, foams, nanofluidic chips, desalination membranes based on layered materials, and porous electrodes of supercapacitors.[239, 327-329] The diverse chemistry of the confining surfaces and liquids, together with the confinement imposed by surfaces, endow thin liquid films with rich structure at molecular and mesoscopic scales. For example, water forms distinct layers with enhanced density near rigid, hydrophilic surfaces but depletion layers with reduced density near soft, hydrophobic surfaces.[330-333] When the confining surfaces carry net charges, an electrical double layer (EDL) emerge in the liquid film, and the EDL's structure depends strongly on the liquids' nature (e.g. solvent-free ionic liquids vs. dilute aqueous solutions), concentration of bulk ions, and the thickness of films, among other factors. Thin liquid films often exhibit dynamic properties different from bulk liquids and fascinating thermodynamics. The latter can manifest as the surface forces they mediate, the phase behavior they display, and the charge they store, *etc*. In particular, liquid films can mediate a host of surface forces with vastly different range and strength, e.g. the steric force, hydration force, hydrophobic force, double layer force, and van der Waals force. The structure, dynamics, and thermodynamics of thin liquid films play an essential role in numerous problems, e.g. the stability of colloids and foams, boundary lubrication, throughput of desalination by graphene-derived membranes, to name just a few.[334-338] As such, thin liquid films have been studied extensively using experimental, theoretical, and simulation approaches. [335, 339-340]

In petroleum reservoirs, which are essentially oil-brine-rock (OBR) systems, thin brine films are often found between rocks and oil droplets.[232-233] The thickness of these films depends on the nature of rock surfaces, the brine composition, and the properties of the oil droplets, and can range

from a few angstroms to tens of nanometers.[234-235] For example, using small-angle neutron scattering, it was shown that water films with a thickness of ~0.8-1.3nm exist on the surfaces of silica particles dispersed in heptane using anionic surfactants.[235] Despite their small thickness, brine films can play a fundamental role in the oil recovery from reservoirs. For example, the contact angle of oil droplets on rock surfaces, a primary factor governing the recovery of oil,[341] depends strongly on the disjoining pressure in these films.[227, 233] Indeed, some of the enhanced oil recovery (EOR) techniques are thought to function through the modification of thin brine films in OBR systems. For example, in low-salinity waterflooding (LSW), water with low salt concentration is injected into reservoirs and notable success has been reported in many field studies.[203, 226, 342-345] While multiple mechanisms are likely responsible for EOR, an emerging consensus is that the expansion of EDLs in the brine films caused by the decrease of brine's ion concentration and the ensuing increase of EDL disjoining pressure in the films play a key role by making the rock surface more water-wet.[227, 232] In addition to their structure and disjoining pressure, which affect the thermodynamics of EOR, the dynamics of brine films are expected to play a key role in determining the kinetics of LSW.[236, 254]

Insights on the structure, thermodynamics, and dynamics of brine films in OBR systems can potentially help improve existing EOR techniques and/or formulate new EOR concepts. While such insights may be derived from prior works on thin liquid films in other systems, some unique situations in OBR systems can make this approach difficult. In particular, the brine films in some OBR systems can have sub-nanometer thickness.[235] These brine films exhibit two interesting features. First, these brine films are confined by a solid rock with a rigid surface and an oil phase with a soft, diffusive surface. Second, the thickness of these brine films is comparable to key intrinsic length scales of the brine solution, brine-rock interfaces, and brine-oil interfaces (e.g. the Debye length of brine, the hydration diameter of the ions in brine, the characteristic length of the density oscillation of water molecules near rock surfaces, and the width of diffuse brine-oil interfaces). The combination of these features makes these brine films highly unique, and it is thus

difficult to extrapolate the insights obtained in the studies of other thin liquid films to them.

In principle, molecular dynamics (MD) simulations, in which the thin brine film, oil, and rock are resolved with atomistic resolution, can be used to gain insights into the molecularly thin brine films in OBR systems. Indeed, some molecular simulations of OBR systems have been reported, and insights such as effects of salinity on the wettability of oil on rock surface have been gained.[346-352] However, the brine films in these studies, if exist, are often bound by oil droplets or pores with a width of several nanometers. With this type of setup, the brine films usually extend less than 2nm laterally and its thickness varies greatly in the lateral direction. Consequently, these studies do not address the situation of extended brine films encountered in practice. Indeed, many questions on the structure, thermodynamics, and dynamics of extended brine films found in practical OBR systems remain open. For example, what is the molecular structure of the rock-brine and brine-oil interfaces in these films and how do these interfaces evolve as the brine film approaches molecular thickness? How are ions distributed in the EDLs in the brine film and how does the ion distribution respond to the changes of bulk ion concentration and film thickness? What is the disjoining pressure inside these films? What is the relative contribution of the hydration and EDL forces to the total disjoining pressure? How do these forces change with the film thickness and bulk ion concentration?

In this work, we perform extensive MD simulations to study extended brine films sandwiched between rock surfaces and thick slabs of oil. The rest of the manuscript is organized as follows. In Section 5.2, the molecular system and simulation methods are presented. In Section 5.3, the structure of brine films and the disjoining pressure in them are quantified at several film thickness and brine concentration, and the mechanisms underlying the observed results are discussed. The dynamic properties of the brine films are also presented. Finally, conclusions are drawn in Section 5.4.

5.2 Models and Methods

The molecular modeling of OBR systems is complicated by the diverse composition of oil, brine, and rock in oil reservoirs: the rocks can be sandstone or carbonate;[232] the brine can contain a variety of ions, e.g. Na^+, Cl^-, Ca^{2+}, Mg^{2+}, *etc*; the oil is a mixture of many hydrocarbons, basic and acidic groups (e.g. naphtenic acids), and impurities. Since the molecular study of OBR system is very limited at present, we focus on a simplified description of OBR here. Quartz slabs are used as model rock because quartz is a key component of sandstone. Aqueous NaCl solution is used as the brine, and pure *n*-decane is used as the oil. The surface of the quartz slabs facing brine and oil is negatively charged in most simulations to be consistent with experimental data at typical pH, although neutral surfaces are also considered as a reference (see below). The oil-brine interface is neutral, which corresponds to the limit of very low density of electroactive species at the water-oil interfaces.[353]

Simulation systems. Three types of systems have been simulated. The first type of system, the "*thin brine film*" system, is used to study molecularly thin brine films confined between rock and oil surfaces. As shown in Fig. 5-1a, this type of system consists of a quartz slab, an oil reservoir, a brine reservoir and brine film, and two rigid pistons bounding the oil and brine reservoirs. The quartz slab is ~3nm thick. Its surface facing the brine film and oil has a surface charge density of $-0.12 C/m^2$. A brine film is formed between the upper rock surface and oil phase and it is connected with the brine reservoir. Its thickness ranges from 0.7 to 1.0nm, which is within the range of brine film thickness revealed by neutron scattering.[232, 253] To maintain a bulk like behavior at position away from the rock surface, the brine and oil reservoirs measure ~5nm and ~4nm in the *z*-direction, separately. The top piston is used to control the thickness of the brine film (see below); the bottom piston is used to prevent water molecules from evaporation and it is allowed to move freely in the *z*-direction. The system is periodic in all directions, but two large vacuum spaces are placed outside of the pistons to effectively remove the periodicity in the *z*-direction. The simulation box measures $14.00 \times 3.93 \times 18.00 nm^3$ in *x*-, *y*-, and *z*-directions, respectively.

Apart from the setup in Fig. 5-1a, thin brine film systems without an explicit brine reservoir (see Fig. 5-1b) are also studied. Specifically, after a system shown in Fig. 5-1a reaches an equilibrium, its middle portion (delineated using a red dashed box) is extracted to build the system shown in Fig. 5-1b. In doing so, the chemical potential of the brine film in the new system is the same as that in the original system featuring an explicit brine reservoir, but the dimension (and thus computational cost) of the new system is smaller. The systems thus set up are used to study the hydrodynamic properties of thin brine films.

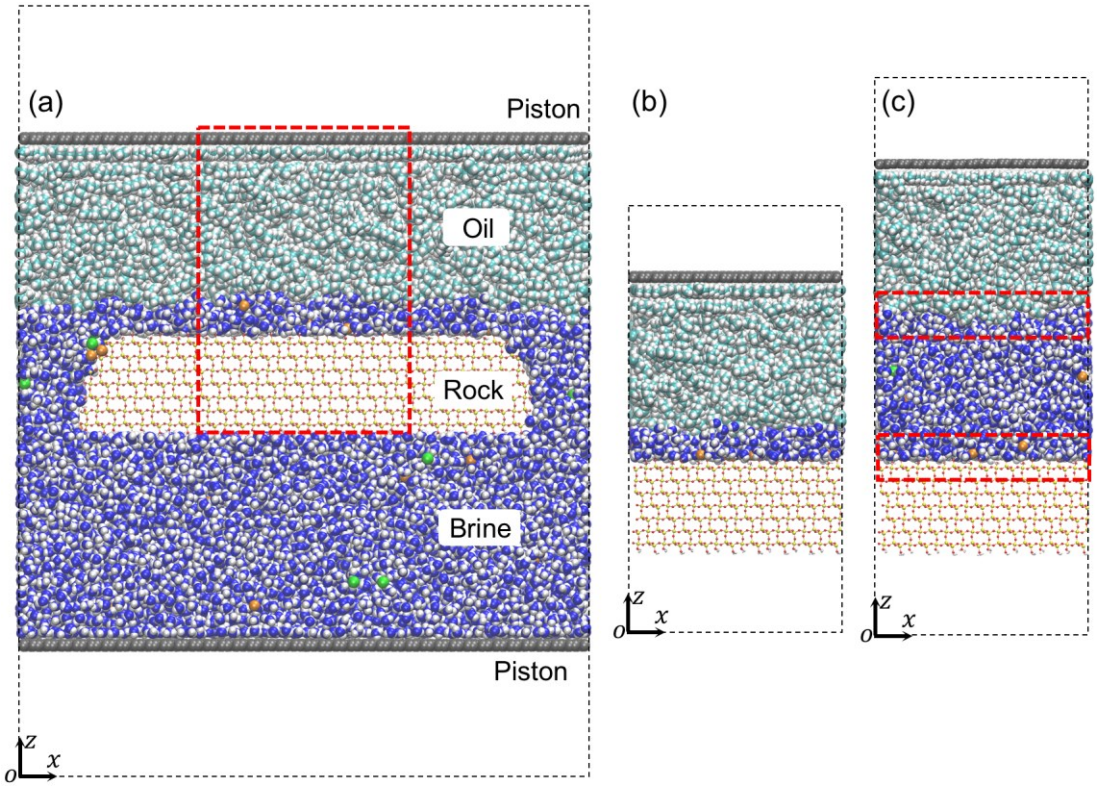

Figure 5-1. *The molecular systems for studying oil-brine-rock (OBR) systems.* **(a)** A snapshot of a model OBR system featuring a thin brine film, brine reservoir, and a thick oil slab. The pressure in the brine reservoir and oil is regulated using two rigid pistons. The black dashed box shows the simulation box. The 5.5nm-wide red box denote the region in which the statistics of brine films are taken. **(b)** A snapshot of system for investigating the dynamic properties of brine film. **(c)** A snapshot of a reference system for studying the isolated rock-brine and unconfined brine-oil interfaces. The brine film is ~4nm thick so that the brine-rock and brine-oil interfaces do not affect each other. Water is shown as blue (oxygen) and white (hydrogen) spheres. Oil (*n*-decane) is shown as cyan (carbon) and white (hydrogen) spheres. Na^+ and Cl^- ions are shown as orange and green spheres respectively. Rock is made of α-quartz and shown using a bar-and-stick model.

The second type of system, the "*thin water film"* system, is similar to the *thin brine film* system except that the quartz surface is neutral and there are no ions in the system. This type of systems is used to study the hydration force in thin water films in absence of any surface charge and salinity effects. The third type of system is the "*reference"* systems. In this type of system, a thick brine slab (~4nm thick) is sandwiched between a thick oil slab (~4nm thick) and the quartz slab (see Fig. 5-1c). Because bulk-like behavior is achieved for the water and oil away from the rock-brine and brine-oil interfaces, the rock-brine and brine-oil interfaces do not affect each other noticeably. Therefore, this type of systems allows us to study the brine/EDLs near isolated rock surfaces and unconfined oil-brine interfaces, which are useful references for understanding the behavior of thin brine films.

Table 5-1. *The parameters of the three types of systems.*

	Thin brine film	Thin water film	Reference
System snapshots	Fig. 5-1a, Fig. 5-1b	-	Fig. 5-1c
Brine (water) film thickness	0.7nm – 1.0nm	0.7nm – 1.0nm	~4.0nm
Oil slab thickness	~4.0nm	~4.0nm	~4.0nm
Salt concentration	0.1M, 1M	0	0, 0.1M, 1M
Quartz slab's surface charge density	-0.12 C/m^2	0	0, -0.12C/m^2
Box length in *x, y, z*-directions	14.00×3.93×18.00nm^3 5.50×3.93×10.00nm^3	14.00×3.93×18.00nm^3 5.50×3.93×10.00nm^3	5.50×3.93×13.00nm^3

For the first type of OBR systems, four systems with two different brine film thicknesses and two different brine concentrations are studied; for the second type of systems, two systems with two different brine film thickness are studied; for the third type of systems, two systems with a bulk ion concentration of 0.1M and 1M are studied. The brine film thickness, brine reservoir ion concentration, and other parameters of the three types of systems are summarized in Table 5-1.

Molecular models. Water is described using the rigid SPC/E model.[314] *n*-decane is modeled using the optimized parameter set of the original OPLS-AA force fields for hydrocarbons.[354] The

force fields parameters for Na^+ and Cl^- ions are taken from Ref. 355. The rock is made of α-quartz. Its upper and lower surfaces are cleaved from the (101) plane by following the recent study of quartz-water interface,[315] yielding a surface silanol group density of 5.92 per nm^2. This silanol group surface density leads to a strongly hydrophilic surface as suggested by previous work,[356-357] which facilitates the formation of brine film on the quartz surface in OBR systems.[271, 310, 357] Following prior work,[315] the zero plane of the quartz slab is defined as the *z*-position of the second outmost layer of surface silicon atoms (see Fig. SD-1 in *Appendix D*). The outmost silanol groups of the quartz surface facing the oil phase are selectively deprotonated using the method in Ref. 315 to produce a net surface charge density of $-0.12 C/m^2$. The force field parameters of the quartz thus prepared, including the Lennard-Jones (LJ) parameters and partial charges are taken from the CLAYFF force fields.[265, 315] To reduce computational cost, the silicon and oxygen atoms of the quartz slab are fixed and their non-electrostatic interactions with each other are excluded. The hydrogen atoms of the surface silanol groups are allowed to move by considering their bonded interactions with other atoms in the quartz slab. The LJ parameters for the interactions between dissimilar atoms are obtained using the Lorentz−Berthelot combination rule. The LJ potentials, partial charges and bonded parameters of atoms in the systems studied here are listed in *Appendix D*.

Simulation methods and protocol. All simulations are performed using the Gromacs code (version 4.5.6).[358] The bond length and angle of water molecules are constrained using the SETTLE algorithm. All simulations are done in the NVT ensemble with a temperature of 350K, which is relevant to typical reservoir conditions.[288, 359] The temperature is maintained using the velocity rescale thermostat[289] with a time constant of 1ps. A global cutoff of 1.2nm is used for computing the LJ potentials, and the particle mesh Ewald method with a slab correction to remove the periodicity in the *z*-direction is used to calculate the electrostatic interactions.[317]

The first type of systems with explicit brine reservoirs (see Fig. 5-1a) are built and equilibrated

in four stages. In the first stage, a ~3nm thick brine slab is initially enclosed between the quartz surface and oil slab. The top piston is allowed to move in the *z*-direction without applying any external force to it and the system is equilibrated for 4ns. In the second stage, a 20MPa pressure is exerted on the top piston to push the oil and brine downward to form a thin brine film between the oil and the quartz surface. During this stage, the thickness of the brine film in the middle portion of the system is recorded. Once the film thickness reaches 0.9 or 0.7nm, the piston is fixed in space. In the third stage, the system is equilibrated further with the piston fixed. The pressure on the top piston and the number of ions and water molecules in the middle portion of the brine film (denoted by the red dashed box in Fig. 5-1a) are monitored with time. Typically, the pressure and water and ion number in the brine film reach their equilibrium values within 200-500ns (see Fig. SD-2 and Fig. SD-3 in *Appendix D*). In the final stage, the system is simulated for another 100ns to gather statistics. The equilibrium thickness of brine films built using this protocol is not prescribed *a priori* and usually differs from the film thickness at the end of the second stage. Through trial and error, the thickness of equilibrated film has been adjusted to within 0.02nm of the target values.

The first type of systems without explicit brine reservoirs (see Fig. 5-1b) is built based on the composition of the brine film obtained at the end of the third stage. Once built, the system is equilibrated for 50ns first and then followed by the shearing simulations described in Section 5.3.4. The second type of system are built and equilibrated in a similar way as the first type of system. The third type of system is built by stacking thick oil and brine slabs and then equilibrating the system for 100ns.

5.3 Results and Discussions

5.3.1 Structure of interfacial water and oil

We start with the structures of the interfacial water and oil in thin brine films, with a focus on how these structures differ from those near unconfined water-oil interfaces and isolated water-rock interfaces. The results presented below are based on systems featuring brine reservoirs with an ion

concentration of 0.1M. Similar interfacial oil and water structures are observed for the 1M brine concentration cases and are not shown.

Water-oil interfaces. Figure 5-2 shows the water and decane density profiles in/near two brine films. The thickness of these brine films, h, is difficult to define uniquely. Here, h is defined from the perspective that a brine film is confined between the quartz and oil surfaces. Because water molecules can access the space ~0.22nm above the quartz slab's zero plane, the effective surface of the quartz slab can be assigned to z=0.22nm (see Fig. 5-2a). For decane, using the convention of assigning the position of diffusive interfaces, its nominal surface is taken as the position where its density is 50% of the bulk density. With the above definition, the thickness of the brine films shown in Fig. 5-2a and 5-2b is determined as 0.74 and 0.94nm, respectively. The space below (above) the nominal decane surface is shaded using blue (green) color to reflect the fact that this space is occupied predominately by brine (oil).

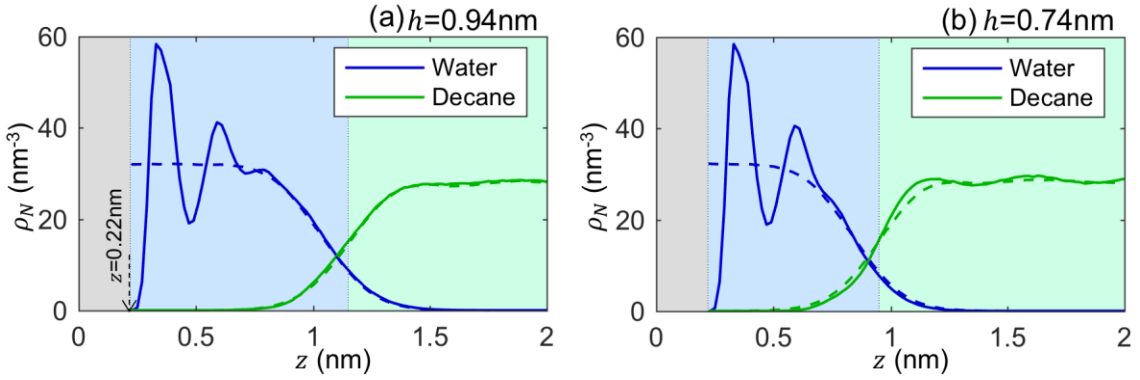

Figure 5-2. *The water-oil interface in brine films.* **(a-b)** The density profiles of water and oil in brine films with a thickness of 0.94nm (a) and 0.74nm (b). The water density is calculated based on its center of mass position and the oil density is calculated from the number density of carbon atoms. The space shaded with blue and green colors denotes the water and oil phases, which are separated by a plane where decane density is half of its bulk value. The dashed lines show the reference density profiles of interfacial water (in blue) and decane (in green) near unconfined brine-oil interfaces. The reference density profiles are placed such that the water-oil phase boundary meets.

Figure 5-2a shows that, when the brine film is 0.94nm thick, the density profiles of water and decane near water-oil interface are practically identical to these near unconfined interfaces. As the film is thinned to 0.74nm, the density profile of water very close to the water-oil interface remains

little changed, but that of the oil becomes slightly sharper (see Fig. 5-2b). The latter means that the oil surface bounding a brine film becomes sharper (more well-defined) when film is thinned to ~2-3 layers of water molecules. Sharper oil surfaces are also observed in brine films with bulk ion concentration of 1M (see Fig. SD-4 in *Appendix D*).

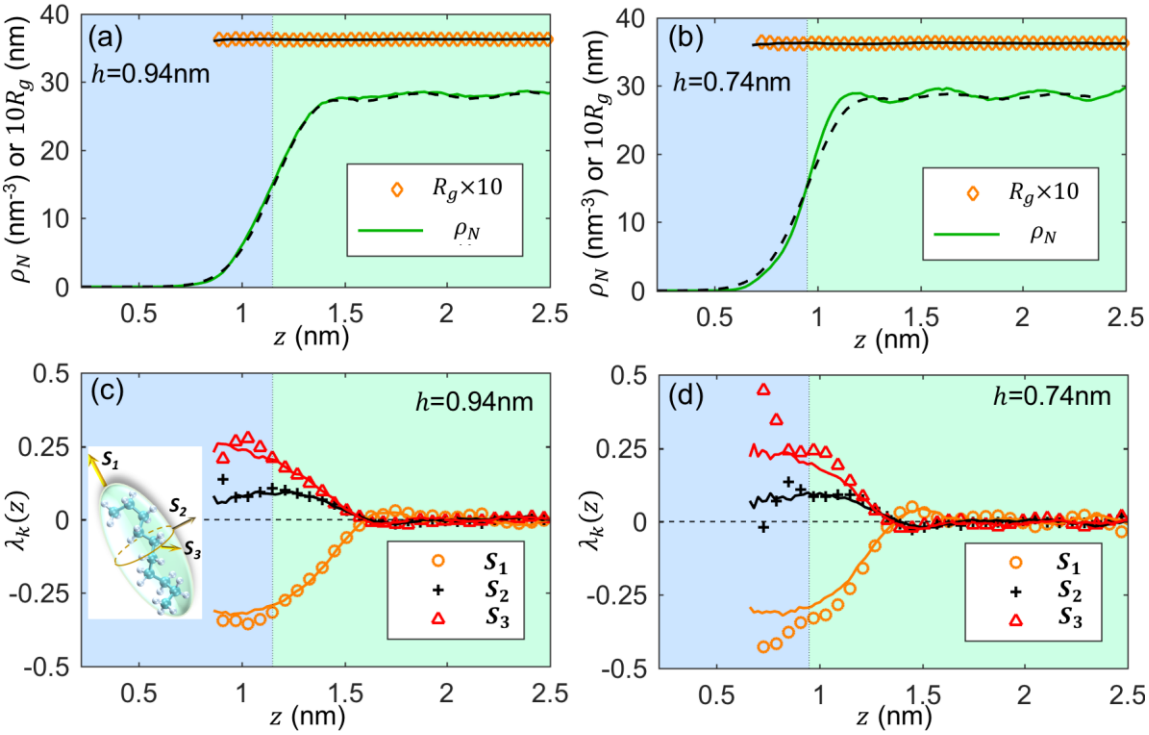

Figure 5-3. *The structure of oil near brine film-oil interfaces.* (**a-b**) The density and radius of gyration of decane near brine film with a thickness of 0.94nm (a) and 0.74nm (b). Similar profiles near unconfined brine-oil interfaces are shown as black lines. (**c-d**) The orientation order parameter of decane molecule's three principal axes near brine films with a thickness of 0.94nm (c) and 0.74nm (d). Data for brine film-oil interfaces are shown as symbols, whereas these for unconfined brine-oil interfaces are shown as solid lines with the same color. The inset in (c) shows the three principal axes of a decane molecule.

Structure of interfacial oil. The sharper oil surface above thinner brine films is caused by the fact that, as a brine film becomes thinner, the oil molecules above it maintain similar conformation but take a more parallel alignment with respect to the brine-oil interfaces. To show this, we fit each decane molecule into an ellipsoid and determine its three principal axes $\boldsymbol{S}_k$ (k=1, 2, 3) and radius of gyration R_g (see Fig. 5-3c's inset and *Appendix D*). The orientation of the decane molecule at position z with respect to the oil-brine interface is characterized by the order parameter

$$\lambda_k(z) = \langle 3(\boldsymbol{S}_k(z) \cdot \boldsymbol{n_z})^2 - 1 \rangle / 2, \quad (5.1)$$

where $\langle \cdot \rangle$ denotes the ensemble average, $\boldsymbol{n_z}$ is the unit normal vector of the oil-brine interface. $\lambda_k = 1$ (–0.5) if decane's k-th principal axis is normal (parallel) to the oil-brine interface.

Figure 5-3a and 5-3b show the radius of gyration of the decane molecules near brine-oil interfaces. We observe that R_g of decane molecules is maintained at 0.36nm regardless it is in bulk oil or at any position across water-oil interfaces, the latter has also been reported in prior work of interfacial hydrocarbon with similar chain length.[360] These results indicate that the conformation of decane molecule in contact with the brine film is little changed as the film is thinned.

Figure 5-3c and 5-3d show the order parameters of the principal axes of decane molecules near the brine-oil interfaces. As a decane molecule approaches a unbounded brine-oil interface, its longest axis becomes more parallel to the interface, indicating it tends to "lay" on the brine surface, similar to that reported for linear alkanes near isolated water-oil interfaces.[330] When the brine film is 0.94nm-thick, the orientation ordering of the decane molecules near this film is nearly identical to that near unbounded brine-oil interfaces. As the film is thinned to 0.74nm, λ_1 of the decane molecules in contact with the brine film decreases toward –0.5 while λ_3 increases toward 1.0, suggesting that the interfacial decane molecules adopt a more parallel orientation with respect to the brine surface. Because decane molecules in contact with the brine films are better aligned with the brine surface, these molecules tend to occupy a narrower space in *z*-direction, thus making the oil surface sharper. The more parallel orientation of interfacial decane above the 0.74 nm-thick brine film can be understood as follows. Many decane molecules right above the 0.94nm-thick film are in contact with water with a density close to bulk water (see Fig. 5-2a); many decane molecules above the 0.74nm-thick film are in contact with the second water peak near quartz surfaces, which are packed more densely than bulk water (see Fig. 5-2b). Because it is more difficult to insert a decane molecule into more densely packed water, more decane molecules will "lay" on the surface of the 0.74nm-thick brine film, thus leading to a sharper oil surface.

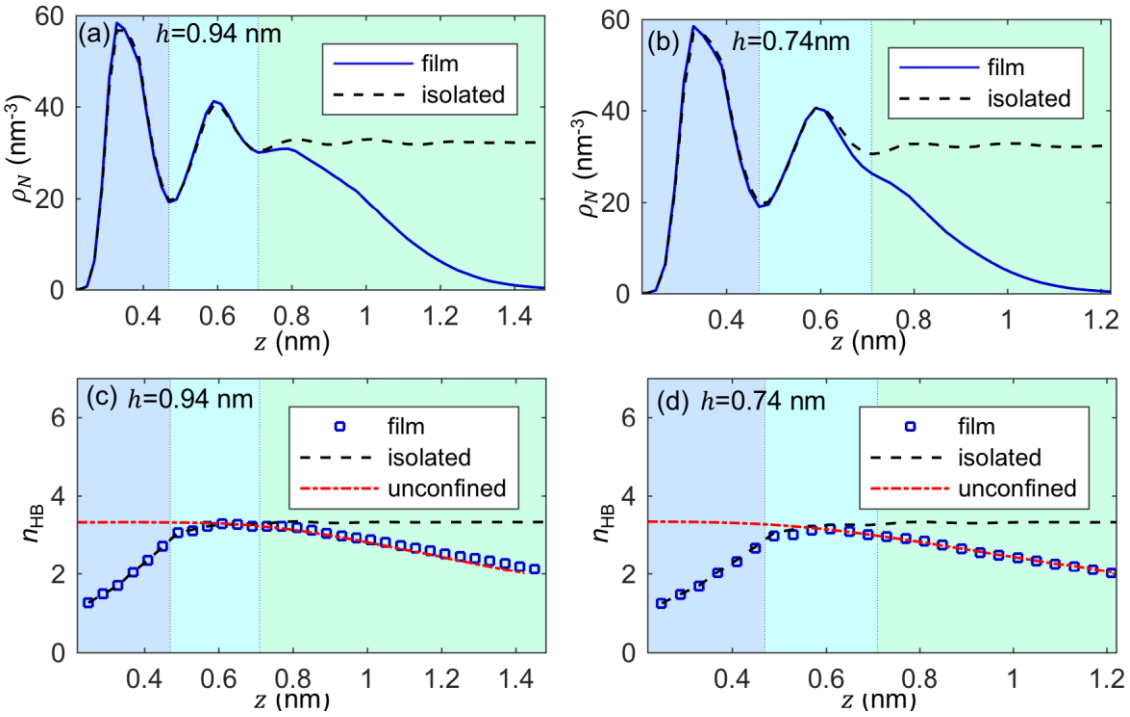

Figure 5-4. *The water-rock interface in brine films.* **(a-b)** The density profiles of water near isolated quartz surface and across brine films with a thickness of 0.94nm (a) and 0.74nm (b). The shaded areas denote the three water layers based on the two valleys positioned at z_1=*0.*47and z_2=*0.*71nm. **(c-d)** The hydrogen bond number profile of water molecules in brine film with a thickness of 0.94nm (c) and 0.74nm (d). The hydrogen bond profiles near unconfined interface are placed in a way similar to the water/oil density profiles in Fig. 5-2.

Water-rock interfaces. Figure 5-4a and 5-4b show the water density profiles near quartz surfaces bounding brine films with a thickness of 0.94 and 0.74nm, respectively. The density profile of water near isolated quartz surface, which shows two distinct water layers centered at z=0.34 and 0.60nm as observed in previous works,[315] is also included in Fig. 5-4 as a reference. The water in the brine film can be divided into three layers according to the two valleys positioned at z_1=0.47nm and z_2=0.71nm (1st layer: $z_0 < z < z_1$; 2nd layer: $z_1 < z < z_2$; 3rd layer: $z > z_2$). The water density in the third layer closely resembles that near the unconfined oil-water interfaces (see Fig. 5-2a and 5-2b). As brine films are thinned to 0.94nm, the first two layers of water remains intact; only when the brine film is thinned to 0.74nm, does the second water layer become disturbed by the presence of water-oil interfaces nearby. The fact that the water-rock interface is hardly

disturbed in brine film down to about three water layers is a consequence of the strong interactions between water and the quartz surface: the first water layer interacts strongly with the surface silanol groups, whereas the second water layer mainly interacts with the densely packed water in the first layer. The soft, hydrophobic surface of oil impacts only the layer of water molecules in direct contact with it.

The strong water-water/quartz interactions in the first two water layers near the quartz can be observed from the hydrogen bonds formed by the water molecules in brine films. The geometric criteria are used for hydrogen bonds,[361] i.e. a hydrogen bond exists if L_{oo}<0.35 nm and $\angle$OOH≤30° (L_{oo}: oxygen-oxygen distance; $\angle$OOH: angle formed between one water molecule's OH bond and the oxygen-oxygen vector pointing from the donor to the acceptor). As shown in Fig. 5-4c and 5-4d, the number of hydrogen bonds per water molecule, n_{HB}, is smaller for water in the first layer than in the bulk due to their favorable interactions with surface silanol groups. n_{HB} is close to the bulk value in the second water layer, indicating dominant water-water interactions in this layer. Similar to the density profiles, the profile of n_{HB} near the rock surface and the oil surface closely resembles that near isolated quartz surface and unconfined oil-water interface, respectively. As a side note, in both brine films, the orientation of their two layers of water molecules can deviate from that near isolated quartz surfaces (see Section 5.3.3).

The above results show that, in brine films as narrow as 2-3 water layers, the packing of water molecules as well as the coordination between them can be reasonably approximated as those near isolated rock-brine interfaces and unconfined oil-brine interfaces. This is different from the water confined between two rigid surfaces, where the structure of water near one surface can be modified greatly when the two surfaces approach each other closely.[362]

5.3.2 Structure of electrical double layers

In this part, we investigate the structure of EDLs in the thin brine films when the quartz slab has a surface charge density of σ=–0.12C/m^2. The ion concentration in the brine reservoir is 0.1M

unless otherwise mentioned. We focus on the evolution of the ion distribution as the brine film thickness reduces and what are the underlying mechanisms.

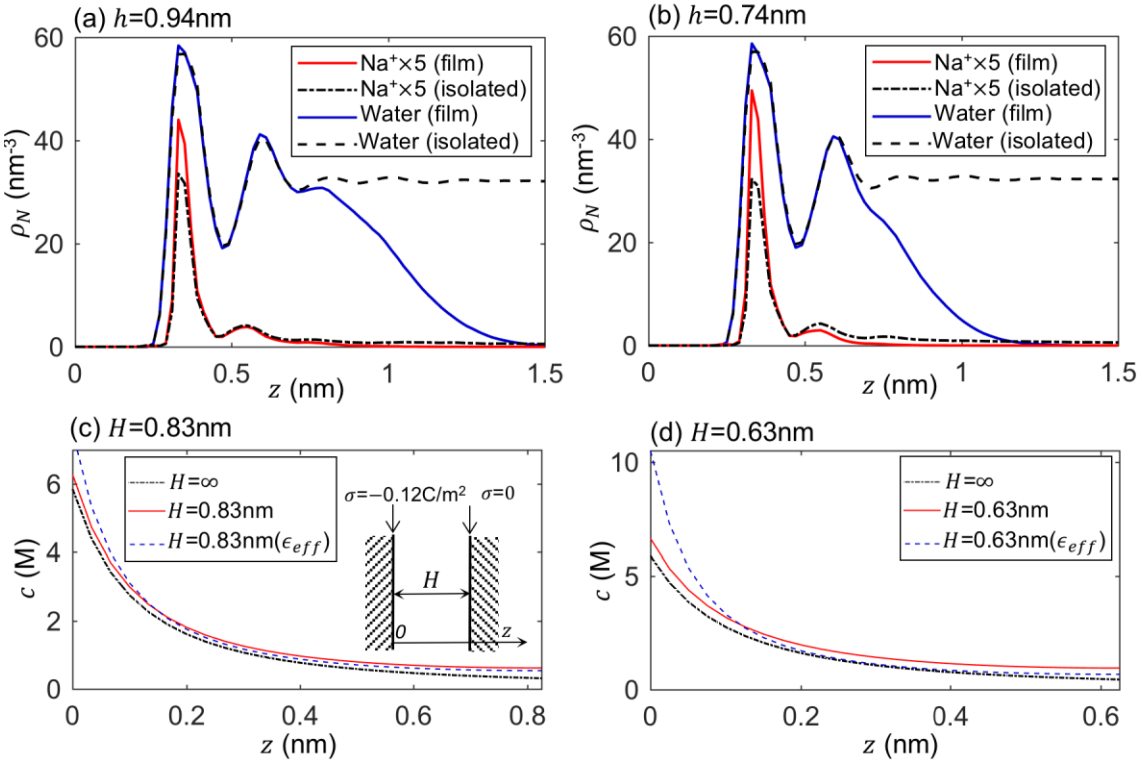

Figure 5-5. *Electrical double layers in brine films.* (**a-b**) The density profiles of Na^+ ions and water near isolated quartz surface and in thin films with a thickness of 0.94nm (a) and 0.74nm (b). (**c-d**) The Na^+ ion density predicted by the Poisson-Boltzmann equation in the brine film with an ion-accessible thickness of 0.83nm (c) and 0.63nm (d). The inset in (c) is the continuum model of the brine film. The ion-accessible thickness H is defined as the distance between Na^+'s first peak and the nominal oil surface. The brine film is in equilibrium with a brine reservoir with an ion concentration of 0.1M. The co-ion density is not shown because of their very small values.

Ion distribution. Figure 5-5 shows the density profiles of Na^+ ions in two brine films and near isolated quartz surfaces. The density profile of Cl^- ions is not shown because of their very small value, especially inside the brine films. Regardless of brine film thickness (note that an isolated quartz surface is effectively bounded by a very thick brine film), two Na^+ density peaks appear at z=0.33 and 0.55nm. The location of these peaks is in excellent agreement with prior studies of EDLs near the same quartz surface.[315] As the brine film is thinned, the evolution of Na^+ density profiles shows two features. First, the Na^+ density away from the quartz surface (e.g. at the second

Na^+ peak) decreases noticeably. For example, in the 0.74nm-thick film, the height of the second Na^+ peak is reduced to 1/3 of its height near an isolated quartz surface. Second, the first Na^+ peak grows by 28.7% and 44.6% compared to that near isolated quartz surfaces as the film is thinned to 0.94nm and then to 0.74nm.

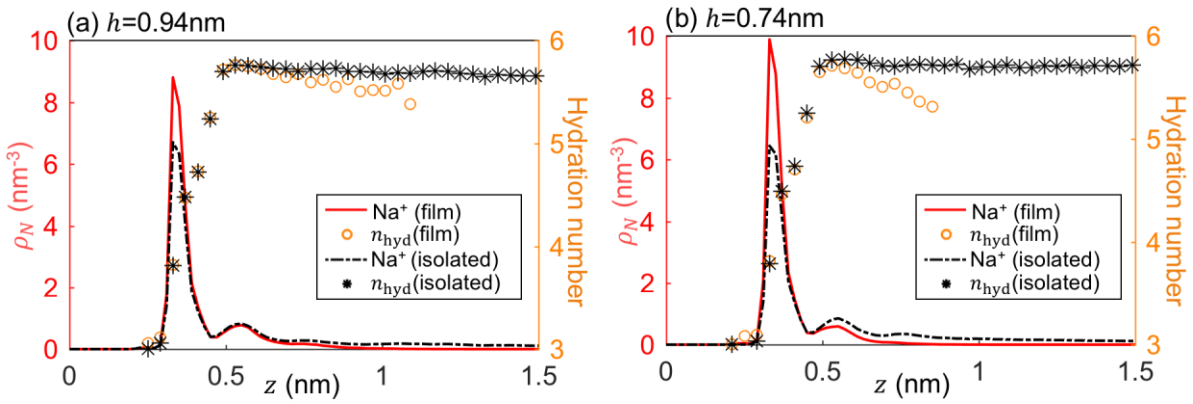

Figure 5-6. *The ion hydration number profiles in brine films.* The density and hydration number of Na^+ ions across brine films with a thickness of 0.94nm (**a**) and 0.74nm (**b**). The brine film is in equilibrium with a reservoir with an ion concentration of 0.1M.

The first feature and the very existence of the second Na^+ peak are primarily caused by the ion hydration effect. In classical EDL theories such as the Poisson-Boltzmann (PB) equation, the ion distribution is governed by long-range ion-ion electrostatic interactions and water acts only as a dielectric medium. However, water also behaves as a molecular solvent that hydrates ions, and the related short-range ion-water interactions have been found to greatly affect the ion distribution in EDLs.[363-368] To explore this effect, we compute the hydration number of Na^+ ions (n_{hdr}) by counting the number of water molecules in its first hydration shell (i.e. $r_{\mathrm{water-Na^+}}$ <0.31nm, see *Appendix D*). Figure 5-6a and 5-6b show that n_{hdr} of Na^+ ions shows a local maximum at z=0.53nm, which is caused by the non-homogeneous distribution (layering) of water molecules near the quartz surface. Because a Na^+ ion is hydrated by more water molecules at this location than in bulk, it is energetically favorable to reside here, thus helping explain the second Na^+ peak at z=0.55nm. We note that similar solvent-induced effects have been reported in prior MD and DFT simulations of EDLs near solid surfaces.[363-368]

As a brine film is thinned, the oil surface moves toward to the quartz surface. Since the water density is reduced near an oil surface, the ion hydration at a given distance from the quartz surface is reduced. For example, in the 0.74nm-thick brine film, n_{hdr} of Na^+ ions in the region z>0.5nm is markedly smaller than that in the 0.94nm-thick brine films. Consequently, the Na^+ density in this region is lower than in the 0.94nm-thick brine films.

The second feature of Na^+ density evolution, i.e. the increase of the first Na^+ density peak as brine films are thinned, can be caused by several factors. First, as brine films are thinned, Na^+ ions in region away from the quartz surface are depleted as explained above. The number of Na^+ ions in the film, however, is largely unchanged because they must balance the charge on the quartz surface (note that the number of Cl^- ions in the brine film is negligible under the reservoir concentration studied here). Therefore, the Na^+ density close to the quartz surface will increase. Second, as brine films are thinned, even if Na^+ ions are not repelled away from the oil surface due to the hydration effect, these ions are confined in a narrower space and thus the Na^+ density near the quartz surface should increase. Assessing whether the increased confinement in thinner brine films can lead to the higher first Na^+ peak is difficult because, ideally, this confinement effect should be evaluated using a model that incorporates all relevant physics (e.g. ion hydration effects) in addition to the geometrical confinement. While such models do exist, they often requires empirical parameters as inputs.[369] Here, we use the classical PB equation to gain a qualitative understanding only.

As shown in Fig. 5-5c' inset, in the PB model, each brine film is taken as a slit pore bounded by one charged wall (mimicking the quartz surface) and one neutral wall (mimicking the neutral oil surface). Because the first Na^+ density peak at z=0.33nm is 0.11nm away from the nominal brine-quartz interface (see Fig. 5-5a and Fig. 5-2a), the width of the slit pore, H, is taken as 0.83 (0.63nm) for the 0.94nm (0.74nm)-thick brine film. The dielectric constant inside the pore, ε_r, is set to 56.83±1.31, which is computed for bulk SPC/E water at 350K (see *Appendix D*).[370-371] As

shown in Fig. 5-5c and 5-5d, the density of Na^+ ions on the pore increases by 7.4% and 12.9% as H decreases from ∞ to 0.83nm and 0.74nm, respectively. Such an increase is much smaller than the increase of first Na^+ peak observed in Fig. 5-5a and 5-5b, suggesting that the increased confinement in thinner brine films is likely not the direct reason for the increased Na^+ adsorption on the quartz surface.

Dielectric effects. In the above analysis based on the PB equation, the dielectric constant of the brine film is taken as that of bulk water. However, the dielectric response of nano-confined water is known to differ greatly from that in bulk,[372-374] which can modify electrostatic interactions between ions and thus affects the ion distribution in the brine film. To appreciate the dielectric effects in molecularly thin films, following the work by Netz and co-workers, we compute the dielectric profile of water in thin water films near neutral quartz surfaces.

The *thin water film* systems in Table 1 with a film thickness of 0.72, 0.92, and 4nm are studied. The component of dielectric constant in direction perpendicular to the quartz surface is of primary interest and computed following the linear response theory.[373, 375-376] Specifically, a perpendicular polarization correlation function is defined as

$$c_\perp(z) = \langle m_\perp(z) M_\perp \rangle - \langle m_\perp(z) \rangle \langle M_\perp \rangle \quad (5.2)$$

where $\langle \cdot \rangle$ denotes the time average. $m_\perp(z)$ is perpendicular polarization density at position z, which is evaluated via $m_\perp(z) = -\int_0^z \rho_e(z')dz'$ (ρ_e is the space charge density). The total perpendicular polarization of the simulation box is $M_\perp = L_x L_y \int_0^{L_z} m_\perp(z)dz$, where L_x, L_y, and L_z are the box length in the *x-, y-,* and *z*-directions, separately. Using the fluctuation-dissipation theorem,[374-375] the inverse perpendicular dielectric profile of a periodic system is related to $c_\perp(z)$ via

$$\varepsilon_\perp^{-1}(z) = 1 - c_\perp(z)/(\varepsilon_0 k_B T + C_\perp/V), \quad (5.3)$$

where ε_0 is the vacuum permittivity, k_B is Boltzmann constant, T =350K is the system temperature, $C_\perp = L_x L_y \int_0^{L_z} c_\perp(z)dz$ is the variance of the total polarization, and V is the simulation

box volume. For thick enough water films, $\varepsilon_{\perp}^{-1}(z)$ should approach $1/\varepsilon_r$ at position away from the confining surfaces.

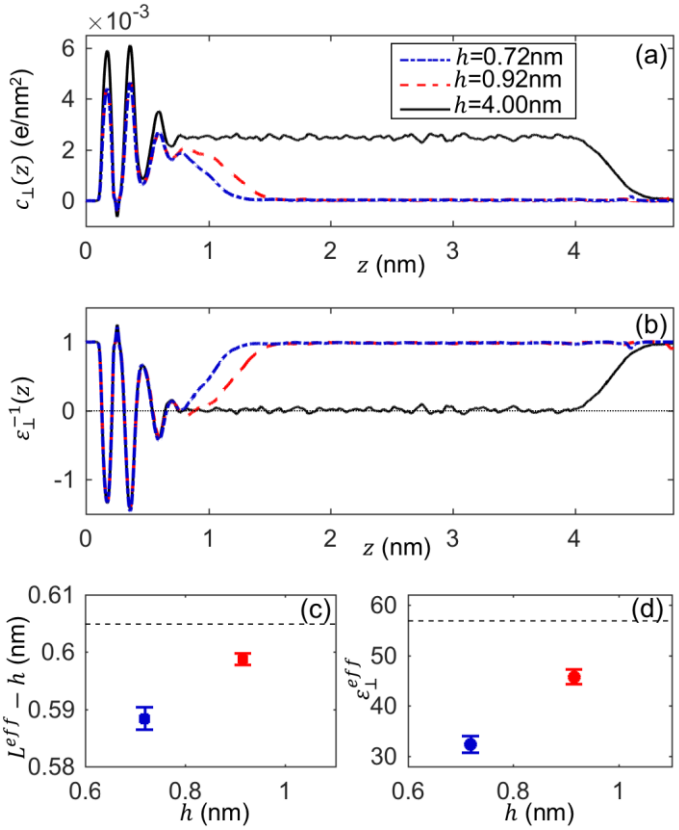

Figure 5-7. *The perpendicular dielectric profiles in thin films*. **(a)** The polarization correlation function near the quartz surface. **(b)** The inverse perpendicular dielectric profile near the quartz surface. **(c)** The shift of effective dielectric box length with respect to the film thickness. The dashed line denotes the shift when the water film is 4.0nm thick. **(d)** The effective dielectric constant in direction normal to the quartz surface. The dashed line denotes the static dielectric constant of bulk water.

Figure 5-7a shows the perpendicular polarization correlation function in the water films studied. Near the quartz surface, whose zero plane is located at z=0, the $c_{\perp}(z)$ profiles of the two thin water films are undistinguishable from each other, but are overall lower than that for the case with H=4nm because of the larger $M_{\perp}$ for the much thicker water film. The corresponding $\varepsilon_{\perp}^{-1}(z)$ profiles are shown in Fig. 5-7b. One can observe that, near quartz surface, $\varepsilon_{\perp}^{-1}(z)$ crosses zero several times and exhibits negative values in some regions, i.e. $\varepsilon_{\perp}(z)$ can become negative or diverge locally. Similar phenomena have been reported for water near many types of substrates,

and they correspond to the over-screening of surface charge at some positions by water.[373, 375-377] While it is not straightforward to evaluate how the complex $\varepsilon_{\perp}(z)$ affects dielectric screening in the water film, the complex $\varepsilon_{\perp}^{-1}(z)$ profile can be used to construct a coarse-grained dielectric box model that approximates the film as a continuum with a uniform effective dielectric constant.[373] From the linear response theory, such a dielectric box model effectively reproduces the integral over the electrical field by

$$\int_0^{L_z}(\varepsilon_{\perp}^{-1}(z)-1)dz = L_{\perp}^{eff}(1/\varepsilon_{\perp}^{eff}-1). \qquad (5.4)$$

where $L_{\perp}^{eff}$ and $\varepsilon_{\perp}^{eff}$ are the effective dielectric box length in the z-direction and the effective perpendicular dielectric constant within the box, separately. As practiced in the original dielectric box model,[373] one first computes $L_{\perp}^{eff}$ by taking $\varepsilon_{\perp}^{eff}$ to the dielectric constant of bulk water (56.83 here). Using the $L_{\perp}^{eff}$ thus obtained, a shift $\delta = L_{\perp}^{eff} - h$ is obtained (h is the water film thickness). The effects of the quartz slab, oil phase, and water film on the dielectric profile are all lumped into the shift δ. Since quartz slab and oil phase are the same in systems with different water films, the perpendicular dielectric profiles are the same in them (data not shown here). Therefore, δ in systems with different water film thickness h provides a measurement of how the dielectric environment is changed when h changes. Typically, δ varies monotonically as a water film becomes thicker and approaches an asymptotic value δ_0 when h is larger than a few nanometers. In thin films, it has been established that $\varepsilon_{\perp}^{eff}$ can be obtained using Equ. 5.4 and the effective dielectric box length based on the asymptotic shift ($L_{\perp}^{eff} = h + \delta_0$).[373]

Figure 5-7c shows the shift δ in three water films. The shift δ for 4.0nm-thick film is 0.715nm. This value is taken as the asymptotic shift δ_0 and labeled using a dashed line. As the film thickness decreases to 0.92 and 0.72nm, δ is reduced to 0.709 and 0.698nm, respectively. The magnitude of δ for our water films, which are confined between a rigid quartz surface and a soft decane slab, is similar to that of the water films confined between two polar walls with similar separations.[373] δ decreases as a water film is thinned, indicating a decrease of the dielectric

efficiency of nano-confined water in direction normal to confining surfaces. Furthermore, using the method described above, the effective dielectric constant $\varepsilon_{\perp}^{eff}$ is found to decrease to 57% and 81% of the bulk dielectric constant in films with h =0.72 and 0.92nm, respectively (see Fig. 5-7d). Using these dielectric constants, the PB model sketched in Fig. 5-5c is solved again to evaluate how Na^+ density in brine films changes as they are thinned. As shown in Fig. 5-5c and 5-5d, the new PB model predicts that, as the film thickness decreases from $H = \infty$ to 0.94 and then 0.74nm, the maximal Na^+ density in the film increases by ~30% and ~80%. The larger increase observed here are in better agreement with the increase of the first Na^+ peak predicted by the MD simulations than when the dielectric decrement in thin films is neglected. Physically, as the effective dielectric constant in a film decreases, the Na^+-Na^+ and Na^+-surface electrostatic interactions are less screened, which leads to a stronger adsorption of Na^+ ions on the quartz surface.

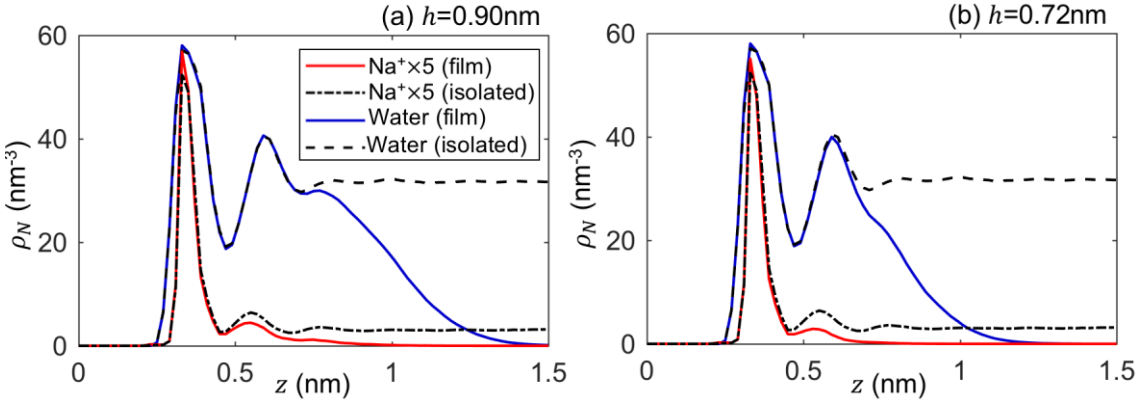

Figure 5-8. *Ion and water distribution in brine films with reservoir ion concentration of 1.0M.* **(a)** The film thickness is 0.90nm. **(b)** The film thickness is 0.72nm.

Salinity effects. We finally examine the EDL structure in brine films in equilibrium with brine reservoirs with an ion concentration of 1.0M. Figure 5-8 shows the counter-ion (Na^+) density profile across the film, along with the water density profiles (the co-ion density profiles are shown in Fig. SD-7 in *Appendix D*). The density of Na^+ ions is much reduced near the oil surface for the 0.90nm- and 0.72nm-thick brine films, again due to the reduced ion hydration near oil surfaces as explained above. In contrast to the situation when the ion concentration in reservoir is 0.1M, the height of the first Na^+ peak near the quartz surface increases only ~10% as the brine film thickness

decreases from $h = \infty$ to 0.90 and 0.72nm. This is expected. At a bulk ion concentration of 1.0M, the Debye length is ~0.3nm and thus most of the charge on the quartz surface is screened by the Na^+ ions adsorbed on it (i.e. within the first Na^+ peak). Consequently, the height of the first Na^+ peak near a quartz surface is controlled mainly by the surface charge density and shows no great variation as a brine film is thinned.

5.3.3 Disjoining pressure in brine films

The disjoining pressure in thin films is measured as the pressure difference between the top and bottom pistons in Fig. 5-1a. For films in contact with charged quartz substrates (σ=–0.12C/m^2), film thickness of 0.92±0.02nm and 0.72±0.02nm and a brine reservoir ion concentration of 0.1M and 1M are studied. Figure 5-9 shows the disjoining pressure of the films as a function of film thickness at two ion concentrations. For brine films with a thickness of ~0.92nm, the disjoining pressure increases from 2.45 to 3.57MPa as the brine concentration decreases from 1M to 0.1M. Similar increase, from 11.3 to 13.1MPa, is observed in brine films with a thickness of ~0.72nm. The increased repulsion between oil and quartz surfaces at lower salinity is consistent with the double-layer expansion mechanism for wettability alteration in OBR systems.[232, 246]

To understand the above results more quantitatively, we note that the total disjoining pressure Π is usually split into the van der Waals component Π_{vdw}, the double layer component Π_{edl}, and the hydration component Π_{hdr}. For nanometer-thin films considered here, Π_{vdw} is typically much smaller than the other two components and thus is not discussed further. Using the PB equation adopted in the classical DLVO theory and the model of brine film sketched in Fig. 5-5c, Π_{edl} can be obtained through the contact value theorem[239]

$$\Pi_{edl}(H) = k_B T\left(\sum_i \rho_i(z = H) - \sum_i \rho_{i,\infty}\right), \quad (5.5)$$

where $\rho_i(z = H)$ is number density of ion *i* on the neutral surface located at $z = H$ in Fig. 5-5c's inset, $\rho_{i,\infty}$ is the ion density in brine reservoirs, and $k_B T$ is the thermal energy. $\rho_i(z = H)$ can be obtained by solving the classical PB equation.

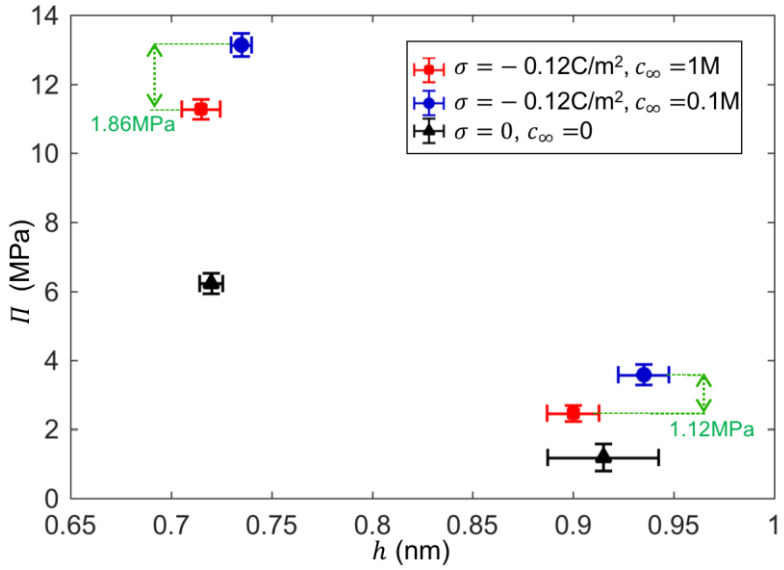

Figure 5-9. *Disjoining pressure in thin films.* The disjoining pressure is shown with different thickness, quartz surface charge density, and reservoir ion concentration.

Solving Equ. 5.5 and the PB equation with a quartz surface charge density of –0.12C/m^2, Π_{edl} in a 0.92±0.02nm-thick brine film is determined as 1.26 and 0.02 MPa at a brine concentration of 0.1 and 1M; in a 0.72±0.02nm-thick brine films, Π_{edl} is 2.21 and 0.31 MPa at a brine concentration of 0.1 and 1M. The increase of Π_{edl} at each brine film thickness due to the salinity reduction predicted by the PB equation agrees very well with the MD results. Such a good agreement is somewhat fortuitous but not a coincidence. Indeed, PB equation has also been shown to predict Π_{edl} in nanometer-thick brine films separating moderately charged soft surfaces quite well.[369] The good performance of the PB equation originates from the facts that Π_{edl} in these films are dominated by the entropic effect associated with the enrichment of ions and the latter is captured by the PB equation.

At a bulk ion concentration of 1M, the observed Π should be contributed mostly by Π_{hdr} because Π_{edl} is greatly suppressed as shown in the PB predictions. In many theoretical models of disjoining pressure, Π_{hdr} and Π_{edl} are assumed to be additive, i.e. Π_{hdr} is independent of Π_{edl} (and hence the surface charge and ion concentration). This additivity has been shown to break down in thin films between rigid surfaces in early experiments[239] and in films between soft surfaces

in recent MD simulations.[369] Here, we examine to what extent Π_{hdr} in thin films separating a rigid quartz slab and a soft hydrocarbon liquid is affected by the quartz's surface charge. To this end, we studied the disjoining pressure in two water films (thickness: 0.72±0.02 and 0.92±0.02nm) in contact with neutral quartz surfaces.

Figure 5-9 shows that, when the quartz surface is neutral, the measured Π, which should be essentially Π_{hdr}, is 1.18 and 6.23 MPa in the 0.92nm- and 0.72nm-thick water films, respectively. In comparison, the Π at 1M ion concentration, which should also be dominated by Π_{hdr}, is 2.45 and 11.3 MPa in 0.90nm- and 0.72nm-thick brine films. These results indicate that Π_{hdr} increases as a quartz slab's surface charge density σ changes from 0 to –0.12C/m^2 and thus it is not simply additive with Π_{edl}. The rather different Π_{hdr} under different surface charge densities can be attributed to several reasons. First, when σ changes from 0 to –0.12C/m^2, a large number of Na^+ ions become adsorbed on the quartz surface. The hydration of these Na^+ ions is stronger than that of quartz surface because Na^+ ions are smaller than the silanol group. Therefore, water molecules are more difficult to be removed near the charged quartz surface than near the neutral surface, thus leading to a more repulsive Π_{hdr}. Second, when a quartz surface is electrified, the orientation of the interfacial water molecules and its evolution as the brine film is thinned, both of which affect the hydration force,[378-379] change too. For example, the dipole orientation of water molecules near a neutral quartz surface changes little as a water film is thinned from $h = \infty$ to to 0.92nm (see Fig. 5-10a), whereas that near a charged quartz surface (σ=–0.12C/m^2) changes notably as a brine film is thinned from $h = \infty$ to to 0.90nm (see Fig. 5-10b). The more noticeable change of the interfacial water molecules' orientation during the thinning of a brine film near charged quartz surface helps explain the stronger Π_{hdr} in these films.

Overall, in film as thin as ~0.9nm, the disjoining pressure is controlled by both the double layer forces and the hydration forces; as films are thinned to ~0.7nm, the hydration force dominates over the double layer force for ion concentration as low as 0.1M. The hydration force, however, is not

independent of the double layer force in that it changes as the quartz surface becomes electrified. When the brine salinity is lowered, the response of the disjoining pressure can be predicted quite well by the classical PB equation. This implies that the hydration force is less dependent on the salinity than the surface charge density of the quartz surface in the films studied here.

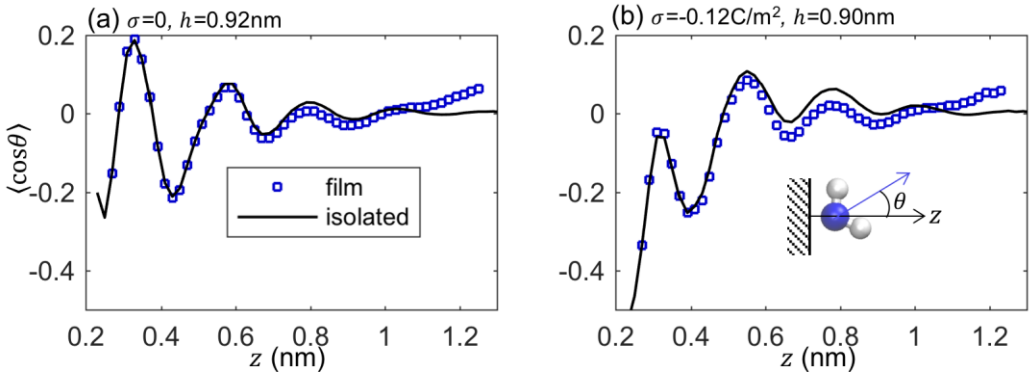

Figure 5-10. *Water dipole orientation profiles*. Dipole orientation of water molecules near isolated quartz surfaces and in thin films when the quartz surface has a charge density of 0 **(a)** and –0.12C/m^2 **(b).** The dipole orientation at position where water density is less than 10% of its bulk value is not shown.

5.3.4 Dynamics of thin brine films

The oil-brine-rock interfaces are often subject to shearing in the lateral direction, e.g. when an oil slug moves through a pore under the action of a pressure gradient.[380-382] In available studies of such problems, the dynamic properties of brine films are taken as those of bulk brine and a no-slip boundary condition is assumed at the oil-brine interface due to the limited information on these aspects. In this section, we fill this gap by studying the hydrodynamic properties of thin brine films. Without losing generality, we focus on the brine films with a reservoir concentration of 0.1M.

We first study the shearing of a reference system featuring thick slabs of brine and oil (Fig. 5-1c). Here, the brine-rock and the brine-oil interfaces are practically isolated because of their large separation. Shearing is imposed by pulling the top piston in the x-direction with a constant speed at V_p (V_p is 70m/s here; simulations with V_p=50m/s showed the same hydrodynamic properties within statistical error). After a steady state is reached, the velocity of water and decane is collected on-the-fly for 50ns. Figure 5-11a and 5-11b show that, away from the quartz-water and water-oil

interfaces, the velocity profiles of water and decane are linear. The velocity of water is almost zero within the first water density peak (z<0.47nm), consistent with the notion that water molecules are attracted strongly to the quartz surfaces.[303] Across the nominal brine-oil interface (z=4.07nm), there is a velocity jump, signifying an slip between the brine and oil phases. Similar interfacial slip has been identified in studies on weakly interacting fluids and was found to originate from the poor mixing of the two fluid phases across diffuse fluid-fluid interface and/or the limited entanglement of molecular chains of the species from the two fluids.[383-385]

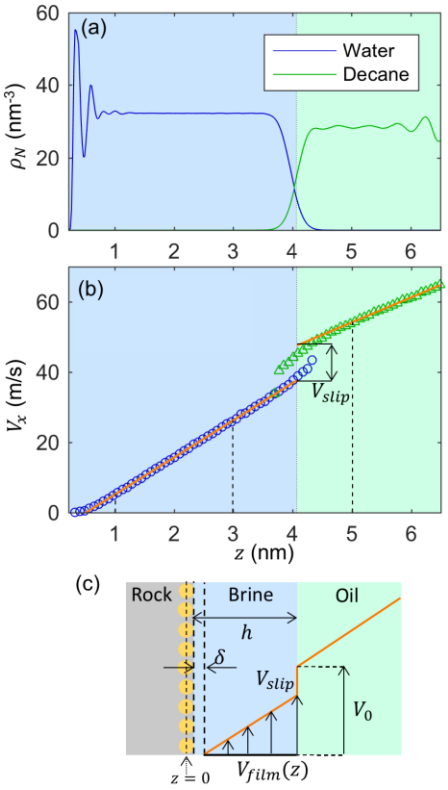

Figure 5-11. *Shear flow near quartz-brine and brine-oil interfaces.* **(a)** The number density profiles of water and decane's carbon atoms near the quartz surface in a *reference system* (see Fig. 5-1c). **(b)** The velocity profiles of water and decane. The shear flow is induced by pulling the top piston in Fig. 5-1c at a constant speed of 70m/s. **(c)** A schematic of the continuum model for describing the shearing flow in brine films.

In light of the above observations, we use a continuum model to describe the hydrodynamics of oil-brine-rock interfaces (see Fig. 5-11c). First, a no-slip plane is located at a distance δ from the brine-rock interface (note that the brine-rock interface is located 0.22nm above the zero plane

of the quartz surface, see Fig. 5-2a). Second, a slip occurs at the brine-oil interface with $V_{slip} = \tau/\beta$, where V_{slip} is the difference of the brine and oil velocities extrapolated from their profiles in their respective phases to the nominal brine-oil interface, β is the interfacial slip coefficient,[384, 386-387] and τ is the shear stress at the brine-oil interface. Finally, the Stokes equation with a constant effective viscosity ($\mu_{e,w}$ and $\mu_{e,d}$ for the brine and oil) is used to describe the flow in the brine and oil slabs. $\mu_{e,d}$ is taken as the bulk value of decane because the oil slab is thick. Using this model and the velocity profiles in MD simulations, δ, β, and $\mu_{e,w}$ can be obtained (see *Appendix D*). From the data shown in Fig. 5-11b, δ is determined as 0.29nm and β is found to be 0.39 ± 0.04 MPa·s/m. $\mu_{e,w}$ is determined to be 0.39 mPa·s, which is practically the same as that of bulk water.

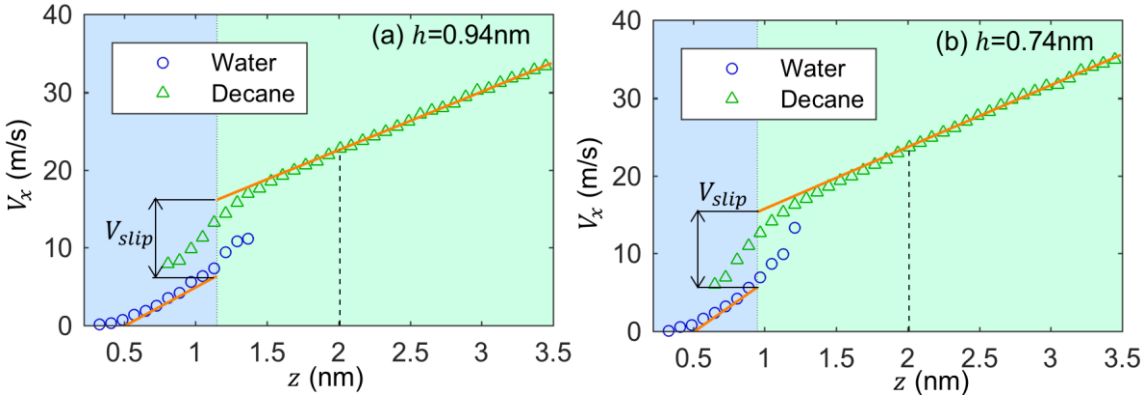

Figure 5-12. *Shear flow in molecularly thin brine films.* Velocity profiles of water and oil across brine films with a thickness of 0.94nm **(a)** and 0.74nm **(b)**. The shear flow is induced by pulling the top piston in Fig. 5-1b at a constant speed of 40m/s.

We next simulated the shearing of oil-brine-rock interfaces in thin brine films. Figure 5-12a and 5-12b show that velocity profiles in brine films with a thickness of 0.74 and 0.94nm, respectively. Their key features, i.e. shift of the no-slip boundary away from the quartz surface and interfacial slip, are similar to those in Fig. 5-11b. The continuum model in Fig. 5-11c is also applied in these brine films with $\mu_{e,w}$ and β as adjustable parameters and $\mu_{e,d}$ taken as bulk oil viscosity (0.63mPa·s). The no-slip plane near the quartz surface is assumed to remain at the same position as in the reference system (i.e. z=0.51nm, or equivalently, δ=0.29nm) since water-rock interfaces

in thin brine films differ little from those in the reference system (see Fig. 5-4). By requiring that V_{slip} at the brine-oil interface and the total water flux across the brine film predicted by the continuum model to match those measured in MD simulations, $\mu_{e,w}$ and β in the brine films are extracted (see Table 5-2). The effectivity viscosity of water in the two brine films are the same as that of bulk water within statistical uncertainty. While the friction coefficient β at the brine-oil interfaces seems to increase marginally as a brine film is thinned, the variations are within the statistical error of our simulations. These results suggest that the hydrodynamic properties of brine films are not heavily affected by the molecular confinement in these films, which is consistent with the insensitivity of the structure of water in brine films and brine-oil interfaces toward brine films' thickness (see Section 5.3.1).

Table 5-2. *Effective water viscosity and brine-oil slip coefficient for brine films**

Film thickness (h / nm)	0.94	0.94	0.74	0.74	4.00
Piston speed (m/s)	40	20	40	20	70
$\boldsymbol{\mu_{e,w}}$ (mPa·s)	0.40±0.05	0.37±0.02	0.33±0.03	0.32±0.01	0.39±0.04
$\boldsymbol{\beta}$ (MPa·s/m)	0.41±0.04	0.40±0.08	0.46±0.03	0.44±0.05	0.39±0.04

* the ion concentration in the brine reservoir is 0.1M.

For oil slugs inside a pore, the brine films between the slug and pore walls act like a slip layer facilitating the transport of the oil slug due to their smaller viscosity than oil.[388] For a brine film with a thickness h and under a shear stress τ, the velocity of the oil at the brine-oil interface is $V_0/\tau = h/\mu_b$ according to the classical hydrodynamic models (μ_b is the viscosity of bulk water). In light of the continuum model sketched in Fig. 5-11c, the velocity of the oil at the interface $V_0'/\tau = (h-\delta)\mu_{e,w}^{-1} + \beta^{-1}$, or

$$V_0'/V_0 = (1-\delta/h)\mu_b\mu_{e,w}^{-1} + \mu_b/\beta h. \quad (5.6)$$

The first term on the right-hand side accounts for the effects of the shifted shear plane from quartz surfaces and deviation of viscosity from their bulk values. The second term on the right-hand side accounts for the slip at brine-oil interfaces. For the 0.74 and 0.94nm-thick films considered here, the first term is ~0.75-0.85 based on the data in Table 5-2, suggesting that these effects only change

the transport of oil slugs marginally. The second term is ~1 for the two films considered here. In another word, because of the interfacial slip, the oil surface can move ~100% faster than when this slip is neglected. Physically, in terms of providing lubrication for the movement of an oil slug along a pore, the slip at the brine-oil interface effectively increases the apparent thickness of the brine layer between the oil slug and pore walls by $\ell = \mu_b/\beta$. When ℓ is comparable to the physical thickness h of the brine film, the interfacial slip greatly affects the transport of the oil slug. Because brine films in OBR systems are often thinner than one or a few nanometers,[234-235] such interfacial slip should be considered in future continuum simulations of oil droplet transport in OBR systems.

5.4 Conclusion

In summary, we studied molecularly thin brine films confined between nonpolar oil and quartz surfaces using MD simulations. We quantify the structure of the interfacial water, oil, and EDLs, the disjoining pressure, and the shearing properties of the brine films and brine-oil interfaces. The sub-nanometer confinement in brine films only weakly modifies the molecular packing at the rock-brine and brine-oil interfaces. Increasing the confinement (i.e. thinning the brine films), however, markedly increases the counterion density near the charged quartz surfaces, especially under low brine concentration conditions. Although the increased geometrical confinement does contribute *directly* to the enhanced counterion adsorption, its *indirect* contributions are more important, e.g. as the confinement is increased, the dielectric screening in brine films is weakened. The disjoining pressure in the films is dominated by the hydration forces. Interestingly, the disjoining pressure increases as the brine concentration is lowered and the magnitude of its increase is consistent with that predicted by the PB equation. Analysis of the disjoining pressure in systems with neutral and charged quartz surfaces indicates that the hydration disjoining pressure increases markedly as the quartz surface is electrified. Hence the hydration and double layer forces are not simply additive, which is consistent with prior experimental measurement between solid surfaces and simulation

of surface forces between soft surfaces.[239, 369] The first layer of water molecules on the quartz surface are effectively stagnant but the viscosity of water beyond this layer is bulk-like in brine films as thin as three water molecule layers. A notable interfacial slip is observed between the brine and oil phase, which contributes to an effective slip length of ℓ~1nm in the systems investigated here.

The results and insights here help improve the fundamental understanding, numerical modeling, and rational application of technologies including LSW. The little disturbed structure and dynamic properties of interfacial water and oil as the brine films are thinned highlight that the water-rock and water-oil interfaces can be predicted reasonably well from unconfined water-rock and water-oil interfaces. The classical PB equation predicts quite well the response of the disjoining pressure to salinity change for the cases studied here. However, the fact that hydration forces is most likely not additive to the double layer force suggests that the classical surface force theories should be used with caution in modeling of disjoining pressure in brine films in OBR systems. Furthermore, the significant modification of EDL structure and the decrease of the effective dielectric constant as brine films are thinned will likely affect processes such as surface charge regulation.[389] Therefore, although these factors do not greatly change the disjoining pressure under the fixed surface charge condition explored here, they may play an important role in practice. Finally, the slip at brine-oil interfaces can greatly facilitate the transport of oil slugs in narrow pores by *effectively* providing a thicker slip layer for such transport.

Supporting Information

All supporting information cited in this chapter is located in *Appendix D*.

Chapter 6. Conclusions

Multiphase interfacial and transport phenomena play a central role in the extraction processes of hydrocarbons from conventional reservoirs and unconventional sources such as shales. Hence there is a long-standing need to understand these phenomena, especially at the pore scale. In this dissertation, three projects were performed to understand these phenomena in hydrocarbon reservoirs: the imbibition of water in shales, transport of gaseous and liquid hydrocarbon transport in shales, and the interfacial thermodynamics and dynamics of thin brine films in oil-brine-rock systems.

In Chapter 2, the imbibition of water into single mica nanopore initially filled with methane at pressure similar to that in shale gas reservoirs is investigated. Water is imbibed into the nanopore through surface hydration in the form of monolayer liquid films till the imbibition fronts reach the pore's end. As the imbibition front moves, the water film behind it gradually densifies and later becomes saturated. The propagation of the imbibition fronts follows a diffusive scaling law with an effective diffusion coefficient more than ten times larger than the diffusion coefficient of water molecules in the water film adsorbed on mica walls. The scaling law can be captured through a thin film growth theory, where the stronger water-mica interaction over water-water interaction gives rise to the fast diffusion front. After the imbibition fronts meet at the middle of the pore end, the second stage of imbibition starts. Due to capillary effects, the corners of the pore are occupied by water molecules first and the films on the pore surface are growing with extra water layers that are added from pore interior to pore entrance.

In Chapter 3, the invasion of methane gas into water-filled mica pores with widths of 2-6nm is studied. A residual thin water film is left on the pore surface as the gas front meniscus moving into the pore at high pressures. The thickness of such film is less than 1nm in these pores and decreases with pore width. The gas breakthrough pressure can be predicted using the capillary pressured with effective pore width modified by the finite thickness of the thin water film in 4 and 6nm-wide

pores. In 2nm-wide pores, the breakthrough pressure is underestimated by such capillary pressure and the diffuseness of the gas-liquid interface should be taken into account. The dynamics of gas invasion is quantified through the movement of the front of liquid meniscus. Once the negative slip length on mica surface is considered, the front dynamics can be predicted well by classical hydrodynamics.

In Chapter 4, the free energy profiles of nanometer-sized droplets entering a nanopore under varying pressure difference are studied using molecular and continuum simulations. Three regimes of droplet invasion are identified: spontaneous invasion, invasion by thermal activation, and blocking at pore entrance. Due to the disjoining pressure of thin liquid films between droplet and pore surface, a free energy barrier higher than that predicted by classical capillary theories must be overcome. When the droplet size is in nanometers and comparable to the pore width, the parameter space in which invasion can occur is expanded by thermal activation. When the droplet is slightly narrower than a pore, rather than entering the pore freely, large free energy barrier for droplet entry still exists because of the disjoining pressure effects. Hydrodynamic drag on the droplet is insufficient to drive the droplet into the pore. Nevertheless, a droplet can enter the pore through Brownian motion, though its mean entry time increases sharply with droplet diameter for a given pore size.

In Chapter 5, brine films confined between model oil and rock are investigated, with a focus on the structure of the brine films and the EDLs in them, the surface forces between oil and rock, and the dynamic properties of brine films and their interfaces. As brine films are squeezed down to ~0.7nm, the structure of water-rock and water-oil interfaces changes marginally, except that the oil surface above the brine film becomes less diffuse. As the film is thinned from ~1.0 to ~0.7nm, ions are enriched (depleted) near the rock (oil) surface, especially at a bath ion concentration of 0.1M. These changes are caused primarily by the reduced dielectric screening of water and the weakened ion hydration near water-oil interfaces, and, to a much smaller extent, the increased

confinement. When the brine film is ~1.0nm thin, the disjoining pressure between the charged rock and the oil is contributed by hydration and EDL forces. The latter is reduced greatly as the ion concentration increases from 0.1 to 1.0M, and magnitude of the reduction is close to that predicted by the DLVO theory. When the brine film is thinned from ~1.0 to ~0.7nm, the disjoining pressure increases by ~10MPa, mostly due to an increase of hydration forces. Whereas the first layer of water molecules on the rock surface is hydrodynamically stagnant, even in brine films of 0.7nm thickness, the viscosity of the water beyond the first layer is bulk-like and the slip coefficient of the oil-water interfaces is close to that between thick oil and water layers.

Together this dissertation reveals the crucial role of thin liquid films in determining the thermodynamics and hydrodynamics of multiphase transport at the pore scale, in conventional and unconventional hydrocarbon reservoirs. These liquid films emerge spontaneously between gas/liquid-phase hydrocarbons and strongly hydrophilic solid surfaces, the latter being ubiquitous in shales and convectional oil reservoirs. Because these films often measure less than a few nanometers in thickness, experimental characterization and continuum simulations of these films have long been difficult. These difficulties are circumvented using molecular dynamics simulations in this dissertation, and the molecular insight gained here helps lay foundation for effectively modeling, manipulating, and leveraging these thin liquid films to enhance oi/gas production and to reduce potential environmental damage during oil and gas extraction.

Appendices

Appendix A

AA. Schematic of the simulation system for studying water imbibition

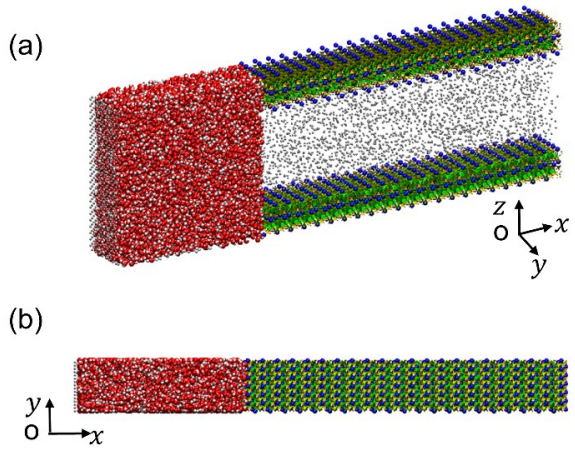

Figure SA-1. *Schematics of the MD system used in Fig. 2-1 in the main text.* **(a)** A 3D view of the MD system. **(b)** An *xy*-plane view of the system.

AB. Equilibrium MD simulations for characterizing hydration layers of mica surfaces

To understand the dynamics of water molecules in the hydration layer on mica surfaces, we performed separate equilibrium MD simulations. The MD system in these simulations features two mica walls separated by a slab of methane measuring 6nm in thickness. The dimension of the mica walls is 3.67 and 3.15nm in the *x*- and *y*- direction, respectively. The system is periodical in the *xy*-plane, and its center is located at (0, 0, 0). A layer of water molecules is placed on each wall so that the water area density matches the asymptotic density of the water molecules in the *monolayer* water film on pore walls shown in Fig. 2-3b. The system is equilibrated for 2ns, which is followed by a 5ns equilibrium run. The mean square displacements of water molecules in the *x*- and *y*-directions are used to determine their diffusion coefficients, e.g., the self-diffusion coefficient in the *x*-direction, D_x, is computed using the Einstein relation $D_x = \lim_{t\to\infty}\langle|x_i(t) - x_i(0)|^2\rangle/2t$, where x_i is the *x*-position of water molecule i and t is the time. To compute the PMF of water molecules

on the mica surface, the average density of the water molecules in the *xy*-plane, $\rho_s(x,y)$, is first computed by binning their positions during the equilibrium run. The PMF is next computed using $\mathrm{PMF}(x,y) = -k_B T \ln(\rho_s(x,y)/\rho_0)$, where ρ_0 is the average water density in the monolayer water film.

AC. System used for calculating potential energy of water molecules

As described in the main text, to qualitatively understand $E_{\downarrow}$ and $W_{\leftarrow}$, the potential energy of water molecules at four different positions in water-mica systems are calculated (see Fig. SA-2):

1. In bulk water. The potential energy of the water molecule is denoted as E_1
2. In the first water layer near a mica wall hydrated by a thick slab of water (slab thickness: ~6nm). The potential energy of the water molecule is denoted as E_2.
3. In the monolayer water film adsorbed on a mica surface. The water film is exposed to methane (pressure: 250bar). The potential energy of the water molecule is denoted by E_3.
4. Isolated water molecules on a mica surface. The potential energy of the water molecule is denoted as E_4. In this simulation, eight water molecules are placed on a mica surface measuring 3.7×3.15nm^2 laterally so that water-water interactions are very weak. Periodical boundary condition is adopted in directions parallel to the mica surface.

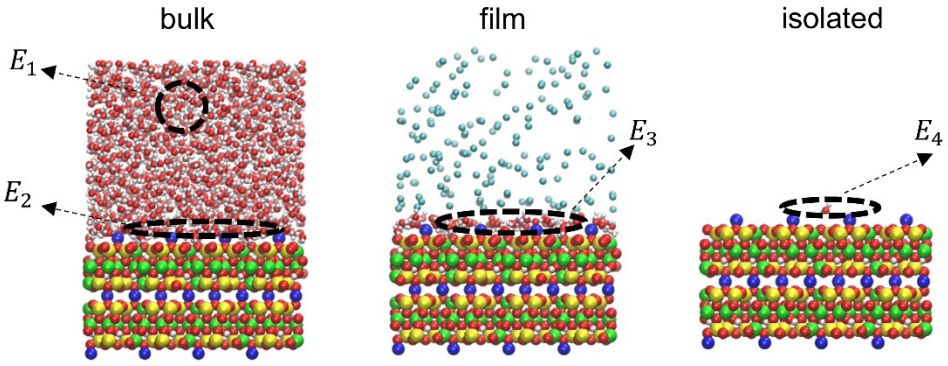

Figure SA-2. *Schematics of the MD system used for studying the potential energy of water molecules in various water-mica systems.* In the middle panel, the cyan balls denote methane molecules.

AD. Radial density distribution around water molecules

In the main text, to understand why it is energetically favorable for a water molecule at the imbibition front to hop forward, we compute the potential energy of a single water molecule in two scenarios: when it resides in a monolayer water film adsorbed on mica surface (E_3, middle panel in Fig. SA-2) or when it is isolated on a mica surface (E_4, right panel in Fig. SA-2). It was found that E_4 is lower than E_3 by $3k_BT$. To understand this result, we compute the distribution of mica surface atoms around a water molecule in these two scenarios. Since water molecules often interact strongly with the bridging oxygen atoms with tetrahedral substitution (OBST) on mica surfaces, we compare the distribution of OBST atoms around water molecules in the above two scenarios. Figure SA-3 shows that, compared to the water molecules in a monolayer film, water molecules isolated on mica surface are coordinated by more OBST atoms. Since OBST atoms interact with water molecules via attractive electrostatic interactions, this result helps explain why the potential energy of a water molecule is lower when it is isolated on a mica surface.

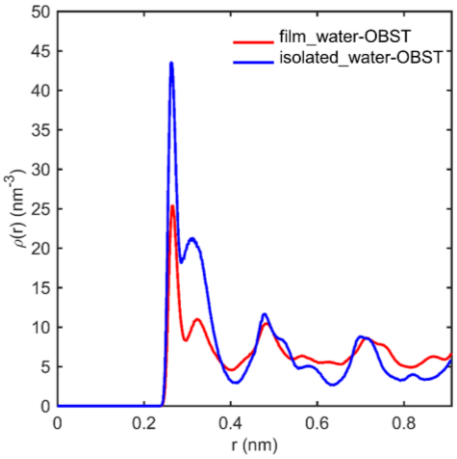

Figure SA-3. *Radial density distribution of OBST atoms of mica near water molecules in a monolayer water film adsorbed on mica surface and isolated on mica surfaces.* OBST atoms are the bridging oxygen atoms with tetrahedral substitution in mica.

Disclosure

This work has been published by the Royal Society Chemistry: C. Fang, R. Qiao, Surface hydration drives rapid water imbibition into strongly hydrophilic nanopores. *Phys. Chem. Chem. Phys.* 2017, 19 (31), 20506-20512.

Appendix B

BA. Force fields parameters.

BA.1 Non-bonded parameters

(The combination rule for dissimilar atoms is $\sigma_{ij} = (\sigma_i + \sigma_j)/2$ and $\epsilon_{ij} = \sqrt{\epsilon_i \epsilon_j}$.)

Table SB-1. *Non-bonded parameters*

Atom type	Atom name	Charge (e)	σ_i (nm)	ϵ_i (kJ/mol)
Tetrahedral aluminum	ALT	1.575	3.30203e-1	7.70070e-6
Octahedral aluminum	AL	1.575	4.27124e-1	5.56390e-6
Tetrahedral silicon	SI	2.100	3.30203e-1	7.70070e-6
Potassium ion	K	1.000	3.33401e-1	4.18400e-1
Bridging oxygen	O	-1.05	3.16554e-1	6.50194e-1
Bridging oxygen with tetrahedral substitution	OBS	1.16875	3.16554e-1	6.50194e-1
Hydroxyl oxygen	OH	-0.95	3.16554e-1	6.50194e-1
Hydroxyl hydrogen	H	0.425	0.0	0.0
Water hydrogen	HW	0.4238	0.0	0.0
Water oxygen	OW	-0.8476	3.16554e-1	6.50200e-1
Methane molecule	C4	0.0	3.73000e-1	1.23054e+0
Piston carbon	CA	0.0	3.55000e-1	2.93000e-1

BA.2 Bonded parameters

The bond and angle of water molecule is fixed using SELLTE algorithm with OW-HW bond length 0.1nm and HW-OW-HW angle 109.5^o.

BB. The thickness of the water films in 4 nm pores for P_u =60MPa and P_u =100MPa.

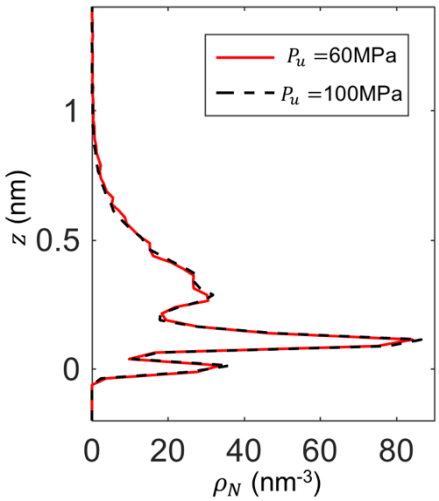

Figure SB-1. *Density profile of water molecules near the lower the mica wall in the 4nm-wide channel connected to upstream reservoirs with pressure of 60 and 100MPa.*

Disclosure

This work has been published by the Institute of Physics: C. Fang, F. Zhang, R. Qiao, Invasion of gas into mica nanopores: a molecular dynamics study. *J. Phys. Condens. Matter* 2018, 30 (22), 224001.

Appendix C

CA. Calculation of free energy profile for droplet invasion by continuum theory

CA.1 Droplet invasion in two-dimensional spaces

Figure SC-1 shows the schematics of a droplet invading a pore. The invasion is divided into three stages depending on the extent that droplet invaded into the pore. At stage I, the droplet only invades slightly into the pore from the position where it just touches the two edges of the pore's entrance. The front and back part of the droplet have a circular shape with a radius r_f and r_b, respectively (see Fig. SC-1a). At this stage, the angles shown in Fig.SC-1a are within the range of $\pi/2 \geq \theta_f \geq \theta_b \geq \theta_0$, where $\sin\theta_0 = W_{eff}/2R_0$ and R_0 is the radius of the un-deformed droplet. In this and the following stages, the changes of the droplet's interface area ΔA and invasion volume ΔV_{in} are measured with respect to the initial un-deformed droplet with a radius of R_0 and an angle of θ_0.

Initially, when the droplet just touches the two edges of the pore entrance, $\theta_f = \theta_b = \theta_0$ and $r_f = r_b = R_0$. The geometric constraint requires

$$W_{eff}/2 = r_f \sin\theta_f = r_b \sin\theta_b \quad (\text{SC. 1})$$

The constraint due to the conservation of the droplet volume is

$$\pi R_0^2 = (\pi - \theta_b) r_b^2 + \theta_f r_f^2 + W_{eff}^2 (cot\,\theta_b - cot\,\theta_f)/4 \quad (\text{SC. 2})$$

The increase of water-droplet interface area is

$$\Delta A = 2(\pi - \theta_b) r_b + 2\theta_f r_f - 2\pi R_0 \quad (\text{SC. 3})$$

The change of the invasion volume is

$$\Delta V_{in} = \theta_f r_f^2 - W_{eff} r_f \cos\theta_f /2 - (\theta_0 R_0^2 - W_{eff} R_0 \cos\theta_0 /2) \quad (\text{SC. 4})$$

The steps of calculating the free energy profiles in this stage are as follows: (1) Vary θ_f from θ_0 to $\pi/2$ and obtain r_f from the geometric constraint; (2) Obtain θ_b and r_b from the geometric and volume constrains together. (3) Calculate the free energy at each point by inserting θ_f, r_f, θ_b, and r_b into equations SC.3 and SC.4.

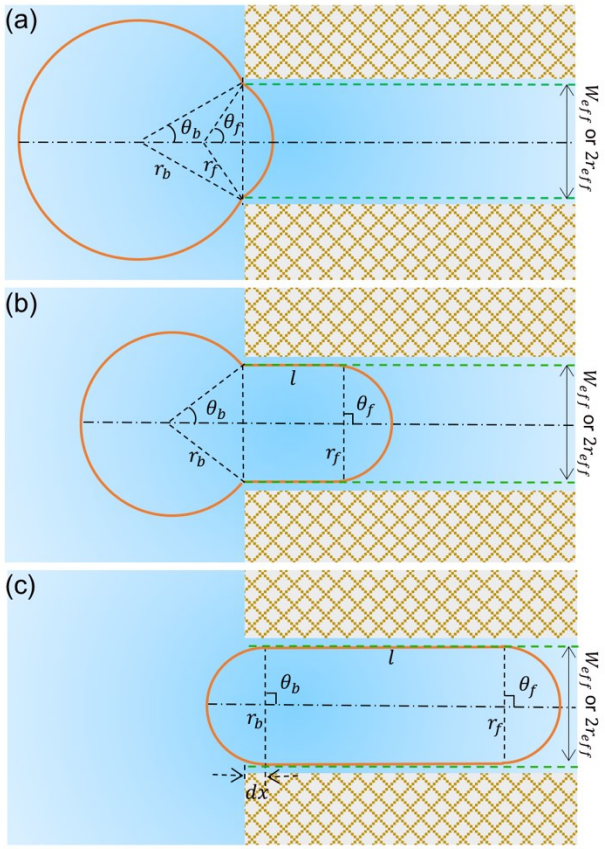

Figure SC-1. *Schematics of the three stages of droplet invasion process.* **(a)** stage I, **(b)** stage II, and **(c)** stage III. The solid line denotes the boundary of the droplet. The front and back parts of the droplet have a circular shape with a radius of r_f and r_b, respectively. The pore is either a slit pore with effective width of W_{eff} or a circular pore with an effective diameter of $2 \times r_{eff}$.

At stage II, thin water films begin to develop with length of l and the front part of the droplet maintains a constant radius of $r_f = W_{eff}/2$. The angles shown in Fig.SC-1b are within the range of $\pi/2 = \theta_f \geq \theta_b$. The geometric constraint requires

$$W_{eff}/2 = r_b \sin\theta_b \qquad (\text{SC. } 5)$$

The constraint due to the conservation of the droplet volume is

$$\pi R_0^2 = (\pi - \theta_b) r_b^2 + \theta_f r_f^2 + W^2 \cot\theta_b /4 + W_{eff} l \qquad (\text{SC. } 6)$$

The change of the water-droplet interface area is

$$\Delta A = 2(\pi - \theta_b) r_b + 2\theta_f r_f + 2l - 2\pi R_0 \qquad (\text{SC. } 7)$$

The change of the invasion volume is

$$\Delta V_{in} = \theta_f r_f^2 + W_{eff} l - (\theta_0 R_0^2 - W_{eff} R_0 \cos\theta_0 /2) \quad \text{(SC. 8)}$$

The free energy profiles can be calculated in a similar way by varying θ_b from the value at the end of stage I to $\pi/2$, and obtain r_b and l from the geometric and volume constraints.

At stage III, the radius of the back part of the droplet is reduced to $r_b = W_{eff}/2$ such that the droplet is no longer pinned at the two edges of the pore entrance. The angles shown in Fig. SC-1c are within the range of $\pi/2 = \theta_f = \theta_b$. The droplet moves into the pore as a rigid body. The interface area change is zero during this stage and the invasion volume with respect to the last moment in stage II is $W_{eff} dx$, where dx is the displacement of droplet in the *x*-direction in this stage. The free energy in this stage consequently decreases by $W_{eff} dx$ during invasion and the profiles are calculated by varying the value of dx.

CA.2 Mapping the free energy profile into center-of-mass position in 2D system

In the main text, the free energy profiles obtained in MD simulation are based on the reaction coordinate of the center-of-mass of the droplet with respect to the pore entrance. The free energy profiles calculated in Section C1.1 are given as functions of the volume droplet invaded into the pore (invasion volume). To compare these profiles, the invasion volume-based free energy profiles are transferred to the center-of-mass position based reaction coordinate. This can be done by calculating the center of mass position of the droplet in above three stages.

At stage I ($\pi/2 \geq \theta_f \geq \theta_b \geq \theta_0$), the droplet consists of three parts: the back and front partial circles and the remaining middle part (see Fig. SC-1a). The center-of-mass position and the volume of the back partial circle are

$$\bar{x}_1 = -2r_b \frac{\sin(\pi-\theta_b)}{3(\pi-\theta_b)} - r_b \cos\theta_b \text{ and } V_1 = (\pi - \theta_b) r_b^2 \quad \text{(SC. 9)}$$

The center-of-mass position and the volume of the front partial circle are

$$\bar{x}_3 = 2r_f \frac{\sin\theta_f}{3\theta_f} - r_f \cos\theta_f \text{ and } V_3 = \theta_f r_f^2 \quad \text{(SC. 10)}$$

Likewise, for the remaining middle part we have

$$\bar{x}_2 = \left(\frac{2}{3}(d_1+d_2)^2 - d_2\left(\frac{2}{3}d_2 + d_1\right)\right)/d_1 - r_b\cos\theta_b \text{ and } V_2 = \frac{1}{2}W_{eff}\left(r_b\cos\theta_b - r_f\cos\theta_f\right) \quad \text{(SC. 11)}$$

where $d_1 = r_b\cos\theta_b - r_f\cos\theta_f$ and $d_2 = r_f\cos\theta_f$.

The center of mass position of the droplet at stage I is thus given by $\bar{x} = \sum \bar{x}_i V_i / \sum V_i$.

At stage II ($\pi/2 = \theta_f \geq \theta_b$ and $r_f = W_{eff}/2$), the droplet consists of four parts: the front and back partial circles, the left triangle, and the right rectangle (see Fig. SC-1b). The center-of-mass of the whole droplet is obtained in a manner similar to that at stage I. Specifically, the center-of-mass position and the volume of the back partial circle are

$$\bar{x}_1 = -2r_b\frac{\sin(\pi-\theta_b)}{3(\pi-\theta_b)} - r_b\cos\theta_b \text{ and } V_1 = (\pi-\theta_b)r_b^2 \quad \text{(SC. 12)}$$

For the front partial circle, we have

$$\bar{x}_4 = 2r_f\frac{\sin\theta_f}{3\theta_f} + l \text{ and } V_4 = \theta_f r_f^2 \quad \text{(SC. 13)}$$

For the left triangle, we have

$$\bar{x}_2 = -\frac{1}{3}r_b\cos\theta_b \text{ and } V_2 = \frac{1}{2}r_b W_{eff}\cos\theta_b \quad \text{(SC. 14)}$$

For the right triangle, we have

$$\bar{x}_3 = l/2 \text{ and } V_3 = W_{eff}l \quad \text{(SC. 15)}$$

At stage III ($\theta_f = \theta_b = \pi/2$), the center-of-mass of the droplet can be computed using the position of its back circle with respect to the pore entrance (labeled as dx in Fig. SC-1c).

CA.3 Droplet invasion in three-dimensional spaces

Here, an initially spherical droplet with a radius R_0 invades into a cylindrical pore with an effective radius r_{eff}. The free energy profile for the droplet invasion in this 3D system is similar to the droplet invasion in 2D system detailed in Section C1.1. We again divide the invasion process into three stages as shown in Fig. SC-1.

At stage I, the droplet is split into a spherical sector with a radius r_b and a half cone angle

$\pi - \theta_b$, a cone with a radius r_{eff} and a half angle θ_b, and a spherical cap with a base radius r_{eff} and a spherical radius r_f. At this stage, the angles shown in Fig. SC-1a are within the range of $\pi/2 \geq \theta_f \geq \theta_b \geq \theta_0$, where $\sin\theta_0 = r_{eff}/R_0$. Initially, when the droplet just touches the two edges of the pore entrance, we have $\theta_f = \theta_b = \theta_0$ and $r_f = r_b = R_0$. In this and the following stages, the changes of water droplet interface area ΔA and invasion volume ΔV_{in} are again measured with respect to the initial un-deformed droplet with a radius of R_0 and an angle of θ_0. The geometric constraint requires

$$r_{eff} = r_f \sin\theta_f = r_b \sin\theta_b \qquad \text{(SC. 16)}$$

The constraint due to the conservation of the droplet volume is

$$\frac{4}{3}\pi R_0^3 = \frac{2}{3}\pi r_b^3(1+\cos\theta_b) + \frac{\pi}{3}r_{eff}^2 r_b \cos\theta_b + \frac{\pi}{6}r_f(1-\cos\theta_f)[3r_{eff}^2 + r_f^2(1-\cos\theta_f)^2] \qquad \text{(SC. 17)}$$

The change of water-droplet interface area is

$$\Delta A = 2\pi r_b^2(1+\cos\theta_b) + 2\pi r_f^2(1-\cos\theta_f) - 4\pi R_0^2 \qquad \text{(SC. 18)}$$

The invasion volume with respect to the droplet's initial position is

$$\Delta V_{in} = \frac{\pi}{6}r_f(1-\cos\theta_f)[3r^2 + r_f^2(1-\cos\theta_f)^2] - \frac{\pi}{6}R_0(1-\cos\theta_0)[3r^2 + R_0^2(1-\cos\theta_0)^2] \qquad \text{(SC. 19)}$$

The free energy profiles in this stage are calculated by varying θ_f as stated in the case of the 2D droplet (see Section C1.1).

At stage II, thin water films begin to develop with a length of l and the front circular part of the droplet has a constant radius $r_f = r_{eff}$. The droplet now has one more part: a cylinder with a length l and a radius r_{eff}. The angles shown in Fig.SC-1b are within the range $\pi/2 = \theta_f \geq \theta_b$. The geometric constraint requires

$$r_{eff} = r_b \sin\theta_b \qquad \text{(SC. 20)}$$

The constraint due to the conservation of the droplet volume is

$$\frac{4}{3}\pi R_0^3 = \frac{2}{3}\pi r_b^3(1+\cos\theta_b) + \frac{\pi}{3}r_{eff}^2 r_b \cos\theta_b + \pi r_{eff}^2 l + \frac{2}{3}\pi r_{eff}^3 \qquad \text{(SC. 21)}$$

The change of the water-droplet interface area is

$$\Delta A = 2\pi r_b^2(1+\cos\theta_b) + 2\pi r l + 2\pi r_f^2(1-\cos\theta_f) - 4\pi R_0^2 \qquad \text{(SC. 22)}$$

The change of invasion volume is

$$\Delta V_{in} = \frac{\pi}{6} r_f (1 - \cos\theta_f)\left[3r_{eff}^2 + r_f^2 (1 - \cos\theta_f)^2\right] + \pi r^2 l - \frac{\pi}{6} R_0 (1 - \cos\theta_0)[3r^2 + R_0^2 (1 - \cos\theta_0)^2] \quad (\text{SC. } 23)$$

The free energy profiles in this stage are calculated by varying θ_b as stated in the case of the 2D droplet (see Section C1.1).

At stage III, the radius of back spherical sector is reduced to $r_b = r_{eff}$ such that the droplet is no longer pinned at the two edges of the pore entrance. The angles shown in Fig.SC-1c are $\pi/2 = \theta_f = \theta_b$. The droplet moves as a rigid body into the pore. The interface area change is zero within this stage and the invasion volume with respect to the last moment in stage II is $\pi r_{eff}^2 dx$, where dx is the displacement of droplet in *x* direction within this stage (see Fig. SC-1c). The free energy in this stage consequently decreases by $\pi r_{eff}^2 dx$ during the droplet invasion and the free energy profiles are calculated by varying the value of dx.

CB. System parameters used in MD simulations

Table SC-1. *The dimensions of the MD systems studied in this work.*

	Droplet diameter	Box size ($L_x \times L_y \times L_z$)	Length of the total vacuum space in Fig. 4-1b	Pore length; Pore width	Pressure on the left piston	Pressure on the right piston
Large droplet	6 nm	40 nm×3.93 nm ×11.69 nm	~9 nm	11.01 nm; 4 nm	27.1, 31.6, 33.6, and 38.1 MPa	0.1 MPa
Small droplet	1.84 nm 2.26 nm 2.60 nm	26nm×3.93nm ×7.68nm	~5 nm	11.01 nm; 4 nm	0.1 MPa (free energy calculation) 5.1 MPa (non-equilibrium run)	0.1 MPa

Finite-size effects. Our simulations focus on the thermodynamics (i.e., free energy profile) of a single droplet invading a narrow pore. The key source of finite-size effects is the finite size of the simulation box in the *z*-direction (see Fig. 4-1b and Fig. SC-2). Specifically, because the

periodic boundary condition is applied in this direction, a droplet can interact with its images. Finite-size effects can arise if the energy for these interactions is not greatly smaller than the free energy for droplet invasion. For a neutral droplet immersed in water, its interaction with its periodic images is weak if bulk-like water exists between a droplet and its images (see Fig. SC-2), or equivalently, the distance between their surfaces (ΔS) is much larger than the width of droplet-water interfaces (h_{int}). For the droplets considered in this work, h_{int} ~0.8nm. The smallest ΔS in all systems modeled is 5.08nm (when studying the invasion of a 2.60nm-diameter droplet into the 4nm-wide slit pore). Hence, finite-size effects should be minor in our simulations. As a side note, if we were to study the hydrodynamics of droplet invasion, then the simulation box size must be increased greatly because hydrodynamic interactions are long-ranged.

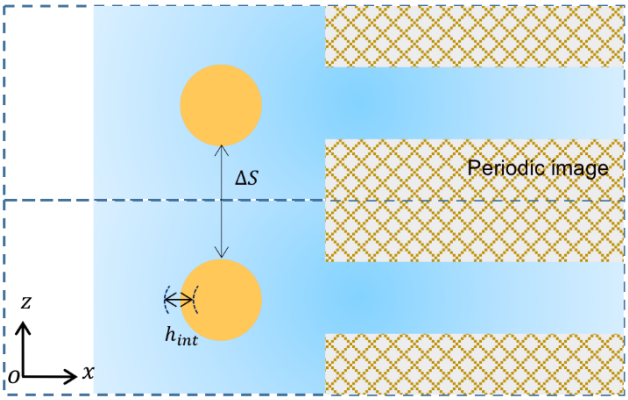

Figure SC-2. *A droplet and its periodic images in the z-direction.* The dashed box shows the simulation box in the *xz* plane. The distance between the surface of droplet and its periodic image is ΔS. The width of the droplet-water interface is h_{int}.

CC. Wetting properties of the quartz walls

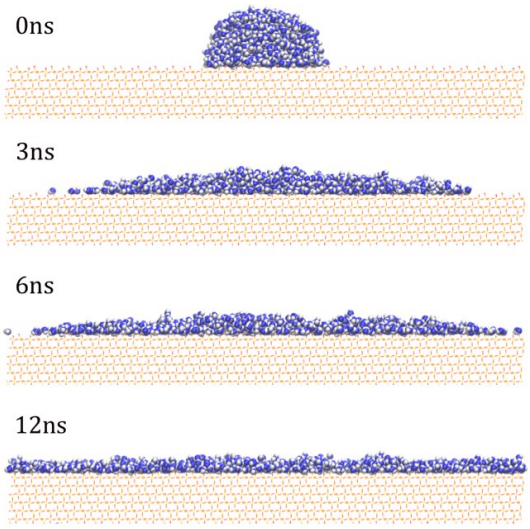

Figure SC-3. *Evolution of a water droplet placed on a quartz surface that is structurally identical to the slit pore walls used in simulations of droplet invasion.* A droplet consisting of 1000 water molecules is initially placed on the surface and the simulation is run for 20ns. The quartz wall is ~3nm thick and 20.64nm long. The depth of the system in the direction normal to the paper is 3.93nm.

CD. Histograms obtained in the Umbrella sampling runs

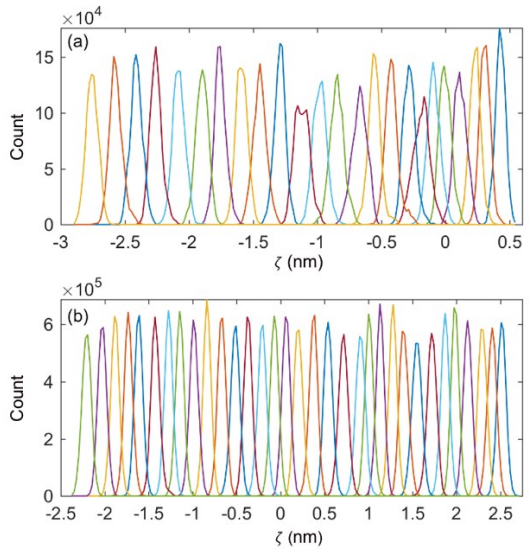

Figure SC-4. *Histograms of the droplet's center of mass during the umbrella sampling runs.* **(a)** The large droplet (diameter: 6.00nm) shown in Fig. 4-1b in the main text at a pressure difference of 31.7MPa between the up- and downstream of the pore. The sampling window size is 0.20nm. **(b)** The small droplet (diameter: 1.84nm). The sampling window size is 0.15nm.

CE. Disjoining pressure effects in the droplet invasion process

To obtain an order of magnitude estimation of when the disjoining pressure effects contribute greatly to the droplet invasion process, we consider the situation where the droplet has already invaded partly into the pore so that the nearly uniform thin water film is formed behind the front portion of the droplet. Figure SC-5 shows the sketch of the 2D system in this situation, where a nearly uniform thin film of a length l is formed. When the thin film grows by dx, the free energy increase due to the disjoining pressure effect is $E_d(\delta)dA'$, where $E_d(\delta)$ is the energy per unit area of a water film with a thickness of δ and $dA' = 2dx$ is the total area increase of the thin water film. According to Equ. 4-1 in the main text, the total free energy change is $dG = \gamma(dA' - dA_b) - \Delta P W_{eff} dx$, where dA_b is the decrease of the surface area of the back part of the invading droplet with a radius of r_b (see Fig. SC-5). Because $dA_b = \frac{W_{eff}}{2r_b} dA'$ (see below), the total free energy change can be expressed in terms of the surface tension as $dG = 2\left(1 - \frac{W_{eff}}{2r_b} - \frac{\Delta P}{P_c}\right)\gamma dx$.

It follows from the above analysis that the ratio between the change of free energy due to the disjoining pressure effects alone and the total change of free energy is $\left|1 - \frac{W_{eff}}{2r_b} - \frac{\Delta P}{P_c}\right|^{-1} E_d(\delta)/\ \gamma$. For a specific system, all parameters but r_b in this ratio are constant. r_b depends on the extent the droplet has invaded into the pore (i.e. l), but generally it is on the order of R_0 during the invasion of the droplet into the pore. Therefore, the ratio between the change of free energy due to the disjoining pressure effects alone and the total change of free energy can be estimated as $\left|1 - \frac{W_{eff}}{2R_0} - \frac{\Delta P}{P_c}\right|^{-1} E_d(\delta)/\ \gamma$, which is shown as Equ. 4.3 in the main text.

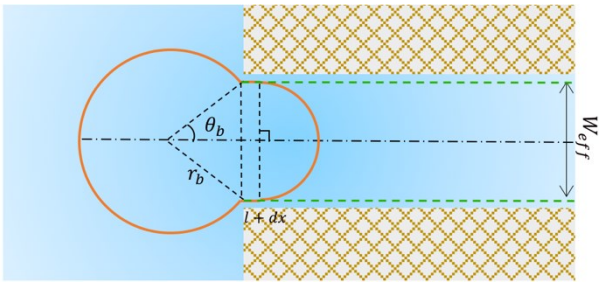

Figure SC-5. *Sketch of thin film growth in a 2D system*. The film length is l and grows by a small amount of length dx. The front part of the droplet is half circle and the back part is partial circle with a radius of r_b and an angle of θ_b.

Here we prove that $dA_b = \frac{W_{eff}}{2r_b} dA'$. As shown in Fig. SC-5, when the film grows by a length of dx, the decrease of the droplet volume outside of the pore is equal to the invasion volume

$$dV = W_{eff} dx \quad \text{(SC. 24)}$$

The volume decrease itself can be expressed in terms of the change of r_b and θ_b

$$dV = d\left((\pi - \theta_b) r_b^2 + \frac{W_{eff}}{2} r_b \cos\theta_b\right) \quad \text{(SC. 25)}$$

With r_b and θ_b related by

$$d(r_b \sin\theta_b) = d\left(\frac{W_{eff}}{2}\right) = 0 \quad \text{(SC. 26)}$$

(SC.25) becomes

$$dV = 2r_b\big((\pi - \theta_r) + \tan\theta_b\big) dr_b \quad \text{(SC. 27)}$$

The surface area decrease of the back part of the droplet is given by

$$dA_b = d(2(\pi - \theta_b) r_b) \quad \text{(SC. 28)}$$

With (SC.26), (SC.28) becomes

$$dA_b = 2\big((\pi - \theta_r) + \tan\theta_b\big) dr_b = dV / r_b \quad \text{(SC. 29)}$$

The increase of the surface area of the thin water film is

$$dA' = 2dx \quad \text{(SC. 30)}$$

Combining (SC.24), (SC.29), and (SC.30), we have

$$dA_b = \frac{W_{eff}}{2r_b} dA' \quad \text{(SC. 31)}$$

CF. Non-equilibrium simulation of droplet invasion into a wide pore

CF.1 Trapping of a droplet at the pore entrance

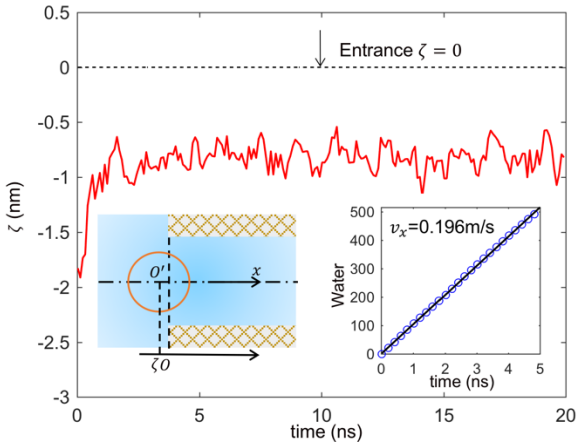

Figure SC-6. *The center-of-mass position of a droplet (diameter: D_1=1.84 nm) in the x-direction during a 20 ns non-equilibrium run.* The droplet is initially placed in front of the pore entrance ($\zeta \approx -1.83$ nm) and a pressure difference of 5 MPa is imposed between the up- and down-stream of the pore. During the non-equilibrium run, the droplet does not enter the pore but remains at $\zeta \approx -0.82$ nm, which is close to the valley of the droplet's potential of mean force near the pore entrance (cf. Fig. 4-6 in the main text). The left inset shows the sketch of the droplet and slit pore. The right inset shows the ensemble average of the cumulative number of water molecules leaving the upstream reservoir as a function of time.

A droplet with a diameter of 1.84nm is initially placed at the entrance of a slit pore with a nominal width of 4.0nm. A pressure difference of 5MPa is imposed between the up- and down-stream of the pore. Figure SC-6 shows the center-of-mass of the droplet during the 20ns non-equilibrium run. We observe that the droplet remains trapped at the pore entrance rather than entering into the pore.

CF.2 The thermodynamic force and hydrodynamic force on the droplet

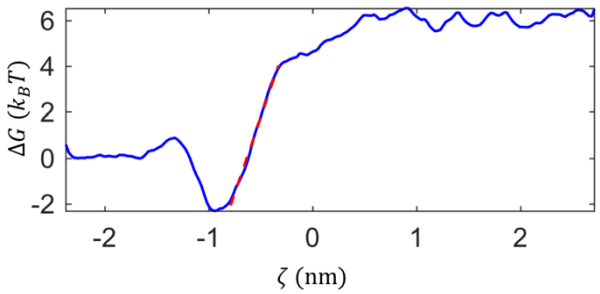

Figure SC-7. *Thermodynamic force acting on a 1.82nm-diameter droplet near the pore entrance.* The force is fitted from the potential of mean force (free energy) of the droplet near the pore entrance.

The thermodynamic force acting on the droplet near the pore entrance is determined by fitting the PMF shown in Fig. 4-6 in the main text (reproduced in Fig. SC-7). The gradient of the PMF, hence the thermodynamic force is non-uniform as the droplet moves into the pore. Since a droplet moving into the pore must overcome the initial thermodynamic barrier very close to the pore entrance, the PMF in this region is fitted to obtain the thermodynamic force acting on the droplet (see Fig. SC-7). A thermodynamic force of 55.47pN is obtained.

To estimate the hydrodynamic drag acting on the droplet by the water flowing around the droplet in the non-equilibrium run, we compute the average velocity of water inside the slit pore. To this end, we monitor the cumulative number of water molecules leaving the upstream reservoir as a function of time, i.e., $n_w^u(t)$. Next, the ensemble average of the cumulative number of water molecules leaving the upstream reservoir is computed as

$$N_f(t) = \langle n_w^u(t) - n_w^u(0) \rangle \quad \text{(SC. 32)}$$

where $\langle \cdots \rangle$ denotes the ensemble average. The mean flux of water through the slit pore is obtained through linear regression of $N_f(t)$ as shown in the inset of Fig. SC-6. The average velocity of water through the slit pore is finally obtained using $U = \frac{1}{\rho_b L_z L_y} \frac{dN_f(t)}{dt}$, where ρ_b is the number density of bulk water, and L_y and L_z are the dimension of the slit pore in the y and z directions, respectively.

The hydrodynamic force is estimated based on hydrodynamic prediction of the drag experienced by a 2D particle confined in a slit channel.[325] Jeong and Yoon showed that the hydrodynamic drag experienced by a particle confined inside a slit pore is given by $F_d = 2\mu U f(D/W)$, where μ and U are viscosity and average velocity of the fluid in the pore, D/W is the ratio between the particle diameter and the pore width.[325] For the MD system considered here, $\alpha = D_1/W \approx 0.46$. Using the numerical results on $f(D/W)$ provided by Jeong and Yoon, the average water velocity in the pore computed above, and the viscosity of SPC/E water at 300K ($\mu = 0.72\text{mPa} \cdot \text{s}$)[302], the hydrodynamic drag per unit depth of the 2D droplet (i.e., its length in the y-

direction in Fig. 4-1b) is determined to be 8.46pN/nm. Because the MD system measures 3.93nm in the depth direction of the droplet, the hydrodynamic drag exerted on the droplet is F_H =33.28pN/nm. The hydrodynamic force estimated here should be the upper bound of that experienced by the droplet in our non-equilibrium MD simulation, in which the droplet is not fully inside the pore (which corresponds to a larger drag force) but is trapped near the pore entrance.

CG. Diffusion coefficients of small droplets in slit pores

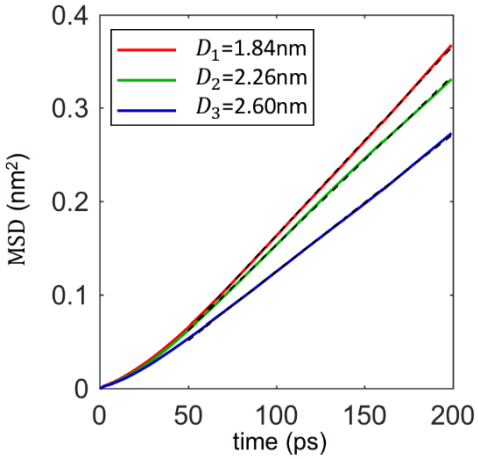

Figure SC-8. *Mean square displacements (MSD) of small droplets confined in slit pores with a nominal width of 4 nm.* The MSD is computed in the plane parallel to the walls of the slit pores.

We performed equilibrium simulations in which the three droplets studied in the main text are confined within a slit pore with the same width but is periodic in the pore length direction. Each simulation lasts 8 ns, and the mean square displacement (MSD) of the center of mass position of each droplet is obtained by analyzing the trajectories saved every 1ps. Figure SC-8 shows the mean-square displacement curve in the plane parallel to the pore walls for each droplet. Fitting of the MSD from 50 ps to 200 ps leads to a diffusion coefficient of 0.51×10^{-9}, 0.45×10^{-9}, and 0.37×10^{9}m^2/s from the droplets with a diameter of 1.84, 2.26, and 2.60nm, respectively.

CH. Free energy profiles of initially spherical droplet invading cylindrical pores

Because it is computationally expensive to run MD simulation of large spherical droplets, we simulated cylindrical droplets that is periodic in the *y*-direction (see Fig. 4-1b), which are 2D

droplets from a continuum perspective. The free energy profiles of the invasion of these droplets into slit pores are obtained through Umbrella sampling as $\Delta G(\zeta)$. It is, however, possible to relate the free energy profile of an initially spherical droplet invading a cylindrical pore, $\Delta G_{3d}(\zeta)$ to that of an initially cylindrical droplet invading a slit pore (i.e. $\Delta G(\zeta)$).

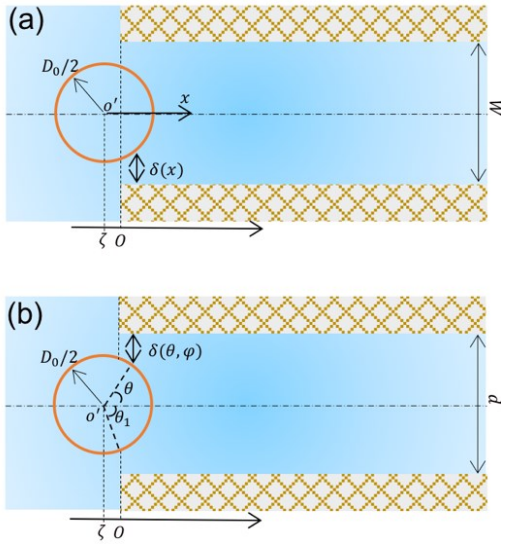

Figure SC-9. *Sketches of the droplet invasion into wide pores.* The droplet's center-of-mass position with respect to the pore entrance in the horizontal direction is ζ. **(a)** A cylindrical droplet with a diameter D_0 invades into slit pore with a width of W. The film thickness δ is a function of x, which is defined as the distance to the droplet center in horizontal direction. **(b)** A spherical droplet with a diameter D_0 invades into cylindrical pore with a diameter of d. θ is the polar angle in the range $[0,\pi]$. φ is the azimuthal angle in the range $[0,2\pi]$ (not drawn here). The film thickness δ is a function of θ and φ.

As shown in Fig. SC-9 a, for the cylindrical droplet with a radius R_0 invading into large slit pore with a width W, the free energy cost due to the formation of the non-uniform thin water film between the droplet and the pore walls is

$$\Delta G(\zeta) = 2L_y \int_{-\zeta}^{R_0} E_d(\delta(x))dx \qquad \text{(SC. 33)}$$

L_y is the length of the cylindrical droplet. $\delta(x)$ is the thickness of the water film at position x. $E_d(\delta(x))$ is the local energy of the film due to the disjoining pressure, which has the same functional form of film thickness at all locations if the disjoining pressure solely depends on the local film thickness. The film thickness at any position can be expressed by $\delta(x) = \frac{W}{2} - \sqrt{D_0^2/4 - x^2}$.

The free energy profile then becomes

$$\Delta G(\zeta) = 2L_y \int_{-\zeta}^{R_0} E_d(\frac{W}{2} - \sqrt{D_0^2/4 - x^2})dx \quad \text{(SC. 34)}$$

Similarly, in the 3D case shown in Fig. SC-9b, for the invasion of spherical droplet D_0 into a cylindrical pore with a diameter d, the free energy cost due to the formation of non-uniform thin film is

$$\Delta G_{3D}(\zeta) = \int_{\theta_1}^{0} \int_{0}^{2\pi} E_d\big(\delta(\theta,\varphi)\big) \sin\theta \, D_0^2/4 d\varphi d\theta \quad \text{(SC. 35)}$$

θ_1 is related to the center-of-mass position of the droplet by $\zeta = -D_0/2\cos\theta_1$. The thickness of the film at any position (θ, φ) can be expressed by $\delta(\theta,\varphi) = d/2 - D_0/2\sin\theta$. Letting $x' = D_0/2\cos\theta$ and intergrading over φ, the free energy profile becomes

$$\Delta G_{3D}(\zeta) = \pi D_0 \int_{-\zeta}^{0} E_d(\frac{d}{2} - \sqrt{D_0^2/4 - x'^2})dx' \quad \text{(SC. 36)}$$

Thus, when the diameter of the cylindrical pore is equal to the width of slit pore, the two free energy profiles can be related to each other by

$$\Delta G_{3\mathrm{D}}(\zeta) = \pi \Delta G(\zeta) d/2L_y \quad \text{(SC. 37)}$$

Disclosure

This work has been published by the American Chemical Society: C. Fang, Q. Kang, R. Qiao, The Role of Disjoining Pressure and Thermal Activation in the Invasion of Droplets into Nanopores. *J. Phys. Chem. C* 2019, 123 (11), 6905-6912.

Appendix D

DA. Molecular models and force field parameters

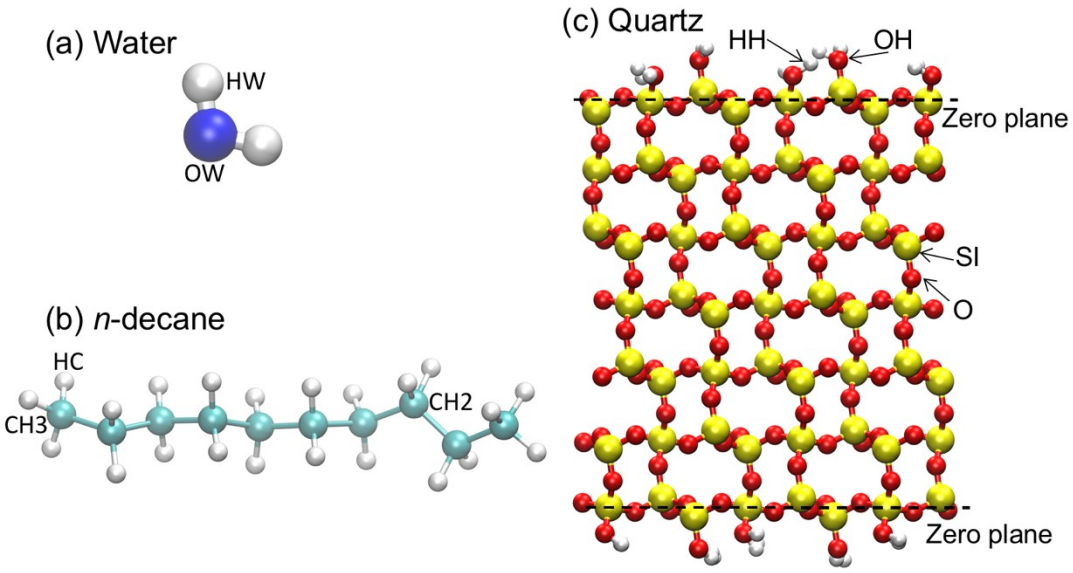

Figure SD-1. Molecular models of water (a), *n*-decane (b). and α-quartz cell cut from the (101) plane.

DA.1 Lennard-Jones parameters and partial charges

Table SD-1. *Lennard-Jones parameters and partial charges*

Atoms	Atom type	Charge (e)	σ_i (nm)	ϵ_i (kJ/mol)
water oxygen	OW	-0.8476	3.166e-1	6.506e-1
water hydrogen	HW	0.4238	0.00	0.00
decane end carbon	CH3	-0.222	3.500e-1	2.761e-1
decane middle carbon	CH2	-0.148	3.500e-1	2.761e-1
decane hydrogen	HC	0.74	3.166e-1	6.50e-1
quartz silicate	SI	2.1	3.020e-1	7.699e-1
quartz oxygen	O	-1.05	3.166e-1	6.506e-1
quartz oxygen of silanol group	OH	-0.95	3.166e-1	6.506e-1
quartz hydrogen of silanol group	HH	0.425	0.00	0.00
sodium ion	NA	1	2.160e-1	1.475
chloride ion	CL	-1	4.830e-1	5.349e-2

DA.2 Boned parameters

(a) The bond stretching between two boned atoms *i* and *j* is represented by a harmonic potential,

$$V_b(r_{ij}) = \frac{1}{2}k_{ij}^b(r_{ij} - b_{ij})^2 \quad \text{(SD. 1)}$$

The bond parameters are listed in Table SD-2.

Table SD-2. *Bond parameters*

Bond type	b (nm)	k^b (kJ/mol/nm^2)
OW-HW	9.572e-1	5.021e5
CH3(CH2)-CH2	1.529e-1	2.243e5
CH3(CH2)-CH	1.09e-1	2.845e5
OH-HH	1.0	4.637e5

(b) The angle vibration between three atoms *i, j,* and *k* is represented by a harmonic potential,

$$V_a(\theta_{ijk}) = \frac{1}{2}k_{ijk}^a(\theta_{ijk} - \theta_{ijk}^0)^2 \quad \text{(SD. 2)}$$

The angle parameters are listed in Table SD-3.

Table SD-3. *Angle parameters*

Angle type	k^a (kJ/mol/rad^2)	θ^0 (degree)
HW-OW-HW	6.276000e+02	109.5
CH2 -CH2-CH2 (CH3)	4.882730e+02	112.7
CH2(CH3)-CH2(CH3)-HC	3.138000e+02	110.7
HC-CH2(CH3)-HC	2.761440e+02	107.8
SI-OH-HH	5.271840e+02	109.47

(c) The Ryckaert-Bellemans proper dihedral is used,

$$V_{rb}(\phi_{ijkl}) = \sum_{n=0}^{5} C_n(\cos(\phi_{ijkl} - 180^o))^n \quad \text{(SD. 3)}$$

The dihedral parameters are listed Table SD-4.

Table SD-4. *Dihedral parameters*

Dihedral type	c_0 (kJ/mol)	c_1 (kJ/mol)	c_2 (kJ/mol)	c_3 (kJ/mol)	c_4 (kJ/mol)	c_5 (kJ/mol)
CH2(CH3)-CH2-CH2-CH2(CH3)	5.1879e-01	-2.3019e-01	8.9681e-01	1.4913e+00	0	0
HC-CH2-CH2-CH2(CH3, HC)	6.2760e-01	-1.8828e+00	0	2.5104e+00	0	0

DB. Thin brine films during last 100ns of simulation

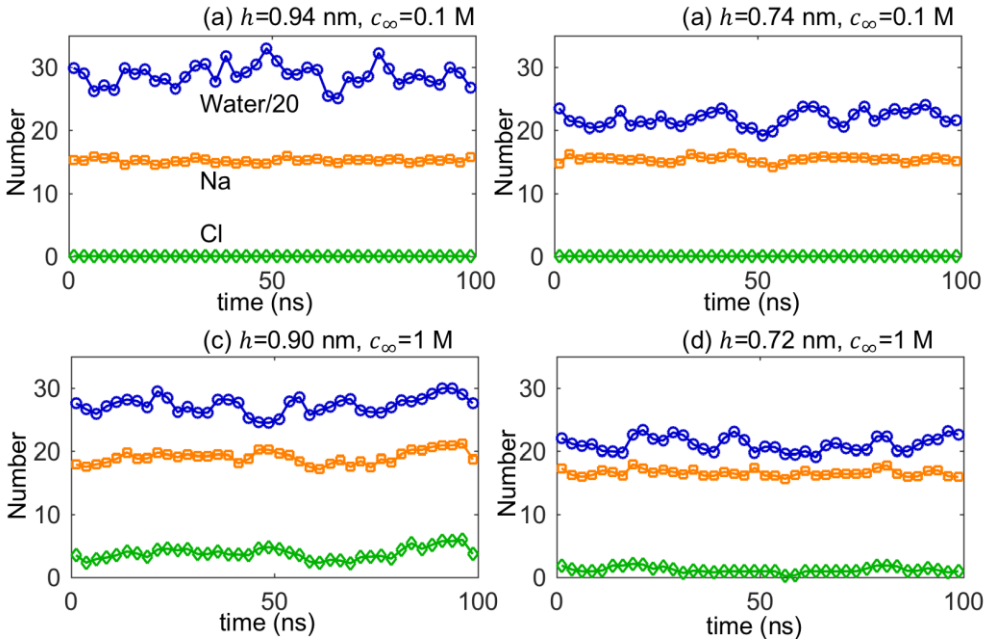

Figure SD-2. *The number of water and ions in thin brine films during the last 100ns of equilibrium simulation.* The number is computed within the red dashed box shown in Fig. 5-1a. The number is averaged every 2.5ns.

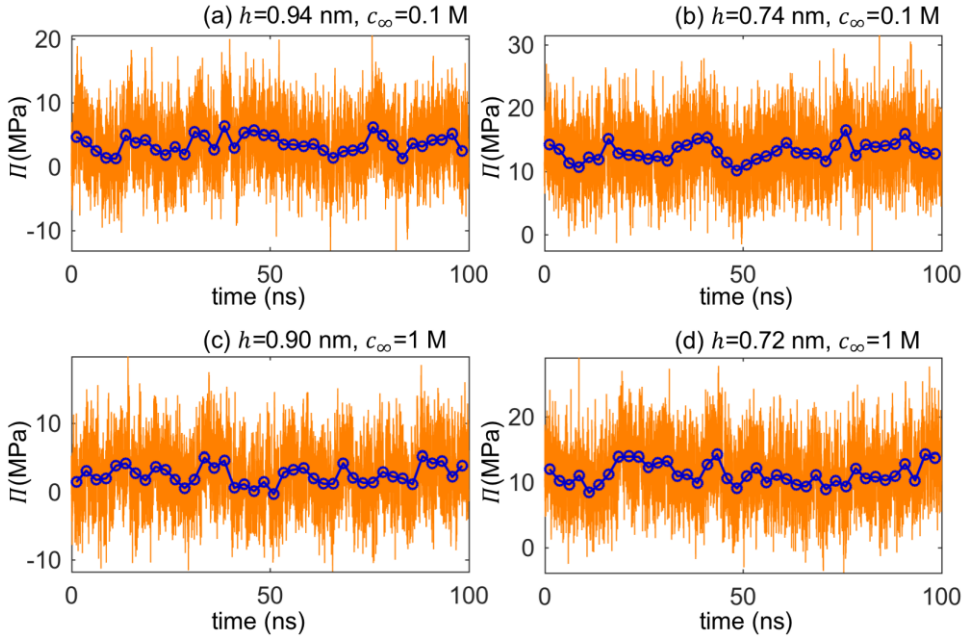

Figure SD-3. *The pressure on the top piston during the last 100ns of simulation.* The pressure at each time step is shown in lines (orange) and the running average with a window of 2.5ns is shown in symbols (blue).

DC. Water-oil interface at 1M thin brine film

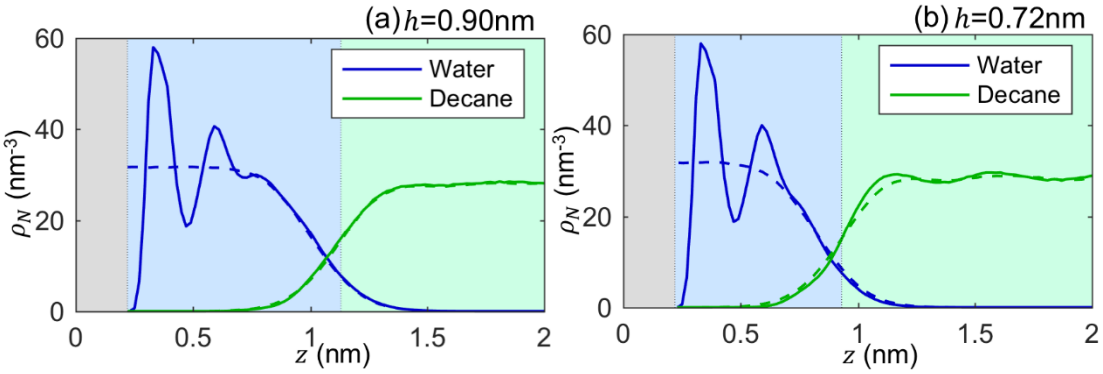

Figure SD-4. The density profiles of water and oil near quartz surface for two different film thickness: **(a)** h=0.90nm and **(b)** h=0.72nm.

DD. Geometry of decane molecules.

We introduce a gyration tensor for each decane molecule:

$$S_{mn} = \sum_{i,j}(r_m^{(i)} - r_m^{(j)})(r_n^{(i)} - r_n^{(j)}), \qquad \text{(SD. 4)}$$

where $r_m^{(i)}$ is the mth Cartesian coordinate of the position vector $\boldsymbol{r}^{(i)}$ of the ith atom. Diagonalizing S_{mn} effectively fits the decane molecule to an ellipsoid. S_{mn}'s eigenvalues σ_k (k=1, 2, 3 from the largest to smallest eigenvalues) are the principle moments of the gyration tensor. The radius of gyration of a decane molecule can be given by $R_g^2 = \sigma_1^2 + \sigma_2^2 + \sigma_3^2$. The eigenvectors $\boldsymbol{S}_k$ of the gyration tensor are the decane molecule's principle axis.

DE. Static dielectric constant of SPC/E water

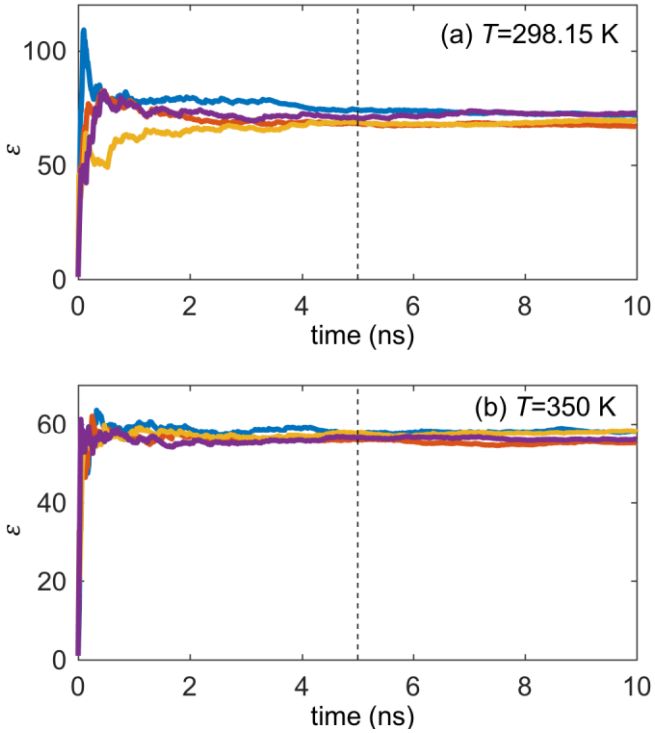

Figure SD-5. *The static dielectric constant of SPC/E water.* 900 water molecules are included inside a periodic simulation box. The convergence of dielectric constant, ε, during four independent simulations done at T=298.15 K **(a)** and T=350 K **(b)**. ε is obtained by computing the total dipole moment fluctuation in the system.[370-371] The averages are taken from the last 5ns and the error bars are obtained from four cases. At T=298.15 K, $\varepsilon = 70.14 \pm 2.63$, in agreement with that reported in previous simulations with the same water model.[390] At T=350 K, $\varepsilon = 56.83 \pm 1.31$.

DF. Radial distribution function in NaCl solution

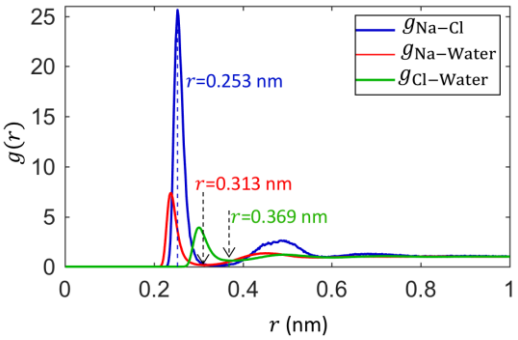

Figure SD-6. *The radial density functions of Cl^- ions around Na^+ ions, water molecules around Na^+ ions, and water molecules around Cl^- ions.* The radial density functions are obtained for a 1M NaCl solution in a $4.5 \times 4.5 \times 4.5$ nm^3 box. The locations of the 1st peak of $g_{\mathrm{Na-CL}}$, 1st valley of $g_{\mathrm{Na-Water}}$, and 1st valley of $g_{\mathrm{Cl-Water}}$ are labeled.

DG. Co-ion density profiles in b 1M brine films

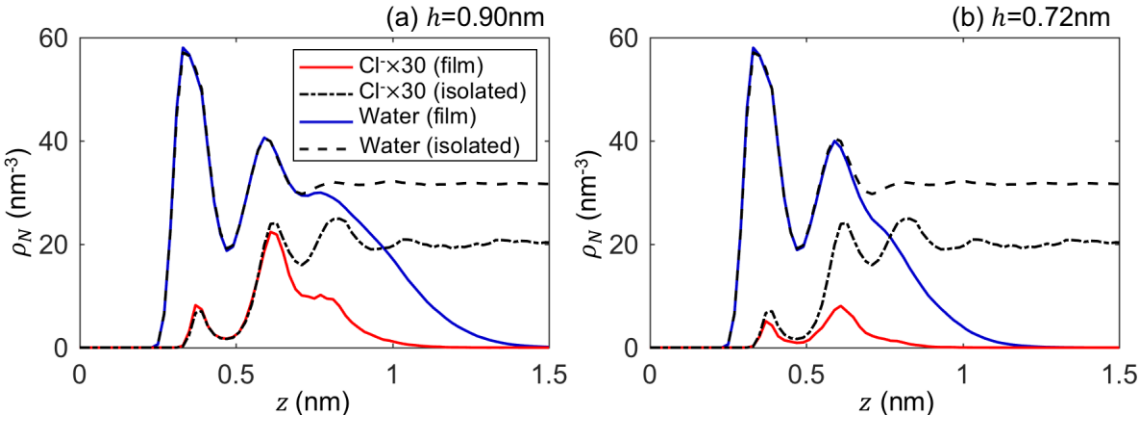

Figure SD-7. *Cl^- ion and water distribution in brine films with a reservoir ion concentration of 1.0M.* **(a)** The film thickness is 0.90nm. **(b)** The film thickness is 0.72nm.

DH. Hydrodynamic properties of thick water film in Fig. 5-11.

With the model sketched in Fig. 5-11c, the no-slip plane can be obtained by extrapolating the linear part of the velocity profile of water (1nm<z<3nm in Fig. 5-11b) towards the rock surface. The position of the no-slip plane is taken as the position where extrapolated water velocity is zero (z= 0.51nm in Fig. 5-11b and consequently δ= 0.29nm).

The slip velocity is obtained by extrapolating both linear parts of the velocity profiles of water (1nm<z<3nm) and decane (5nm<z<6.5nm) to the nominal interface of water-oil (z=4.07nm). The slip velocity is V_{slip}=9.89 m/s (shown in Fig. 5-11b). To obtain the slip coefficient $\beta = \tau/V_{slip}$, the shear stress τ across liquids is needed. On the oil side, shear stress can be obtained from $\tau = \mu_{e,d}\partial V_{oil}/\partial z$ by using the bulk decane viscosity at 350K (see Fig. SD-8) and the shear rate in the linear part of velocity profile (5nm<z<6.5nm in Fig. 5-11b). Consequently, the slip coefficient is $\beta = 0.39 \pm 0.04$ MPa·s/m. At another shear rate (piston velocity at 50m/s), the slip coefficient becomes $\beta = 0.39 \pm 0.02$ MPa·s/m, further demonstrating that the slip coefficient is a material property inherent to the oil-water interface.[384, 386]

The viscosity of water can be obtained by equating the shear stress $\mu_{e,d}\partial V_{oil}/\partial z = \mu_{e,w}\partial V_{water}/\partial z$ between the two linear parts of the velocity profiles of water and oil. The viscosity of water is

found to be 0.39±0.04 mPa·s, which is close to that reported for bulk SPC/E water around 350K.[391]

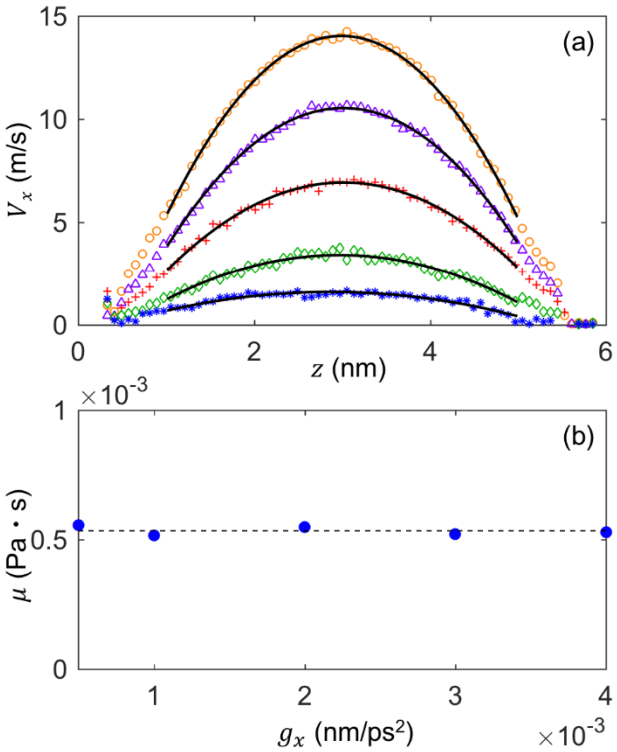

Figure SD-8. *The dynamic viscosity of n-decane at 350K.* The viscosity is calculated from a system with ~5nm thick slab of decane confined between quartz and piston. A constant acceleration g_x is applied to decane atoms in the *x*-direction. **(a)** The velocity profiles of decane's carbon atoms with accelerations g_x= 0.5×10^{-3}, 1×10^{-3}, 2×10^{-3}, 3×10^{-3}, and 4×10^{-3} nm/ps^2. The velocity profile in the region 1nm<z<5nm is fitted to a parabolic profile $V_x(z) = 0.5az^2 + bz + c$. **(b)** The decane viscosity is obtained from the relation $\rho_c g_x = -\mu_{e,d}\partial^2 V_x/\partial z^2$, where ρ_c is the density of carbon atoms and $\partial^2 V_x/\partial z^2$ is taken as a from the fitted parabolic profile. The viscosity is almost unchanged with different accelerations, meaning a linear response at these velocities. The final average viscosity is averaged over each acceleration as 0.63mPa·s and shown as a dashed line.

References

1. Holditch, S. A.; Chianelli, R. R., Factors That Will Influence Oil and Gas Supply and Demand in the 21st Century. *MRS Bull.* **2008**, *33*, 317-323.
2. Arutyunov, V. S.; Lisichkin, G. V., Energy Resources of the 21st Century: Problems and Forecasts. Can Renewable Energy Sources Replace Fossil Fuels? *Russian Chemical Reviews* **2017**, *86*, 777.
3. Zou, C.; Yang, Z.; Tao, S.; Yuan, X.; Zhu, R.; Hou, L.; Wu, S.; Sun, L.; Zhang, G.; Bai, B., Continuous Hydrocarbon Accumulation over a Large Area as a Distinguishing Characteristic of Unconventional Petroleum: The Ordos Basin, North-Central China. *Earth-Science Reviews* **2013**, *126*, 358-369.
4. Wenrui, H.; Jingwei, B.; Bin, H., Trend and Progress in Global Oil and Gas Exploration. *Petroleum Exploration and Development* **2013**, *40*, 439-443.
5. Dudley, B., Bp Statistical Review of World Energy 2016. *London, UK* **2015**.
6. Abas, N.; Kalair, A.; Khan, N., Review of Fossil Fuels and Future Energy Technologies. *Futures* **2015**, *69*, 31-49.
7. Ellabban, O.; Abu-Rub, H.; Blaabjerg, F., Renewable Energy Resources: Current Status, Future Prospects and Their Enabling Technology. *Renewable and Sustainable Energy Reviews* **2014**, *39*, 748-764.
8. Sieminski, A., Outlook for Shale Gas and Tight Oil Development in the Us. 2013.
9. Mohr, S. H.; Evans, G. M., Forecasting Coal Production until 2100. *Fuel* **2009**, *88*, 2059-2067.
10. Cohen, G.; Joutz, F.; Loungani, P., Measuring Energy Security: Trends in the Diversification of Oil and Natural Gas Supplies. *Energy policy* **2011**, *39*, 4860-4869.
11. De Almeida, P.; Silva, P. D., Timing and Future Consequences of the Peak of Oil Production. *Futures* **2011**, *43*, 1044-1055.
12. Aguilera, R., Flow Units: From Conventional to Tight-Gas to Shale-Gas to Tight-Oil to Shale-Oil Reservoirs. *SPE Reservoir Evaluation & Engineering* **2014**, *17*, 190-208.
13. Lee, K. S.; Kim, T. H., *Integrative Understanding of Shale Gas Reservoirs*; Springer, 2016.
14. Islam, M. R., *Unconventional Gas Reservoirs: Evaluation, Appraisal, and Development*; Elsevier, 2014.
15. Aguilera, R. F.; Harding, T.; Krause, F. In *Natural Gas Production from Tight Gas Formations: A Global Perspective*, 19th World Petroleum Congress, World Petroleum Congress: 2008.
16. Zou, C., *Unconventional Petroleum Geology*; Elsevier, 2017.
17. Caineng, Z.; Zhi, Y.; Zhang, G.; Lianhua, H.; Rukai, Z.; Shizhen, T.; Xuanjun, Y.; Yuman, W.; Qiulin, G.; Lan, W., Conventional and Unconventional Petroleum "Orderly Accumulation": Concept and Practical Significance. *Petroleum Exploration and Development* **2014**, *41*, 14-30.
18. Caineng, Z.; Guangming, Z.; Zhang, G.; Hongjun, W.; Zhang, G.; Jianzhong, L.; Zhaoming, W.; Zhixin, W.; Feng, M.; Liang, Y., Formation, Distribution, Potential and Prediction of Global Conventional and Unconventional Hydrocarbon Resources. *Petroleum Exploration and Development* **2015**, *42*, 14-28.
19. Wang, Z.; Krupnick, A., A Retrospective Review of Shale Gas Development in the United States: What Led to the Boom? *Economics of Energy & Environmental Policy* **2015**, *4*, 5-18.
20. Sieminski, A., Outlook for Us Shale Oil and Gas. *USEI Administration (ed) Argus Americas Crude*

Summit, Houston **2014**.

21. Sheng, J. J., Critical Review of Field Eor Projects in Shale and Tight Reservoirs. *Journal of Petroleum Science and Engineering* **2017**, *159*, 654-665.
22. Soeder, D. J., The Successful Development of Gas and Oil Resources from Shales in North America. *Journal of Petroleum Science and Engineering* **2018**, *163*, 399-420.
23. Salama, A.; Amin, M. F. E.; Kumar, K.; Sun, S., Flow and Transport in Tight and Shale Formations: A Review. *Geofluids* **2017**, *2017*.
24. Prasad, M.; Pal-Bathija, A.; Johnston, M.; Rydzy, M.; Batzle, M., Rock Physics of the Unconventional. *The Leading Edge* **2009**, *28*, 34-38.
25. An, C.; Yan, B.; Alfi, M.; Mi, L.; Killough, J. E.; Heidari, Z., Estimating Spatial Distribution of Natural Fractures by Changing Nmr T2 Relaxation with Magnetic Nanoparticles. *Journal of Petroleum Science and Engineering* **2017**, *157*, 273-287.
26. Hosterman, J. W.; Whitlow, S. I., Munsell Color Value as Related to Organic Carbon in Devonian Shale of Appalachian Basin. *AAPG Bulletin* **1981**, *65*, 333-335.
27. Howarth, R. W.; Santoro, R.; Ingraffea, A., Methane and the Greenhouse-Gas Footprint of Natural Gas from Shale Formations. *Climatic Change* **2011**, *106*, 679.
28. Bohacs, K. M.; Grabowski Jr, G. J.; Carroll, A. R.; Mankiewicz, P. J.; Miskell-Gerhardt, K. J.; Schwalbach, J. R.; Wegner, M. B.; Simo, J. T., Production, Destruction, and Dilution—the Many Paths to Source-Rock Development. **2005**.
29. Passey, Q. R.; Bohacs, K.; Esch, W. L.; Klimentidis, R.; Sinha, S. In *From Oil-Prone Source Rock to Gas-Producing Shale Reservoir-Geologic and Petrophysical Characterization of Unconventional Shale Gas Reservoirs*, International oil and gas conference and exhibition in China, Society of Petroleum Engineers: 2010.
30. Wang, L.; Cao, H., Probable Mechanism of Organic Pores Evolution in Shale: Case Study in Dalong Formation, Lower Yangtze Area, China. *Journal of Natural Gas Geoscience* **2016**, *1*, 295-298.
31. Javadpour, F.; Fisher, D.; Unsworth, M., Nanoscale Gas Flow in Shale Gas Sediments. *Journal of Canadian Petroleum Technology* **2007**, *46*.
32. King, H., Utica Shale: The Natural Gas Giant Below the Marcellus. *Geology. com* **2017**.
33. Kolodzie, S. In *The Analysis of Pore Throat Size and Use of Waxman-Smit to Determine Ooip in Spindle Field, Colorado: Spe 55, H Annual Fall Tech*, Conf. and Exhib., SPE Paper, 1980.
34. Charpentier, R. R.; Cook, T. A. *Usgs Methodology for Assessing Continuous Petroleum Resources*; 2331-1258; US Geological Survey: 2011.
35. Jianzhong, J.; Min, L. D. Z., Assessment Criteria, Main Types, Basic Features and Resource Prospects of the Tight Oil in China [J]. *Acta Petrolei Sinica* **2012**, *3*.
36. Forrest, J.; Birn, K.; Brink, S.; Comb, T.; Cuthbert, B.; Dunbar, R.; Harju, J.; Isaace, E.; Jones, F.; Khanna, P., Working Document of the Npc North American Resource Development Study-Unconventional Oil. *US National Petroleum Council (NPC)* **2011**.
37. King Jr, H. E.; Eberle, A. P.; Walters, C. C.; Kliewer, C. E.; Ertas, D.; Huynh, C., Pore Architecture and Connectivity in Gas Shale. *Energy Fuels* **2015**, *29*, 1375-1390.

38. Gu, X.; Cole, D. R.; Rother, G.; Mildner, D. F.; Brantley, S. L., Pores in Marcellus Shale: A Neutron Scattering and Fib-Sem Study. *Energy & Fuels* **2015**, *29*, 1295-1308.
39. Russian, A.; Gouze, P.; Dentz, M.; Gringarten, A., Multi-Continuum Approach to Modelling Shale Gas Extraction. *Transport in Porous Media* **2015**, *109*, 109-130.
40. Ethridge, S.; Bredfeldt, T.; Sheedy, K.; Shirley, S.; Lopez, G.; Honeycutt, M., The Barnett Shale: From Problem Formulation to Risk Management. *Journal of Unconventional Oil and Gas Resources* **2015**, *11*, 95-110.
41. Estrada, J. M.; Bhamidimarri, R., A Review of the Issues and Treatment Options for Wastewater from Shale Gas Extraction by Hydraulic Fracturing. *Fuel* **2016**, *182*, 292-303.
42. Fisher, K., Data Confirm Safety of Well Fracturing. *The American Oil & Gas Reporter* **2010**.
43. Beims, T., Purple Hayes No. 1h Ushers in Step Changes in Lateral Length, Well Cost. *The American Oil and Gas Reporter* **2016**.
44. Muresan, J.; Ivan, M., Controversies Regarding Costs, Uncertainties and Benefits Specific to Shale Gas Development. *Sustainability* **2015**, *7*, 2473-2489.
45. Habibi, A.; Xu, M.; Dehghanpour, H.; Bryan, D.; Uswak, G. In *Understanding Rock-Fluid Interactions in the Montney Tight Oil Play*, SPE/CSUR unconventional resources conference, Society of Petroleum Engineers: 2015.
46. Dutta, R.; Lee, C.-H.; Odumabo, S.; Ye, P.; Walker, S. C.; Karpyn, Z. T.; Ayala, H.; Luis, F., Experimental Investigation of Fracturing-Fluid Migration Caused by Spontaneous Imbibition in Fractured Low-Permeability Sands. *SPE Reservoir Evaluation & Engineering* **2014**, *17*, 74-81.
47. Yethiraj, A.; Striolo, A., Fracking: What Can Physical Chemistry Offer? ACS Publications: 2013.
48. Vengosh, A.; Jackson, R. B.; Warner, N.; Darrah, T. H.; Kondash, A., A Critical Review of the Risks to Water Resources from Unconventional Shale Gas Development and Hydraulic Fracturing in the United States. *Environmental science & technology* **2014**, *48*, 8334-8348.
49. Duda, J.; Salamy, S.; Aminian, K.; Ameri, S., Pressure Analysis of an Unstimulated Horizontal Well with Type Curves. *Journal of Petroleum Technology* **1991**, *43*, 988-993.
50. Hill, R.; Middlebrook, M.; Peterson, R.; Johnson, E.; McKetta, S.; Wilson, G.; Branagan, P., Horizontal Gas Well Completion Technology in the Barnett Shale—Analysis of the Mitchell Energy Corporation T.P. Sims B No. 1, Wise County, Texas. **1993**, 68.
51. Mantle, K., Defining Directional Drilling: The Art of Controlling Wellbore Trajectory. *Schlumberger Oilfield Rev.* **2014**, *25*, 54-55.
52. Chen, X.; Gao, D.; Guo, B.; Luo, L.; Liu, X.; Zhang, X., A New Method for Determining the Minimum Gas Injection Rate Required for Hole Cleaning in Horizontal Gas Drilling. *J Nat Gas Sci Eng* **2014**, *21*, 1084-1090.
53. Chen, X.; Gao, D.; Guo, B., Optimal Design of Jet Mill Bit for Jet Comminuting Cuttings in Horizontal Gas Drilling Hard Formations. *J Nat Gas Sci Eng* **2016**, *28*, 587-593.
54. Yu, W.; Zhang, T.; Du, S.; Sepehrnoori, K., Numerical Study of the Effect of Uneven Proppant Distribution between Multiple Fractures on Shale Gas Well Performance. *Fuel* **2015**, *142*, 189-198.
55. Bilgen, S.; Sarıkaya, İ., New Horizon in Energy: Shale Gas. *J Nat Gas Sci Eng* **2016**, *35*, 637-645.

56. Li, J.; Gong, B.; Wang, H., Mixed Integer Simulation Optimization for Optimal Hydraulic Fracturing and Production of Shale Gas Fields. *Engineering Optimization* **2016**, *48*, 1378-1400.
57. de Rijke, K., Produced Water, Money Water, Living Water: Anthropological Perspectives on Water and Fracking. *Wiley Interdisciplinary Reviews: Water* **2018**, *5*, e1272.
58. Burton, T. G.; Rifai, H. S.; Hildenbrand, Z. L.; Carlton Jr, D. D.; Fontenot, B. E.; Schug, K. A., Elucidating Hydraulic Fracturing Impacts on Groundwater Quality Using a Regional Geospatial Statistical Modeling Approach. *Science of the Total Environment* **2016**, *545*, 114-126.
59. King, G. E. In *Thirty Years of Gas Shale Fracturing: What Have We Learned?*, SPE Annual Technical Conference and Exhibition, Society of Petroleum Engineers: 2010.
60. Arthur, J. D.; Bohm, B.; Layne, M., Hydraulic Fracturing Considerations for Natural Gas Wells of the Marcellus Shale. **2009**.
61. Jackson, R. B.; Vengosh, A.; Carey, J. W.; Davies, R. J.; Darrah, T. H.; O'sullivan, F.; Pétron, G., The Environmental Costs and Benefits of Fracking. *Annual Review of Environment and Resources* **2014**, *39*, 327-362.
62. Clark, C.; Veil, J. *Produced Water Volumes and Management Practices in the United States*; Argonne National Lab.(ANL), Argonne, IL (United States): 2009.
63. Rush, P. V., The Threat from Hydrofracking. *Journal-American Water Works Association* **2010**, *102*, 26-30.
64. Gordalla, B. C.; Ewers, U.; Frimmel, F. H., Hydraulic Fracturing: A Toxicological Threat for Groundwater and Drinking-Water? *Environmental earth sciences* **2013**, *70*, 3875-3893.
65. Elsner, M.; Hoelzer, K., Quantitative Survey and Structural Classification of Hydraulic Fracturing Chemicals Reported in Unconventional Gas Production. *Environmental science & technology* **2016**, *50*, 3290-3314.
66. Montgomery, C. T.; Smith, M. B., Hydraulic Fracturing: History of an Enduring Technology. *Journal of Petroleum Technology* **2010**, *62*, 26-40.
67. Loh, H.-P.; Loh, N., Hydraulic Fracturing and Shale Gas: Environmental and Health Impacts. In *Advances in Water Resources Management*, Springer: 2016; pp 293-337.
68. Meng, Q.; Ashby, S., Distance: A Critical Aspect for Environmental Impact Assessment of Hydraulic Fracking. *The Extractive Industries and Society* **2014**, *1*, 124-126.
69. Gregory, K. B.; Vidic, R. D.; Dzombak, D. A., Water Management Challenges Associated with the Production of Shale Gas by Hydraulic Fracturing. *Elements* **2011**, *7*, 181-186.
70. Warner, N. R.; Jackson, R. B.; Darrah, T. H.; Osborn, S. G.; Down, A.; Zhao, K.; White, A.; Vengosh, A., Geochemical Evidence for Possible Natural Migration of Marcellus Formation Brine to Shallow Aquifers in Pennsylvania. *Proc. Natl. Acad. Sci. U.S.A.* **2012**, *109*, 11961-11966.
71. Myers, T., Potential Contaminant Pathways from Hydraulically Fractured Shale to Aquifers. *Groundwater* **2012**, *50*, 872-882.
72. Cohen, H. A.; Parratt, T.; Andrews, C. B., Potential Contaminant Pathways from Hydraulically Fractured Shale to Aquifers. *Groundwater* **2013**, *51*, 317-319.
73. Myers, T., Potential Contaminant Pathways from Hydraulically Fractured Shale to Aquifers Author's

Reply. WILEY-BLACKWELL 111 RIVER ST, HOBOKEN 07030-5774, NJ USA: 2013.
74. Saiers, J. E.; Barth, E., Potential Contaminant Pathways from Hydraulically Fractured Shale Aquifers. *Groundwater* **2012**, *50*, 826-828.
75. Engelder, T., Capillary Tension and Imbibition Sequester Frack Fluid in Marcellus Gas Shale. *Proc. Natl. Acad. Sci. U.S.A.* **2012**, *109*, E3625-E3625.
76. Flewelling, S. A.; Sharma, M., Constraints on Upward Migration of Hydraulic Fracturing Fluid and Brine. *Groundwater* **2014**, *52*, 9-19.
77. Birdsell, D. T.; Rajaram, H.; Dempsey, D.; Viswanathan, H. S., Hydraulic Fracturing Fluid Migration in the Subsurface: A Review and Expanded Modeling Results. *Water Resour. Res.* **2015**, *51*, 7159-7188.
78. Jackson, R. B.; Vengosh, A.; Darrah, T. H.; Warner, N. R.; Down, A.; Poreda, R. J.; Osborn, S. G.; Zhao, K.; Karr, J. D., Increased Stray Gas Abundance in a Subset of Drinking Water Wells near Marcellus Shale Gas Extraction. *Proc. Natl. Acad. Sci. U.S.A.* **2013**, *110*, 11250-11255.
79. Osborn, S. G.; Vengosh, A.; Warner, N. R.; Jackson, R. B., Methane Contamination of Drinking Water Accompanying Gas-Well Drilling and Hydraulic Fracturing. *Proc. Natl. Acad. Sci. U.S.A.* **2011**, *108*, 8172-8176.
80. Weaver, T.; Frape, S.; Cherry, J., Recent Cross-Formational Fluid Flow and Mixing in the Shallow Michigan Basin. *Geological Society of America Bulletin* **1995**, *107*, 697-707.
81. Long, D. T.; Wilson, T. P.; Takacs, M. J.; Rezabek, D. H., Stable-Isotope Geochemistry of Saline near-Surface Ground Water: East-Central Michigan Basin. *Geological Society of America Bulletin* **1988**, *100*, 1568-1577.
82. Mehta, S.; Fryar, A. E.; Banner, J. L., Controls on the Regional-Scale Salinization of the Ogallala Aquifer, Southern High Plains, Texas, USA. *Applied Geochemistry* **2000**, *15*, 849-864.
83. Mehta, S.; Fryar, A.; Brady, R.; Morin, R. H., Modeling Regional Salinization of the Ogallala Aquifer, Southern High Plains, Tx, USA. *Journal of Hydrology* **2000**, *238*, 44-64.
84. Kissinger, A.; Helmig, R.; Ebigbo, A.; Class, H.; Lange, T.; Sauter, M.; Heitfeld, M.; Klünker, J.; Jahnke, W., Hydraulic Fracturing in Unconventional Gas Reservoirs: Risks in the Geological System, Part 2. *Environmental earth sciences* **2013**, *70*, 3855-3873.
85. Roychaudhuri, B.; Tsotsis, T. T.; Jessen, K., An Experimental Investigation of Spontaneous Imbibition in Gas Shales. *Journal of Petroleum Science and Engineering* **2013**, *111*, 87-97.
86. Ghanbari, E.; Dehghanpour, H., Impact of Rock Fabric on Water Imbibition and Salt Diffusion in Gas Shales. *International Journal of Coal Geology* **2015**, *138*, 55-67.
87. Lan, Q.; Ghanbari, E.; Dehghanpour, H. In *Water Loss Versus Soaking Time: Spontaneous Imbibition in Tight Rocks*, SPE/EAGE European Unconventional Resources Conference and Exhibition, 2014.
88. Byrnes, A. P., Role of Induced and Natural Imbibition in Frac Fluid Transport and Fate in Gas Shales. *for the Hydraulic Fracturing Study: Fate and Transport* **2011**, 70.
89. Makhanov, K.; Habibi, A.; Dehghanpour, H.; Kuru, E., Liquid Uptake of Gas Shales: A Workflow to Estimate Water Loss During Shut-in Periods after Fracturing Operations. *Journal of Unconventional Oil and Gas Resources* **2014**, *7*, 22-32.
90. Bahrami, H.; Rezaee, R.; Clennell, B., Water Blocking Damage in Hydraulically Fractured Tight Sand

Gas Reservoirs: An Example from Perth Basin, Western Australia. *Journal of Petroleum Science and Engineering* **2012**, *88*, 100-106.

91. Shaoul, J. R.; van Zelm, L. F.; De Pater, C., Damage Mechanisms in Unconventional-Gas-Well Stimulation--a New Look at an Old Problem. *SPE Production & Operations* **2011**, *26*, 388-400.
92. Paktinat, J.; Pinkhouse, J. A.; Johnson, N. J.; Williams, C.; Lash, G. G.; Penny, G. S.; Goff, D. A. In *Case Studies: Optimizing Hydraulic Fracturing Performance in Northeastern Fractured Shale Formations*, SPE Eastern Regional Meeting, Society of Petroleum Engineers: 2006.
93. Lucas, R., Ueber Das Zeitgesetz Des Kapillaren Aufstiegs Von Flüssigkeiten. *Colloid & Polymer Science* **1918**, *23*, 15-22.
94. Washburn, E. W., The Dynamics of Capillary Flow. *Phys. Rev.* **1921**, *17*, 273.
95. Singh, H., A Critical Review of Water Uptake by Shales. *J Nat Gas Sci Eng* **2016**, *34*, 751-766.
96. Handy, L., Determination of Effective Capillary Pressures for Porous Media from Imbibition Data. **1960**.
97. Li, K.; Horne, R. N. In *Characterization of Spontaneous Water Imbibition into Gas-Saturated Rocks*, SPE/AAPG Western Regional Meeting, Society of Petroleum Engineers: 2000.
98. Cai, J.; Perfect, E.; Cheng, C.-L.; Hu, X., Generalized Modeling of Spontaneous Imbibition Based on Hagen–Poiseuille Flow in Tortuous Capillaries with Variably Shaped Apertures. *Langmuir* **2014**, *30*, 5142-5151.
99. Schmid, K.; Geiger, S.; Sorbie, K., Semianalytical Solutions for Cocurrent and Countercurrent Imbibition and Dispersion of Solutes in Immiscible Two-Phase Flow. *Water Resour. Res.* **2011**, *47*.
100. Schmid, K.; Geiger, S., Universal Scaling of Spontaneous Imbibition for Arbitrary Petrophysical Properties: Water-Wet and Mixed-Wet States and Handy's Conjecture. *Journal of Petroleum Science and Engineering* **2013**, *101*, 44-61.
101. Das, S.; Mitra, S. K., Different Regimes in Vertical Capillary Filling. *Phys. Rev. E* **2013**, *87*.
102. Cao, G.; Qiao, Y.; Zhou, Q.; Chen, X., Infiltration Behaviour of Water in a Carbon Nanotube under External Pressure. *Philos. Mag. Lett.* **2008**, *88*, 371-378.
103. Supple, S.; Quirke, N., Rapid Imbibition of Fluids in Carbon Nanotubes. *Phys. Rev. Lett.* **2003**, *90*.
104. Yamashita, K.; Daiguji, H., Molecular Dynamics Simulations of Water Uptake into a Silica Nanopore. *J. Phys. Chem. C* **2015**, *119*, 3012-3023.
105. Mo, J.; Li, L.; Zhou, J.; Xu, D.; Huang, B.; Li, Z., Fluid Infiltration Pressure for Hydrophobic Nanochannels. *Phys. Rev. E* **2015**, *91*, 033022.
106. Oyarzua, E.; Walther, J. H.; Mejia, A.; Zambrano, H. A., Early Regimes of Water Capillary Flow in Slit Silica Nanochannels. *Phys. Chem. Chem. Phys.* **2015**, *17*, 14731-14739.
107. Henrich, B.; Cupelli, C.; Santer, M.; Moseler, M., Continuum Concepts in Nanoscale Capillary Impregnation. *New J. Phys.* **2008**, *10*.
108. Joly, L., Capillary Filling with Giant Liquid/Solid Slip: Dynamics of Water Uptake by Carbon Nanotubes. *J. Chem. Phys.* **2011**, *135*, 214705.
109. Gravelle, S.; Ybert, C.; Bocquet, L.; Joly, L., Anomalous Capillary Filling and Wettability Reversal in Nanochannels. *Phys. Rev. E* **2016**, *93*.

110. Desai, N.; Ghosh, U.; Chakraborty, S., Capillary Filling under Electro-Osmotic Effects in the Presence of Electromagneto-Hydrodynamic Effects. *Phys. Rev. E* **2014**, *89*.
111. Vo, T. Q.; Barisik, M.; Kim, B., Near-Surface Viscosity Effects on Capillary Rise of Water in Nanotubes. *Phys. Rev. E* **2015**, *92*.
112. Bakli, C.; Chakraborty, S., Capillary Filling Dynamics of Water in Nanopores. *Appl. Phys. Lett.* **2012**, *101*.
113. Schlemmer, R.; Friedheim, J.; Growcock, F.; Bloys, J.; Headley, J.; Polnaszek, S. In *Membrane Efficiency in Shale-an Empirical Evaluation of Drilling Fluid Chemistries and Implications for Fluid Design*, IADC/SPE Drilling Conference, Society of Petroleum Engineers: 2002.
114. Cheng, Y. In *Impact of Water Dynamics in Fractures on the Performance of Hydraulically Fractured Wells in Gas Shale Reservoirs*, SPE International Symposium and Exhibition on Formation Damage Control, Society of Petroleum Engineers: 2010.
115. Roychaudhuri, B.; Tsotsis, T. T.; Jessen, K., An Experimental and Numerical Investigation of Spontaneous Imbibition in Gas Shales. In *SPE Annual Technical Conference and Exhibition*, Society of Petroleum Engineers: Denver, Colorado, USA, 2011; p 11.
116. Hu, Q.; Ewing, R. P.; Dultz, S., Low Pore Connectivity in Natural Rock. *Journal of contaminant hydrology* **2012**, *133*, 76-83.
117. Hu, Q.; Ewing, R. P.; Rowe, H. D., Low Nanopore Connectivity Limits Gas Production in Barnett Formation. *Journal of Geophysical Research: Solid Earth* **2015**, *120*, 8073-8087.
118. Hu, Q.-H.; Liu, X.-G.; Gao, Z.-Y.; Liu, S.-G.; Zhou, W.; Hu, W.-X., Pore Structure and Tracer Migration Behavior of Typical American and Chinese Shales. *Petroleum Science* **2015**, *12*, 651-663.
119. Roshan, H.; Ehsani, S.; Marjo, C.; Andersen, M.; Acworth, R., Mechanisms of Water Adsorption into Partially Saturated Fractured Shales: An Experimental Study. *Fuel* **2015**, *159*, 628-637.
120. Zhou, Z.; Abass, H.; Li, X.; Bearinger, D.; Frank, W., Mechanisms of Imbibition During Hydraulic Fracturing in Shale Formations. *Journal of Petroleum Science and Engineering* **2016**, *141*, 125-132.
121. Shen, Y.; Ge, H.; Li, C.; Yang, X.; Ren, K.; Yang, Z.; Su, S., Water Imbibition of Shale and Its Potential Influence on Shale Gas Recovery—a Comparative Study of Marine and Continental Shale Formations. *J Nat Gas Sci Eng* **2016**, *35*, 1121-1128.
122. Zhou, Z.; Hoffman, B. T.; Bearinger, D.; Li, X., Experimental and Numerical Study on Spontaneous Imbibition of Fracturing Fluids in Shale Gas Formation. In *SPE/CSUR Unconventional Resources Conference – Canada*, Society of Petroleum Engineers: Calgary, Alberta, Canada, 2014; p 13.
123. Morsy, S.; Sheng, J. J., Imbibition Characteristics of the Barnett Shale Formation. In *SPE Unconventional Resources Conference*, Society of Petroleum Engineers: The Woodlands, Texas, USA, 2014; p 8.
124. Haluszczak, L. O.; Rose, A. W.; Kump, L. R., Geochemical Evaluation of Flowback Brine from Marcellus Gas Wells in Pennsylvania, USA. *Applied Geochemistry* **2013**, *28*, 55-61.
125. Renock, D.; Landis, J. D.; Sharma, M., Reductive Weathering of Black Shale and Release of Barium During Hydraulic Fracturing. *Applied geochemistry* **2016**, *65*, 73-86.
126. Zolfaghari, A.; Dehghanpour, H.; Noel, M.; Bearinger, D., Laboratory and Field Analysis of Flowback

Water from Gas Shales. *Journal of unconventional oil and gas resources* **2016**, *14*, 113-127.
127. Wang, G.; Zhao, Z.; Li, K.; Li, A.; He, B., Spontaneous Imbibition Laws and the Optimal Formulation of Fracturing Fluid During Hydraulic Fracturing in Ordos Basin. *Procedia Engineering* **2015**, *126*, 549-553.
128. Yang, L.; Ge, H.; Shi, X.; Cheng, Y.; Zhang, K.; Chen, H.; Shen, Y.; Zhang, J.; Qu, X., The Effect of Microstructure and Rock Mineralogy on Water Imbibition Characteristics in Tight Reservoirs. *J Nat Gas Sci Eng* **2016**, *34*, 1461-1471.
129. Wang, D.; Butler, R.; Zhang, J.; Seright, R., Wettability Survey in Bakken Shale with Surfactant-Formulation Imbibition. *SPE Reservoir Evaluation & Engineering* **2012**, *15*, 695-705.
130. Liang, L.; Luo, D.; Liu, X.; Xiong, J., Experimental Study on the Wettability and Adsorption Characteristics of Longmaxi Formation Shale in the Sichuan Basin, China. *J Nat Gas Sci Eng* **2016**, *33*, 1107-1118.
131. Derjaguin, B.; Churaev, N., Structural Component of Disjoining Pressure. *J. Colloid Interface Sci.* **1974**, *49*, 249-255.
132. Checco, A.; Guenoun, P.; Daillant, J., Nonlinear Dependence of the Contact Angle of Nanodroplets on Contact Line Curvature. *Phys. Rev. Lett.* **2003**, *91*, 186101.
133. Yuan, Y.; Lee, T. R., Contact Angle and Wetting Properties. In *Surface Science Techniques*, Springer: 2013; pp 3-34.
134. Marmur, A., Penetration of a Small Drop into a Capillary. *J. Colloid Interface Sci.* **1988**, *122*, 209-219.
135. Stukan, M. R.; Ligneul, P.; Crawshaw, J. P.; Boek, E. S., Spontaneous Imbibition in Nanopores of Different Roughness and Wettability. *Langmuir* **2010**, *26*, 13342-13352.
136. Kelly, S.; Torres-Verdín, C.; Balhoff, M. T., Anomalous Liquid Imbibition at the Nanoscale: The Critical Role of Interfacial Deformations. *Nanoscale* **2016**, *8*, 2751-2767.
137. van't Hoff, J. H., Die Rolle Des Osmotischen Druckes in Der Analogie Zwischen Lösungen Und Gasen. *Zeitschrift für physikalische Chemie* **1887**, *1*, 481-508.
138. Takeda, M.; Hiratsuka, T.; Ito, K.; Finsterle, S. In *Development and Application of Chemical Osmosis Simulator Based on Tough2*, 2012 TOUGH2 Symposium, Lawrence Berkeley National Laboratory Berkeley, California: 2012.
139. Fakcharoenphol, P.; Kurtoglu, B.; Kazemi, H.; Charoenwongsa, S.; Wu, Y.-S., The Effect of Osmotic Pressure on Improve Oil Recovery from Fractured Shale Formations. In *SPE Unconventional Resources Conference*, Society of Petroleum Engineers: The Woodlands, Texas, USA, 2014; p 12.
140. Wayllace, A. Volume Change and Swelling Pressure of Expansive Clay in the Crystalline Swelling Regime. University of Missouri--Columbia, 2008.
141. Gray, G. R.; Darley, H. C.; Rogers, W. F., *Composition and Properties of Oil Well Drilling Fluids*; Gulf Publishing Company, Book Division, 1980.
142. Rao, S. M.; Thyagaraj, T.; Rao, P. R., Crystalline and Osmotic Swelling of an Expansive Clay Inundated with Sodium Chloride Solutions. *Geotechnical and Geological Engineering* **2013**, *31*, 1399-1404.
143. Sun, Y.; Bai, B.; Wei, M., Microfracture and Surfactant Impact on Linear Cocurrent Brine Imbibition

in Gas-Saturated Shale. *Energy Fuels* **2015**, *29*, 1438-1446.

144. Makhanov, K.; Dehghanpour, H.; Kuru, E. In *An Experimental Study of Spontaneous Imbibition in Horn River Shales*, SPE Canadian unconventional resources conference, Society of Petroleum Engineers: 2012.
145. Özkaya, I., A Simple Analysis of Oil-Induced Fracturing in Sedimentary Rocks. *Mar. Pet. Geol.* **1988**, *5*, 293-297.
146. Wang, J.; Rahman, S. S., Investigation of Water Leakoff Considering the Component Variation and Gas Entrapment in Shale During Hydraulic-Fracturing Stimulation. *SPE Reservoir Evaluation & Engineering* **2016**, *19*, 511-519.
147. Wang, X.; Sheng, J. J., Spontaneous Imbibition Analysis in Shale Reservoirs Based on Pore Network Modeling. *Journal of Petroleum Science and Engineering* **2018**, *169*, 663-672.
148. Pollastro, R. M., Total Petroleum System Assessment of Undiscovered Resources in the Giant Barnett Shale Continuous (Unconventional) Gas Accumulation, Fort Worth Basin, Texas. *AAPG bulletin* **2007**, *91*, 551-578.
149. Mengal, S. A.; Wattenbarger, R. A. In *Accounting for Adsorbed Gas in Shale Gas Reservoirs*, SPE middle east oil and gas show and conference, Society of Petroleum Engineers: 2011.
150. Ross, D. J.; Bustin, R. M., Shale Gas Potential of the Lower Jurassic Gordondale Member, Northeastern British Columbia, Canada. *Bulletin of Canadian Petroleum Geology* **2007**, *55*, 51-75.
151. Zhang, Z.; Yang, S., On the Adsorption and Desorption Trend of Shale Gas. *Journal of experimental mechanics* **2012**, *27*, 492-497.
152. Langmuir, I., The Adsorption of Gases on Plane Surfaces of Glass, Mica and Platinum. *J. Am. Chem. Soc.* **1918**, *40*, 1361-1403.
153. Brunauer, S.; Emmett, P. H.; Teller, E., Adsorption of Gases in Multimolecular Layers. *J. Am. Chem. Soc.* **1938**, *60*, 309-319.
154. Dubinin, M., The Potential Theory of Adsorption of Gases and Vapors for Adsorbents with Energetically Nonuniform Surfaces. *Chem. Rev.* **1960**, *60*, 235-241.
155. Yang, F.; Ning, Z.; Liu, H., Fractal Characteristics of Shales from a Shale Gas Reservoir in the Sichuan Basin, China. *Fuel* **2014**, *115*, 378-384.
156. Bae, J.-S.; Bhatia, S. K., High-Pressure Adsorption of Methane and Carbon Dioxide on Coal. *Energy Fuels* **2006**, *20*, 2599-2607.
157. Dada, A.; Olalekan, A.; Olatunya, A.; Dada, O., Langmuir, Freundlich, Temkin and Dubinin–Radushkevich Isotherms Studies of Equilibrium Sorption of Zn2+ Unto Phosphoric Acid Modified Rice Husk. *IOSR Journal of Applied Chemistry* **2012**, *3*, 38-45.
158. Mertens, F. O., Determination of Absolute Adsorption in Highly Ordered Porous Media. *Surf Sci.* **2009**, *603*, 1979-1984.
159. Stadie, N. P.; Murialdo, M.; Ahn, C. C.; Fultz, B., Unusual Entropy of Adsorbed Methane on Zeolite-Templated Carbon. *J. Phys. Chem. C* **2015**, *119*, 26409-26421.
160. Song, H.; Wang, Y.; Wang, J.; Li, Z., Unifying Diffusion and Seepage for Nonlinear Gas Transport in Multiscale Porous Media. *Chem. Phys. Lett.* **2016**, *661*, 246-250.

161. Singh, H.; Javadpour, F., Langmuir Slip-Langmuir Sorption Permeability Model of Shale. *Fuel* **2016**, *164*, 28-37.
162. Beskok, A.; Karniadakis, G. E.; Trimmer, W., Rarefaction and Compressibility Effects in Gas Microflows. *Journal of Fluids Engineering* **1996**, *118*, 448-456.
163. Klinkenberg, L. In *The Permeability of Porous Media to Liquids and Gases*, Drilling and production practice, American Petroleum Institute: 1941.
164. Tanikawa, W.; Shimamoto, T., Comparison of Klinkenberg-Corrected Gas Permeability and Water Permeability in Sedimentary Rocks. *International Journal of Rock Mechanics and Mining Sciences* **2009**, *46*, 229-238.
165. Jones, S. C., A Rapid Accurate Unsteady-State Klinkenberg Permeameter. *Society of Petroleum Engineers Journal* **1972**, *12*, 383-397.
166. Davarzani, H.; Marcoux, M.; Costeseque, P.; Quintard, M., Experimental Measurement of the Effective Diffusion and Thermodiffusion Coefficients for Binary Gas Mixture in Porous Media. *Chemical Engineering Science* **2010**, *65*, 5092-5104.
167. Mason, E. A.; Malinauskas, A., *Gas Transport in Porous Media: The Dusty-Gas Model*; Elsevier Science Ltd, 1983; Vol. 17.
168. Krishna, R.; Wesselingh, J., The Maxwell-Stefan Approach to Mass Transfer. *Chemical engineering science* **1997**, *52*, 861-911.
169. Kapoor, A.; Yang, R.; Wong, C., Surface Diffusion. *Catalysis Reviews—Science and Engineering* **1989**, *31*, 129-214.
170. Sladek, K. J.; Gilliland, E. R.; Baddour, R. F., Diffusion on Surfaces. Ii. Correlation of Diffusivities of Physically and Chemically Adsorbed Species. *Industrial & Engineering Chemistry Fundamentals* **1974**, *13*, 100-105.
171. Myers, A. L.; Belfort, G. *Fundamentals of Adsorption*; Engineering Foundation, New York, NY: 1984.
172. Nodzeński, A., Sorption and Desorption of Gases (Ch4, Co2) on Hard Coal and Active Carbon at Elevated Pressures. *Fuel* **1998**, *77*, 1243-1246.
173. Wu, K.; Li, X.; Wang, C.; Yu, W.; Chen, Z., Model for Surface Diffusion of Adsorbed Gas in Nanopores of Shale Gas Reservoirs. *Industrial & Engineering Chemistry Research* **2015**, *54*, 3225-3236.
174. Sharma, A.; Namsani, S.; Singh, J. K., Molecular Simulation of Shale Gas Adsorption and Diffusion in Inorganic Nanopores. *Molecular Simulation* **2015**, *41*, 414-422.
175. Yang, X.; Zhang, C., Structure and Diffusion Behavior of Dense Carbon Dioxide Fluid in Clay-Like Slit Pores by Molecular Dynamics Simulation. *Chem. Phys. Lett.* **2005**, *407*, 427-432.
176. Zhang, X.; Xiao, L.; Shan, X.; Guo, L., Lattice Boltzmann Simulation of Shale Gas Transport in Organic Nano-Pores. *Scientific reports* **2014**, *4*, 4843.
177. Zhang, T.; Sun, S.; Song, H., Flow Mechanism and Simulation Approaches for Shale Gas Reservoirs: A Review. *Transport in Porous Media* **2019**, *126*, 655-681.
178. Ma, J.; Sanchez, J. P.; Wu, K.; Couples, G. D.; Jiang, Z., A Pore Network Model for Simulating Non-Ideal Gas Flow in Micro-and Nano-Porous Materials. *Fuel* **2014**, *116*, 498-508.
179. Huang, X.; Bandilla, K. W.; Celia, M. A., Multi-Physics Pore-Network Modeling of Two-Phase Shale

Matrix Flows. *Transport in Porous Media* **2016**, *111*, 123-141.
180. Adler, P.; Thovert, J.-F., Real Porous Media: Local Geometry and Macroscopic Properties. *Applied Mechanics Reviews* **1998**, *51*, 537-585.
181. Al-Raoush, R.; Willson, C., Extraction of Physically Realistic Pore Network Properties from Three-Dimensional Synchrotron X-Ray Microtomography Images of Unconsolidated Porous Media Systems. *Journal of hydrology* **2005**, *300*, 44-64.
182. Wang, L.; Wang, S.; Zhang, R.; Wang, C.; Xiong, Y.; Zheng, X.; Li, S.; Jin, K.; Rui, Z., Review of Multi-Scale and Multi-Physical Simulation Technologies for Shale and Tight Gas Reservoirs. *J Nat Gas Sci Eng* **2017**, *37*, 560-578.
183. Sakhaee-Pour, A.; Bryant, S., Gas Permeability of Shale. *SPE Reservoir Evaluation & Engineering* **2012**, *15*, 401-409.
184. Ma, H.; Wang, K.; Fan, L.; Cui, F. In *A Finger Vein Image Quality Assessment Method Using Object and Human Visual System Index*, International Conference on Intelligent Science and Intelligent Data Engineering, Springer: 2012; pp 498-506.
185. Curtis, M. E.; Sondergeld, C. H.; Ambrose, R. J.; Rai, C. S., Microstructural Investigation of Gas Shales in Two and Three Dimensions Using Nanometer-Scale Resolution Imagingmicrostructure of Gas Shales. *AAPG bulletin* **2012**, *96*, 665-677.
186. Ziarani, A. S.; Aguilera, R., Knudsen's Permeability Correction for Tight Porous Media. *Transport in porous media* **2012**, *91*, 239-260.
187. Dusseault, M. B., Coupled Processes and Petroleum Geomechanics. In *Elsevier Geo-Engineering Book Series*, Elsevier: 2004; Vol. 2, pp 49-62.
188. Phan, A.; Cole, D. R.; Weiß, R. G.; Dzubiella, J.; Striolo, A., Confined Water Determines Transport Properties of Guest Molecules in Narrow Pores. *ACS nano* **2016**, *10*, 7646-7656.
189. Ho, T. A.; Striolo, A., Water and Methane in Shale Rocks: Flow Pattern Effects on Fluid Transport and Pore Structure. *AIChE J.* **2015**, *61*, 2993-2999.
190. Li, S.; Dong, M.; Li, Z.; Huang, S.; Qing, H.; Nickel, E., Gas Breakthrough Pressure for Hydrocarbon Reservoir Seal Rocks: Implications for the Security of Long-Term Co2 Storage in the Weyburn Field. *Geofluids* **2005**, *5*, 326-334.
191. Amann-Hildenbrand, A.; Ghanizadeh, A.; Krooss, B. M., Transport Properties of Unconventional Gas Systems. *Mar. Pet. Geol.* **2012**, *31*, 90-99.
192. Vincent, O.; Sessoms, D. A.; Huber, E. J.; Guioth, J.; Stroock, A. D., Drying by Cavitation and Poroelastic Relaxations in Porous Media with Macroscopic Pores Connected by Nanoscale Throats. *Phys. Rev. Lett.* **2014**, *113*, 134501.
193. Vincent, O.; Szenicer, A.; Stroock, A. D., Capillarity-Driven Flows at the Continuum Limit. *Soft matter* **2016**, *12*, 6656-6661.
194. Wang, L.; Tian, Y.; Yu, X.; Wang, C.; Yao, B.; Wang, S.; Winterfeld, P. H.; Wang, X.; Yang, Z.; Wang, Y., Advances in Improved/Enhanced Oil Recovery Technologies for Tight and Shale Reservoirs. *Fuel* **2017**, *210*, 425-445.
195. Lee, T.; Bocquet, L.; Coasne, B., Activated Desorption at Heterogeneous Interfaces and Long-Time

Kinetics of Hydrocarbon Recovery from Nanoporous Media. *Nature communications* **2016**, *7*, 11890.
196. Schebarchov, D.; Hendy, S., Capillary Absorption of Metal Nanodroplets by Single-Wall Carbon Nanotubes. *Nano Lett.* **2008**, *8*, 2253-2257.
197. Schebarchov, D.; Hendy, S., Uptake and Withdrawal of Droplets from Carbon Nanotubes. *Nanoscale* **2011**, *3*, 134-141.
198. Yue, P.; Renardy, Y., Spontaneous Penetration of a Non-Wetting Drop into an Exposed Pore. *Phys. Fluids* **2013**, *25*, 052104.
199. Zhang, Z.; Chen, X.; Xu, J., Entry Effects of Droplet in a Micro Confinement: Implications for Deformation-Based Circulating Tumor Cell Microfiltration. *Biomicrofluidics* **2015**, *9*, 024108.
200. Benet, E.; Vernerey, F. J., Mechanics and Stability of Vesicles and Droplets in Confined Spaces. *Physical Review E* **2016**, *94*, 062613.
201. Zhang, Z.; Drapaca, C.; Chen, X.; Xu, J., Droplet Squeezing through a Narrow Constriction: Minimum Impulse and Critical Velocity. *Physics of Fluids* **2017**, *29*, 072102.
202. Muggeridge, A.; Cockin, A.; Webb, K.; Frampton, H.; Collins, I.; Moulds, T.; Salino, P., Recovery Rates, Enhanced Oil Recovery and Technological Limits. *Philosophical Transactions of the Royal Society A: Mathematical, Physical and Engineering Sciences* **2014**, *372*, 20120320.
203. Al-Shalabi, E. W.; Sepehrnoori, K., A Comprehensive Review of Low Salinity/Engineered Water Injections and Their Applications in Sandstone and Carbonate Rocks. *Journal of Petroleum Science and Engineering* **2016**, *139*, 137-161.
204. Martin, J. C. In *The Effects of Clay on the Displacement of Heavy Oil by Water*, Venezuelan annual meeting, Society of Petroleum Engineers: 1959.
205. Jadhunandan, P. P., *Effects of Brine Composition, Crude Oil, and Aging Conditions on Wettability and Oil Recovery*; Department of Petroleum Engineering, New Mexico Institute of Mining & Technology, 1990.
206. Jadhunandan, P.; Morrow, N., Spontaneous Imbibition of Water by Crude Oil/Brine/Rock Systems. *In Situ;(United States)* **1991**, *15*.
207. Jadhunandan, P.; Morrow, N. R., Effect of Wettability on Waterflood Recovery for Crude-Oil/Brine/Rock Systems. *SPE reservoir engineering* **1995**, *10*, 40-46.
208. RezaeiDoust, A.; Puntervold, T.; Strand, S.; Austad, T., Smart Water as Wettability Modifier in Carbonate and Sandstone: A Discussion of Similarities/Differences in the Chemical Mechanisms. *Energy Fuels* **2009**, *23*, 4479-4485.
209. Sheng, J., Critical Review of Low-Salinity Waterflooding. *Journal of Petroleum Science and Engineering* **2014**, *120*, 216-224.
210. Mohan, S.; Perry, L.; Malhotra, J.; Lyddiatt, A., Assessment of Beer Foam Stability by High Performance Liquid Immunoaffinity Chromatography (Hpliac). *Journal of the Institute of Brewing* **1993**, *99*, 231-236.
211. Tang, G.-Q.; Morrow, N. R., Influence of Brine Composition and Fines Migration on Crude Oil/Brine/Rock Interactions and Oil Recovery. *Journal of Petroleum Science and Engineering* **1999**, *24*, 99-111.

212. Sharma, M.; Filoco, P., Effect of Brine Salinity and Crude-Oil Properties on Oil Recovery and Residual Saturations. *SPE Journal* **2000**, *5*, 293-300.
213. Lager, A.; Webb, K. J.; Black, C.; Singleton, M.; Sorbie, K. S., Low Salinity Oil Recovery-an Experimental Investigation1. *Petrophysics* **2008**, *49*.
214. Morrow, N.; Buckley, J., Improved Oil Recovery by Low-Salinity Waterflooding. *Journal of Petroleum Technology* **2011**, *63*, 106-112.
215. Katende, A.; Sagala, F., A Critical Review of Low Salinity Water Flooding: Mechanism, Laboratory and Field Application. *J. Mol. Liq.* **2019**.
216. Wang, L.; Fu, X., Data-Driven Analyses of Low Salinity Water Flooding in Sandstones. *Fuel* **2018**, *234*, 674-686.
217. Shaker Shiran, B.; Skauge, A., Enhanced Oil Recovery (Eor) by Combined Low Salinity Water/Polymer Flooding. *Energy Fuels* **2013**, *27*, 1223-1235.
218. Jackson, M.; Vinogradov, J.; Hamon, G.; Chamerois, M., Evidence, Mechanisms and Improved Understanding of Controlled Salinity Waterflooding Part 1: Sandstones. *Fuel* **2016**, *185*, 772-793.
219. Mahani, H.; Keya, A. L.; Berg, S.; Bartels, W.-B.; Nasralla, R.; Rossen, W. R., Insights into the Mechanism of Wettability Alteration by Low-Salinity Flooding (Lsf) in Carbonates. *Energy Fuels* **2015**, *29*, 1352-1367.
220. Austad, T.; RezaeiDoust, A.; Puntervold, T. In *Chemical Mechanism of Low Salinity Water Flooding in Sandstone Reservoirs*, SPE improved oil recovery symposium, Society of Petroleum Engineers: 2010.
221. Amirian, T.; Haghighi, M.; Mostaghimi, P., Pore Scale Visualization of Low Salinity Water Flooding as an Enhanced Oil Recovery Method. *Energy Fuels* **2017**, *31*, 13133-13143.
222. McGuire, P.; Chatham, J.; Paskvan, F.; Sommer, D.; Carini, F. In *Low Salinity Oil Recovery: An Exciting New Eor Opportunity for Alaska's North Slope*, SPE western regional meeting, Society of Petroleum Engineers: 2005.
223. Ligthelm, D. J.; Gronsveld, J.; Hofman, J.; Brussee, N.; Marcelis, F.; van der Linde, H. In *Novel Waterflooding Strategy by Manipulation of Injection Brine Composition*, EUROPEC/EAGE conference and exhibition, Society of Petroleum Engineers: 2009.
224. Zahid, A.; Shapiro, A. A.; Skauge, A. In *Experimental Studies of Low Salinity Water Flooding Carbonate: A New Promising Approach*, SPE EOR conference at oil and gas West Asia, Society of Petroleum Engineers: 2012.
225. Al Shalabi, E. W.; Sepehrnoori, K.; Delshad, M. In *Does the Double Layer Expansion Mechanism Contribute to the Lswi Effect on Hydrocarbon Recovery from Carbonate Rocks?*, SPE Reservoir Characterization and Simulation Conference and Exhibition, Society of Petroleum Engineers: 2013.
226. Ding, H.; Rahman, S., Experimental and Theoretical Study of Wettability Alteration During Low Salinity Water Flooding-an State of the Art Review. *Colloids and Surfaces A: Physicochemical and Engineering Aspects* **2017**, *520*, 622-639.
227. Tian, H.; Wang, M., Electrokinetic Mechanism of Wettability Alternation at Oil-Water-Rock Interface. *Surface Science Reports* **2017**, *72*, 369-391.
228. Buckley, J.; Liu, Y., Some Mechanisms of Crude Oil/Brine/Solid Interactions. *Journal of Petroleum*

Science and Engineering **1998**, *20*, 155-160.

229. Hiorth, A.; Cathles, L.; Madland, M., The Impact of Pore Water Chemistry on Carbonate Surface Charge and Oil Wettability. *Transport in porous media* **2010**, *85*, 1-21.
230. Marinova, K.; Alargova, R.; Denkov, N.; Velev, O.; Petsev, D.; Ivanov, I.; Borwankar, R., Charging of Oil− Water Interfaces Due to Spontaneous Adsorption of Hydroxyl Ions. *Langmuir* **1996**, *12*, 2045-2051.
231. Buckley, J.; Takamura, K.; Morrow, N., Influence of Electrical Surface Charges on the Wetting Properties of Crude Oils. *SPE Reservoir Engineering* **1989**, *4*, 332-340.
232. Myint, P. C.; Firoozabadi, A., Thin Liquid Films in Improved Oil Recovery from Low-Salinity Brine. *Current Opinion in Colloid & Interface Science* **2015**, *20*, 105-114.
233. Morrow, N. R., *Interfacial Phenomena in Petroleum Recovery*; Marcel Dekker Inc.: New York, 1990.
234. Tokunaga, T. K., Dlvo-Based Estimates of Adsorbed Water Film Thicknesses in Geologic Co2 Reservoirs. *Langmuir* **2012**, *28*, 8001-8009.
235. Lee, S. Y.; Webb, K. J.; Collins, I.; Lager, A.; Clarke, S.; apos; Sullivan, M.; Routh, A.; Wang, X., Low Salinity Oil Recovery: Increasing Understanding of the Underlying Mechanisms. In *SPE Improved Oil Recovery Symposium*, Society of Petroleum Engineers: Tulsa, Oklahoma, USA, 2010; p 11.
236. Mahani, H.; Berg, S.; Ilic, D.; Bartels, W.-B.; Joekar-Niasar, V., Kinetics of Low-Salinity-Flooding Effect. *Spe Journal* **2015**, *20*, 8-20.
237. Butt, H.-J.; Kappl, M., *Surface and Interfacial Forces*; Wiley Online Library, 2010.
238. Carnie, S. L.; Chan, D. Y.; Mitchell, D. J.; Ninham, B. W., The Structure of Electrolytes at Charged Surfaces: The Primitive Model. *J. Chem. Phys.* **1981**, *74*, 1472-1478.
239. Israelachvili, J. N., *Intermolecular and Surface Forces*; Academic press, 2011.
240. Gregory, J., Interaction of Unequal Double Layers at Constant Charge. *J. Colloid Interface Sci.* **1975**, *51*, 44-51.
241. Shubin, V. E.; Kékicheff, P., Electrical Double Layer Structure Revisited Via a Surface Force Apparatus: Mica Interfaces in Lithium Nitrate Solutions. *J. Colloid Interface Sci.* **1993**, *155*, 108-123.
242. Das, S.; Chakraborty, S., Steric-Effect-Induced Enhancement of Electrical-Double-Layer Overlapping Phenomena. *Phys. Rev. E* **2011**, *84*, 012501.
243. Horn, R.; Clarke, D.; Clarkson, M., Direct Measurement of Surface Forces between Sapphire Crystals in Aqueous Solutions. *J. Mater. Res.* **1988**, *3*, 413-416.
244. Valluri, M.; Alvarez, J.; Schechter, D. In *Study of the Rock/Fluid Interactions of Sodium and Calcium Brines with Ultra-Tight Rock Surfaces and Their Impact on Improving Oil Recovery by Spontaneous Imbibition*, SPE Low Perm Symposium, Society of Petroleum Engineers: 2016.
245. Filoco, P. R.; Sharma, M. M. In *Effect of Brine Salinity and Crude Oil Properties on Relative Permeabilities and Residual Saturations*, SPE Annual Technical Conference and Exhibition, Society of Petroleum Engineers: 1998.
246. Nasralla, R. A.; Nasr-El-Din, H. A., Double-Layer Expansion: Is It a Primary Mechanism of Improved Oil Recovery by Low-Salinity Waterflooding? *SPE Reservoir Evaluation & Engineering* **2014**, *17*, 49-59.

247. Alotaibi, M. B.; Nasralla, R. A.; Nasr-El-Din, H. A., Wettability Studies Using Low-Salinity Water in Sandstone Reservoirs. *SPE Reservoir Evaluation & Engineering* **2011**, *14*, 713-725.
248. Nasralla, R. A.; Bataweel, M. A.; Nasr-El-Din, H. A., Investigation of Wettability Alteration and Oil-Recovery Improvement by Low-Salinity Water in Sandstone Rock. *Journal of Canadian Petroleum Technology* **2013**, *52*, 144-154.
249. Yousef, A. A.; Al-Saleh, S.; Al-Jawfi, M. S. In *Improved/Enhanced Oil Recovery from Carbonate Reservoirs by Tuning Injection Water Salinity and Ionic Content*, SPE Improved Oil Recovery Symposium, Society of Petroleum Engineers: 2012.
250. Alotaibi, M. B.; Nasr-El-Din, H. A.; Fletcher, J. J., Electrokinetics of Limestone and Dolomite Rock Particles. *SPE Reservoir Evaluation & Engineering* **2011**, *14*, 594-603.
251. Matthiesen, J.; Bovet, N.; Hilner, E.; Andersson, M. P.; Schmidt, D.; Webb, K.; Dalby, K. N.; Hassenkam, T.; Crouch, J.; Collins, I., How Naturally Adsorbed Material on Minerals Affects Low Salinity Enhanced Oil Recovery. *Energy Fuels* **2014**, *28*, 4849-4858.
252. Hassenkam, T.; Andersson, M.; Hilner, E.; Matthiesen, J.; Dobberschutz, S.; Dalby, K. N.; Bovet, N.; Stipp, S. L. S.; Salino, P.; Reddick, C. In *A Fast Alternative to Core Plug Tests for Optimising Injection Water Salinity for Eor*, SPE Improved Oil Recovery Symposium, Society of Petroleum Engineers: 2014.
253. Lee, S. Y.; Webb, K. J.; Collins, I.; Lager, A.; Clarke, S.; O'Sullivan, M.; Routh, A.; Wang, X. In *Low Salinity Oil Recovery: Increasing Understanding of the Underlying Mechanisms*, SPE Improved Oil Recovery Symposium, Society of Petroleum Engineers: 2010.
254. Joekar-Niasar, V.; Mahani, H., Nonmonotonic Pressure Field Induced by Ionic Diffusion in Charged Thin Films. *Industrial & Engineering Chemistry Research* **2016**, *55*, 6227-6235.
255. Liu, L.; Chen, X.; Lu, W.; Han, A.; Qiao, Y., Infiltration of Electrolytes in Molecular-Sized Nanopores. *Phys. Rev. Lett.* **2009**, *102*, 184501.
256. Tas, N. R.; Haneveld, J.; Jansen, H. V.; Elwenspoek, M.; van den Berg, A., Capillary Filling Speed of Water in Nanochannels. *Appl. Phys. Lett.* **2004**, *85*, 3274-3276.
257. Gruener, S.; Hofmann, T.; Wallacher, D.; Kityk, A. V.; Huber, P., Capillary Rise of Water in Hydrophilic Nanopores. *Phys. Rev. E* **2009**, *79*.
258. Schoch, R. B.; Han, J.; Renaud, P., Transport Phenomena in Nanofluidics. *Rev. Mod. Phys.* **2008**, *80*, 839-883.
259. Duan, C.; Wang, W.; Xie, Q., Review Article: Fabrication of Nanofluidic Devices. *Biomicrofluidics* **2013**, *7*, 026501.
260. Dimitrov, D. I.; Milchev, A.; Binder, K., Capillary Rise in Nanopores: Molecular Dynamics Evidence for the Lucas-Washburn Equation. *Phys. Rev. Lett.* **2007**, *99*.
261. Mitchell, J. K., *Fundamentals of Soil Behavior*; John Wiley: London, 1993.
262. Howarth, R. W.; Ingraffea, A.; Engelder, T., Natural Gas: Should Fracking Stop? *Nature* **2011**, *477*, 271-275.
263. Malani, A.; Ayappa, K. G., Adsorption Isotherms of Water on Mica: Redistribution and Film Growth. *J. Phys. Chem. B* **2009**, *113*, 1058-1067.
264. Martin, M. G.; Siepmann, J. I., Transferable Potentials for Phase Equilibria. 1. United-Atom

Description of N-Alkanes. *J. Phys. Chem. B* **1998**, *102*, 2569-2577.
265. Cygan, R. T.; Liang, J.-J.; Kalinichev, A. G., Molecular Models of Hydroxide, Oxyhydroxide, and Clay Phases and the Development of a General Force Field. *J. Phys. Chem. B* **2004**, *108*, 1255-1266.
266. Argyris, D.; Cole, D. R.; Striolo, A., Ion-Specific Effects under Confinement: The Role of Interfacial Water. *ACS Nano* **2010**, *4*, 2035-2042.
267. Plimpton, S., Fast Parallel Algorithms for Short-Range Molecular Dynamics. *J. Comput. Phys.* **1995**, *117*, 1-19.
268. Hockney, R. W.; Eastwood, J. W., *Computer Simulation Using Particles*; CRC Press, 1988.
269. Huber, P., Soft Matter in Hard Confinement: Phase Transition Thermodynamics, Structure, Texture, Diffusion and Flow in Nanoporous Media. *J. Phys. Condens. Matter* **2015**, *27*, 103102.
270. Chibbaro, S.; Biferale, L.; Diotallevi, F.; Succi, S.; Binder, K.; Dimitrov, D.; Milchev, A.; Girardo, S.; Pisignano, D., Evidence of Thin-Film Precursors Formation in Hydrokinetic and Atomistic Simulations of Nano-Channel Capillary Filling. *Europhys. Lett.* **2008**, *84*, 44003.
271. Khaneft, M.; Stühn, B.; Engstler, J.; Tempel, H.; Schneider, J. J.; Pirzer, T.; Hugel, T., Imbibition of Polystyrene Melts in Aligned Carbon Nanotube Arrays. *Journal of Applied Physics* **2013**, *113*, 074305.
272. Popescu, M. N.; Oshanin, G.; Dietrich, S.; Cazabat, A., Precursor Films in Wetting Phenomena. *J. Phys. Condens. Matter* **2012**, *24*, 243102.
273. Burlatsky, S. F.; Oshanin, G.; Cazabat, A. M.; Moreau, M., Microscopic Model of Upward Creep of an Ultrathin Wetting Film. *Phys. Rev. Lett.* **1996**, *76*, 86-89.
274. Marry, V.; Dubois, E.; Malikova, N.; Breu, J.; Haussler, W., Anisotropy of Water Dynamics in Clays: Insights from Molecular Simulations for Experimental Qens Analysis. *J. Phys. Chem. C* **2013**, *117*, 15106-15115.
275. Morrow, C. P.; Yazaydin, A. Ö.; Krishnan, M.; Bowers, G. M.; Kalinichev, A. G.; Kirkpatrick, R. J., Structure, Energetics, and Dynamics of Smectite Clay Interlayer Hydration: Molecular Dynamics and Metadynamics Investigation of Na-Hectorite. *J. Phys. Chem. C* **2013**, *117*, 5172-5187.
276. Ngouana W, B. F.; Kalinichev, A. G., Structural Arrangements of Isomorphic Substitutions in Smectites: Molecular Simulation of the Swelling Properties, Interlayer Structure, and Dynamics of Hydrated Cs–Montmorillonite Revisited with New Clay Models. *J. Phys. Chem. C* **2014**, *118*, 12758-12773.
277. Gruener, S.; Hofmann, T.; Wallacher, D.; Kityk, A. V.; Huber, P., Capillary Rise of Water in Hydrophilic Nanopores. *Phys. Rev. E* **2009**, *79*, 067301.
278. Dimitrov, D. I.; Milchev, A.; Binder, K., Capillary Rise in Nanopores: Molecular Dynamics Evidence for the Lucas-Washburn Equation. *Phys. Rev. Lett.* **2007**, *99*, 054501.
279. Das, S.; Mitra, S. K., Different Regimes in Vertical Capillary Filling. *Phys. Rev. E* **2013**, *87*, 063005.
280. Supple, S.; Quirke, N., Rapid Imbibition of Fluids in Carbon Nanotubes. *Phys. Rev. Lett.* **2003**, *90*, 214501.
281. Helmy, R.; Kazakevich, Y.; Ni, C.; Fadeev, A. Y., Wetting in Hydrophobic Nanochannels: A Challenge of Classical Capillarity. *J. Am. Chem. Soc.* **2005**, *127*, 12446-12447.
282. Qiao, Y.; Punyamurtula, V. K.; Han, A.; Kong, X.; Surani, F. B., Temperature Dependence of Working Pressure of a Nanoporous Liquid Spring. *Appl. Phys. Lett.* **2006**, *89*, 251905.

283. Zhao, J.; Liu, L.; Culligan, P. J.; Chen, X., Thermal Effect on the Dynamic Infiltration of Water into Single-Walled Carbon Nanotubes. *Phys. Rev. E* **2009**, *80*, 061206.
284. Bui, K.; Akkutlu, I. Y., Nanopore Wall Effect on Surface Tension of Methane. *Mol. Phys.* **2015**, *113*, 3506-3513.
285. Wang, J.; Kalinichev, A. G.; Kirkpatrick, R. J.; Cygan, R. T., Structure, Energetics, and Dynamics of Water Adsorbed on the Muscovite (001) Surface: A Molecular Dynamics Simulation. *J. Phys. Chem. B* **2005**, *109*, 15893-15905.
286. Ou, X.; Wang, X.; Lin, Z.; Li, J., Heterogeneous Condensation of Water on the Mica (001) Surface: A Molecular Dynamics Simulation Work. *J. Phys. Chem. C* **2017**, *121*, 6813-6819.
287. Hess, B.; Kutzner, C.; Van Der Spoel, D.; Lindahl, E., Gromacs 4: Algorithms for Highly Efficient, Load-Balanced, and Scalable Molecular Simulation. *J. Chem. Theory Comput.* **2008**, *4*, 435-447.
288. Rexer, T. F.; Benham, M. J.; Aplin, A. C.; Thomas, K. M., Methane Adsorption on Shale under Simulated Geological Temperature and Pressure Conditions. *Energy & Fuels* **2013**, *27*, 3099-3109.
289. Bussi, G.; Donadio, D.; Parrinello, M., Canonical Sampling through Velocity Rescaling. *The Journal of chemical physics* **2007**, *126*, 014101.
290. Darden, T.; York, D.; Pedersen, L., Particle Mesh Ewald: An N·Log(N) Method for Ewald Sums in Large Systems. *J. Chem. Phys.* **1993**, *98*, 10089-10092.
291. Malani, A.; Ayappa, K., Adsorption Isotherms of Water on Mica: Redistribution and Film Growth. *J. Phys. Chem. B* **2009**, *113*, 1058-1067.
292. Fang, C.; Qiao, R., Surface Hydration Drives Rapid Water Imbibition into Strongly Hydrophilic Nanopores. *Phys. Chem. Chem. Phys.* **2017**, *19*, 20506-20512.
293. Davis, H. T., *Statistical Mechanics of Phases, Interfaces, and Thin Films*; Wiley-VCH, 1996.
294. Yuet, P. K.; Blankschtein, D., Molecular Dynamics Simulation Study of Water Surfaces: Comparison of Flexible Water Models. *J. Phys. Chem. B* **2010**, *114*, 13786-13795.
295. Kashefi, K.; Pereira, L. M.; Chapoy, A.; Burgass, R.; Tohidi, B., Measurement and Modelling of Interfacial Tension in Methane/Water and Methane/Brine Systems at Reservoir Conditions. *FFE* **2016**, *409*, 301-311.
296. Tolman, R. C., The Effect of Droplet Size on Surface Tension. *J. Chem. Phys.* **1949**, *17*, 333-337.
297. Gravelle, S.; Ybert, C.; Bocquet, L.; Joly, L., Anomalous Capillary Filling and Wettability Reversal in Nanochannels. *Phys. Rev. E* **2016**, *93*, 033123.
298. Israelachvili, J. N., *Intermolecular and Surface Forces*; Academic press, 2015.
299. Leng, Y., Hydration Force between Mica Surfaces in Aqueous Kcl Electrolyte Solution. *Langmuir* **2012**, *28*, 5339-5349.
300. Aarts, D. G.; Schmidt, M.; Lekkerkerker, H. N., Direct Visual Observation of Thermal Capillary Waves. *Science* **2004**, *304*, 847-850.
301. Oyarzua, E.; Walther, J. H.; Mejía, A.; Zambrano, H. A., Early Regimes of Water Capillary Flow in Slit Silica Nanochannels. *Phys. Chem. Chem. Phys.* **2015**, *17*, 14731-14739.
302. Lee, S. H., Molecular Dynamics Simulation Study for Shear Viscosity of Water at High Temperatures Using Spc/E Water Model. *Bull. Korean Chem. Soc.* **2014**, *35*, 644-646.

303. Thompson, P. A.; Robbins, M. O., Shear Flow near Solids: Epitaxial Order and Flow Boundary Conditions. *Physical review A* **1990**, *41*, 6830.
304. Tas, N. R.; Mela, P.; Kramer, T.; Berenschot, J. W.; van den Berg, A., Capillarity Induced Negative Pressure of Water Plugs in Nanochannels. *Nano Lett.* **2003**, *3*, 1537-1540.
305. Duan, C.; Karnik, R.; Lu, M.-C.; Majumdar, A., Evaporation-Induced Cavitation in Nanofluidic Channels. *Proc. Natl. Acad. Sci. U.S.A.* **2012**, *109*, 3688-3693.
306. Zheng, X.; Guo, Z.; Tian, D.; Zhang, X.; Li, W.; Jiang, L., Underwater Self-Cleaning Scaly Fabric Membrane for Oily Water Separation. *ACS Appl. Mater. Interfaces* **2015**, *7*, 4336-4343.
307. Gao, C.; Sun, Z.; Li, K.; Chen, Y.; Cao, Y.; Zhang, S.; Feng, L., Integrated Oil Separation and Water Purification by a Double-Layer Tio 2-Based Mesh. *Energy Environ. Sci.* **2013**, *6*, 1147-1151.
308. Striolo, A.; Cole, D. R., Understanding Shale Gas: Recent Progress and Remaining Challenges. *Energy Fuels* **2017**, *31*, 10300-10310.
309. Zacharoudiou, I.; Chapman, E. M.; Boek, E. S.; Crawshaw, J. P., Pore-Filling Events in Single Junction Micro-Models with Corresponding Lattice Boltzmann Simulations. *J. Fluid Mech.* **2017**, *824*, 550-573.
310. Hu, J.; Ogletree, D.; Salmeron, M., The Structure of Molecularly Thin Films of Water on Mica in Humid Environments. *Surface science* **1995**, *344*, 221-236.
311. Hu, J.; Xiao, X.-D.; Ogletree, D.; Salmeron, M., Imaging the Condensation and Evaporation of Molecularly Thin Films of Water with Nanometer Resolution. *Science* **1995**, *268*, 267-269.
312. Fang, C.; Zhang, F.; Qiao, R., Invasion of Gas into Mica Nanopores: A Molecular Dynamics Study. *J. Phys. Condens. Matter* **2018**, *30*, 224001.
313. Prakash, S.; Xi, E.; Patel, A. J., Spontaneous Recovery of Superhydrophobicity on Nanotextured Surfaces. *Proc. Natl. Acad. Sci. U.S.A.* **2016**, *113*, 5508-5513.
314. Berendsen, H.; Grigera, J.; Straatsma, T., The Missing Term in Effective Pair Potentials. *Journal of Physical Chemistry* **1987**, *91*, 6269-6271.
315. Kroutil, O.; Chval, Z.; Skelton, A.; Predota, M., Computer Simulations of Quartz (101)–Water Interface over a Range of Ph Values. *The Journal of Physical Chemistry C* **2015**, *119*, 9274-9286.
316. Abraham, M. J.; Murtola, T.; Schulz, R.; Páll, S.; Smith, J. C.; Hess, B.; Lindahl, E., Gromacs: High Performance Molecular Simulations through Multi-Level Parallelism from Laptops to Supercomputers. *SoftwareX* **2015**, *1*, 19-25.
317. Darden, T.; York, D.; Pedersen, L., Particle Mesh Ewald: An N· Log (N) Method for Ewald Sums in Large Systems. *The Journal of chemical physics* **1993**, *98*, 10089-10092.
318. Torrie, G. M.; Valleau, J. P., Nonphysical Sampling Distributions in Monte Carlo Free-Energy Estimation: Umbrella Sampling. *J. Comput. Phys.* **1977**, *23*, 187-199.
319. Kumar, S.; Rosenberg, J. M.; Bouzida, D.; Swendsen, R. H.; Kollman, P. A., The Weighted Histogram Analysis Method for Free-Energy Calculations on Biomolecules. I. The Method. *J. Comput. Chem.* **1992**, *13*, 1011-1021.
320. Allen, M. P.; Tildesley, D. J., *Computer Simulation of Liquids*; Oxford university press, 2017.
321. Firoozabadi, A.; Ramey Jr, H. J., Surface Tension of Water-Hydrocarbon Systems at Reservoir Conditions. *J. Can. Pet. Technol.* **1988**, *27*, 41-48.

322. Hu, H.; Weinberger, C. R.; Sun, Y., Effect of Nanostructures on the Meniscus Shape and Disjoining Pressure of Ultrathin Liquid Film. *Nano Lett.* **2014**, *14*, 7131-7137.
323. Hu, H.; Weinberger, C. R.; Sun, Y., Model of Meniscus Shape and Disjoining Pressure of Thin Liquid Films on Nanostructured Surfaces with Electrostatic Interactions. *J. Phys. Chem. C* **2015**, *119*, 11777-11785.
324. König, P.-M.; Roth, R.; Mecke, K., Morphological Thermodynamics of Fluids: Shape Dependence of Free Energies. *Phys. Rev. Lett.* **2004**, *93*, 160601.
325. Jeong, J.-T.; Yoon, S.-H., Two-Dimensional Stokes Flow around a Circular Cylinder in a Microchannel. *J MECH SCI TECHNOL* **2014**, *28*, 573-579.
326. Gardiner, C. W., Handbook of Stochastic Methods for Physics, Chemistry and the Natural Sciences. *Appl. Opt.* **1986**, *25*, 3145.
327. Lyklema, J., *Fundamentals of Interface and Colloid Science*; Academic press, 1995; Vol. II: Solid-Liquid Interfaces.
328. Bazant, M. Z.; Kilic, M. S.; Storey, B. D.; Ajdari, A., Towards an Understanding of Induced-Charge Electrokinetics at Large Applied Voltages in Concentrated Solutions. *Advances in Colloid and Interface Science* **2009**, *152*, 48-88.
329. Zhan, C.; Lian, C.; Zhang, Y.; Thompson, M. W.; Xie, Y.; Wu, J.; Kent, P. R. C.; Cummings, P. T.; Jiang, D.-e.; Wesolowski, D. J., Computational Insights into Materials and Interfaces for Capacitive Energy Storage. *Advanced Science* **2017**, *4*, 1700059.
330. Fukuto, M.; Ocko, B.; Bonthuis, D. J.; Netz, R.; Steinrück, H.-G.; Pontoni, D.; Kuzmenko, I.; Haddad, J.; Deutsch, M., Nanoscale Structure of the Oil-Water Interface. *Physical review letters* **2016**, *117*, 256102.
331. Mamatkulov, S. I.; Khabibullaev, P. K.; Netz, R. R., Water at Hydrophobic Substrates: Curvature, Pressure, and Temperature Effects. *Langmuir* **2004**, *20*, 4756-4763.
332. Janecek, J.; Netz, R. R., Interfacial Water at Hydrophobic and Hydrophilic Surfaces: Depletion Versus Adsorption. *Langmuir* **2007**, *23*, 8417-8429.
333. Sendner, C.; Horinek, D.; Bocquet, L.; Netz, R. R., Interfacial Water at Hydrophobic and Hydrophilic Surfaces: Slip, Viscosity, and Diffusion. *Langmuir* **2009**, *25*, 10768-10781.
334. Jiang, D.-e.; Jin, Z.; Wu, J., Oscillation of Capacitance inside Nanopores. *Nano Letters* **2011**, *11*, 5373-5377.
335. Sharma, A., Equilibrium Contact Angles and Film Thicknesses in the Apolar and Polar Systems: Role of Intermolecular Interactions in Coexistence of Drops with Thin Films. *Langmuir* **1993**, *9*, 3580-3586.
336. Diao, Y. J.; Han, M. W.; Lopez-Berganza, J. A.; Valentino, L.; Marinas, B.; Espinosa-Marzal, R. M., Reconciling Dlvo and Non-Dlvo Forces and Their Implications for Ion Rejection by a Polyamide Membrane. *Langmuir* **2017**, *33*, 8982-8992.
337. Han, M.; Espinosa-Marzal, R. M., Electroviscous Retardation of the Squeeze-out of Nanoconfined Ionic Liquids. *The Journal of Physical Chemistry C* **2018**.
338. Qiu, Y. H.; Ma, J.; Chen, Y. F., Ionic Behavior in Highly Concentrated Aqueous Solutions Nanoconfined between Discretely Charged Silicon Surfaces. *Langmuir* **2016**, *32*, 4806-4814.

339. McEldrew, M.; Goodwin, Z. A. H.; Kornyshev, A. A.; Bazant, M. Z., Theory of the Double Layer in Water-in-Salt Electrolytes. *The Journal of Physical Chemistry Letters, DOI:10.1021/acs.jpclett.8b02543* **2018**.
340. Bazant, M. Z.; Storey, B. D.; Kornyshev, A. A., Double Layer in Ionic Liquids: Overscreening Versus Crowding. *Physical Review Letters* **2011**, *106*, 046102.
341. Bartels, W. B.; Mahani, H.; Berg, S.; Hassanizadeh, S. M., Literature Review of Low Salinity Waterflooding from a Length and Time Scale Perspective. *Fuel* **2019**, *236*, 338-353.
342. Jackson, M. D.; Vinogradov, J.; Hamon, G.; Chamerois, M., Evidence, Mechanisms and Improved Understanding of Controlled Salinity Waterflooding Part 1: Sandstones. *Fuel* **2016**, *185*, 772-793.
343. Sheng, J. J., Critical Review of Low-Salinity Waterflooding. *Journal of Petroleum Science and Engineering* **2014**, *120*, 216-224.
344. Ayirala, S. C.; Al-Enezi, S. M.; Al-Yousef, A. A., A State of the Art Review to Develop Novel Workflow for Microscopic Scale Understanding of Advanced Water Flooding Mechanisms in Carbonates. *Journal of Petroleum Science and Engineering* **2017**, *157*, 530-546.
345. Ayirala, S. C.; Yousef, A. A., A State-of-the-Art Review to Develop Injection-Water-Chemistry Requirement Guidelines for Ior/Eor Projects. *Spe Production & Operations* **2015**, *30*, 26-42.
346. Jiménez-Ángeles, F.; Firoozabadi, A., Tunable Substrate Wettability by Thin Water Layer. *The Journal of Physical Chemistry C* **2016**, *120*, 24688-24696.
347. Jiménez-Ángeles, F.; Firoozabadi, A., Contact Angle, Liquid Film, and Liquid–Liquid and Liquid–Solid Interfaces in Model Oil–Brine–Substrate Systems. *The Journal of Physical Chemistry C* **2016**, *120*, 11910-11917.
348. Koleini, M. M.; Badizad, M. H.; Kargozarfard, Z.; Ayatollahi, S., The Impact of Salinity on Ionic Characteristics of Thin Brine Film Wetting Carbonate Minerals: An Atomistic Insight. *Colloids and Surfaces A: Physicochemical and Engineering Aspects* **2019**, *571*, 27-35.
349. Tian, H. H.; Wang, M. R., Molecular Dynamics for Ion-Tuned Wettability in Oil/Brine/Rock Systems. *Aip Advances* **2017**, *7*.
350. Xu, S.; Wang, J.; Wu, J.; Liu, Q.; Sun, C.; Bai, B., Oil Contact Angles in a Water-Decane-Silicon Dioxide System: Effects of Surface Charge. *Nanoscale Research Letters* **2018**, *13*, 108.
351. Zheng, W.; Sun, C.; Wen, B.; Bai, B., Moving Mechanisms of the Three-Phase Contact Line in a Water–Decane–Silica System. *RSC Advances* **2019**, *9*, 3092-3101.
352. Zhao, J.; Yao, G.; Ramisetti, S. B.; Hammond, R. B.; Wen, D., Molecular Dynamics Investigation of Substrate Wettability Alteration and Oil Transport in a Calcite Nanopore. *Fuel* **2019**, *239*, 1149-1161.
353. Uematsu, Y.; Bonthuis, D. J.; Netz, R. R., Impurity Effects at Hydrophobic Surfaces. *Current Opinion in Electrochemistry* **2018**.
354. Siu, S. W.; Pluhackova, K.; Bo̎ckmann, R. A., Optimization of the Opls-Aa Force Field for Long Hydrocarbons. *Journal of Chemical Theory and Computation* **2012**, *8*, 1459-1470.
355. Joung, I. S.; Cheatham III, T. E., Determination of Alkali and Halide Monovalent Ion Parameters for Use in Explicitly Solvated Biomolecular Simulations. *The journal of physical chemistry B* **2008**, *112*, 9020-9041.

356. Emami, F. S.; Puddu, V.; Berry, R. J.; Varshney, V.; Patwardhan, S. V.; Perry, C. C.; Heinz, H., Force Field and a Surface Model Database for Silica to Simulate Interfacial Properties in Atomic Resolution. *Chemistry of Materials* **2014**, *26*, 2647-2658.
357. Fang, C.; Kang, Q.; Qiao, R., The Role of Disjoining Pressure and Thermal Activation in the Invasion of Droplets into Nanopores. *J. Phys. Chem. C* **2019**.
358. Pronk, S.; Páll, S.; Schulz, R.; Larsson, P.; Bjelkmar, P.; Apostolov, R.; Shirts, M. R.; Smith, J. C.; Kasson, P. M.; Van Der Spoel, D., Gromacs 4.5: A High-Throughput and Highly Parallel Open Source Molecular Simulation Toolkit. *Bioinformatics* **2013**, *29*, 845-854.
359. Firoozabadi, A.; Ramey Jr, H. J., Surface Tension of Water-Hydrocarbon Systems at Reservoir Conditions. *Journal of Canadian Petroleum Technology* **1988**, *27*.
360. Murina, E. L.; Fernández-Prini, R.; Pastorino, C., Molecular Conformation of Linear Alkane Molecules: From Gas Phase to Bulk Water through the Interface. *The Journal of chemical physics* **2017**, *147*, 064907.
361. Luzar, A.; Chandler, D., Hydrogen-Bond Kinetics in Liquid Water. *Nature* **1996**, *379*, 55.
362. Allen, T.; Kuyucak, S.; Chung, S.-H., The Effect of Hydrophobic and Hydrophilic Channel Walls on the Structure and Diffusion of Water and Ions. *The Journal of chemical physics* **1999**, *111*, 7985-7999.
363. Cui, S.; Cochran, H., Molecular Dynamics Simulation of Interfacial Electrolyte Behaviors in Nanoscale Cylindrical Pores. *The Journal of chemical physics* **2002**, *117*, 5850-5854.
364. Qiao, R.; Aluru, N., Atomistic Simulation of Kcl Transport in Charged Silicon Nanochannels: Interfacial Effects. *Colloids and Surfaces A: Physicochemical and Engineering Aspects* **2005**, *267*, 103-109.
365. Feng, G.; Qiao, R.; Huang, J.; Sumpter, B. G.; Meunier, V., Ion Distribution in Electrified Micropores and Its Role in the Anomalous Enhancement of Capacitance. *ACS nano* **2010**, *4*, 2382-2390.
366. Fleharty, M. E.; van Swol, F.; Petsev, D. N., Solvent Role in the Formation of Electric Double Layers with Surface Charge Regulation: A Bystander or a Key Participant? *Physical Review Letters* **2016**, *116*, 048301.
367. Vangara, R.; van Swol, F.; Petsev, D. N., Ionic Solvation and Solvent-Solvent Interaction Effects on the Charge and Potential Distributions in Electric Double Layers. *The Journal of Chemical Physics* **2017**, *147*, 214704.
368. van Swol, F. B.; Petsev, D. N., Solution Structure Effects on the Properties of Electric Double Layers with Surface Charge Regulation Assessed by Density Functional Theory. *Langmuir* **2018**, *34*, 13808-13820.
369. Schlaich, A.; dos Santos, A. P.; Netz, R. R., Simulations of Nanoseparated Charged Surfaces Reveal Charge-Induced Water Reorientation and Nonadditivity of Hydration and Mean-Field Electrostatic Repulsion. *Langmuir* **2018**, *35*, 551-560.
370. Wasserman, E.; Wood, B.; Brodhol, J., The Static Dielectric Constant of Water at Pressures up to 20 Kbar and Temperatures to 1273 K: Experiment, Simulations, and Empirical Equations. *Geochimica et cosmochimica acta* **1995**, *59*, 1-6.
371. Gereben, O.; Pusztai, L., On the Accurate Calculation of the Dielectric Constant from Molecular

Dynamics Simulations: The Case of Spc/E and Swm4-Dp Water. *Chemical Physics Letters* **2011**, *507*, 80-83.

372. Buyukdagli, S.; Blossey, R., Dipolar Correlations in Structured Solvents under Nanoconfinement. *The Journal of chemical physics* **2014**, *140*, 234903.
373. Schlaich, A.; Knapp, E. W.; Netz, R. R., Water Dielectric Effects in Planar Confinement. *Physical review letters* **2016**, *117*, 048001.
374. Ballenegger, V.; Hansen, J.-P., Dielectric Permittivity Profiles of Confined Polar Fluids. *The Journal of chemical physics* **2005**, *122*, 114711.
375. Bonthuis, D. J.; Gekle, S.; Netz, R. R., Profile of the Static Permittivity Tensor of Water at Interfaces: Consequences for Capacitance, Hydration Interaction and Ion Adsorption. *Langmuir* **2012**, *28*, 7679-7694.
376. Bonthuis, D. J.; Gekle, S.; Netz, R. R., Dielectric Profile of Interfacial Water and Its Effect on Double-Layer Capacitance. *Physical review letters* **2011**, *107*, 166102.
377. Bopp, P. A.; Kornyshev, A. A.; Sutmann, G., Frequency and Wave-Vector Dependent Dielectric Function of Water: Collective Modes and Relaxation Spectra. *The Journal of chemical physics* **1998**, *109*, 1939-1958.
378. Cevc, G.; Podgornik, R.; Zeks, B., The Free Energy, Enthalpy and Entropy of Hydration of Phospholipid Bilayer Membranes and Their Difference on the Interfacial Separation. *Chemical Physics Letters* **1982**, *91*, 193-196.
379. Kanduč, M.; Schlaich, A.; Schneck, E.; Netz, R. R., Hydration Repulsion between Membranes and Polar Surfaces: Simulation Approaches Versus Continuum Theories. *Advances in colloid and interface science* **2014**, *208*, 142-152.
380. Wilmott, Z.; Breward, C.; Chapman, S., The Effect of Ions on the Motion of an Oil Slug through a Charged Capillary. *Journal of Fluid Mechanics* **2018**, *841*, 310-350.
381. Starov, V. M.; Kalinin, V. V.; Ivanov, V. I., Influence of Surface Forces on Hydrodynamics of Wetting. *Colloids and Surfaces A: Physicochemical and Engineering Aspects* **1994**, *91*, 149-154.
382. Kuchin, I.; Matar, O.; Craster, R.; Starov, V., Influence of the Disjoining Pressure on the Equilibrium Interfacial Profile in Transition Zone between a Thin Film and a Capillary Meniscus. *Colloids and Interface Science Communications* **2014**, *1*, 18-22.
383. Barsky, S.; Robbins, M. O., Molecular Dynamics Study of Slip at the Interface between Immiscible Polymers. *Physical Review E* **2001**, *63*, 021801.
384. Koplik, J.; Banavar, J. R., Slip, Immiscibility, and Boundary Conditions at the Liquid-Liquid Interface. *Physical review letters* **2006**, *96*, 044505.
385. Razavi, S.; Koplik, J.; Kretzschmar, I., Molecular Dynamics Simulations: Insight into Molecular Phenomena at Interfaces. *Langmuir* **2014**, *30*, 11272-11283.
386. Zhao, R.; Macosko, C. W., Slip at Polymer–Polymer Interfaces: Rheological Measurements on Coextruded Multilayers. *Journal of rheology* **2002**, *46*, 145-167.
387. Schlaich, A.; Kappler, J.; Netz, R. R., Hydration Friction in Nanoconfinement: From Bulk Via Interfacial to Dry Friction. *Nano letters* **2017**, *17*, 5969-5976.

388. Wilmott, Z. M.; Breward, C. J. W.; Chapman, S. J., Modelling Low-Salinity Oil Recovery Mechanisms Using an Ion Dissociation Model. *Transport in Porous Media* **2019**, *127*, 685-709.
389. Trefalt, G.; Behrens, S. H.; Borkovec, M., Charge Regulation in the Electrical Double Layer: Ion Adsorption and Surface Interactions. *Langmuir* **2016**, *32*, 380-400.
390. Raabe, G.; Sadus, R. J., Molecular Dynamics Simulation of the Dielectric Constant of Water: The Effect of Bond Flexibility. *The Journal of chemical physics* **2011**, *134*, 234501.
391. Markesteijn, A.; Hartkamp, R.; Luding, S.; Westerweel, J., A Comparison of the Value of Viscosity for Several Water Models Using Poiseuille Flow in a Nano-Channel. *J. Chem. Phys.* **2012**, *136*, 134104.